POWER SYSTEM STABILITY ENHANCEMENT THROUGH DATA CENTER ANCILLARY SERVICES

A Dissertation
Submitted to the Graduate Faculty
of the
North Dakota State University
of Agriculture and Applied Science

By

Muhammad Ali

In Partial Fulfillment of the Requirements
for the Degree of
DOCTOR OF PHILOSOPHY

Major Department:
Electrical and Computer Engineering

April 2015

Fargo, North Dakota

North Dakota State University
Graduate School

Title

POWER SYSTEM STABILITY ENHANCEMENT THROUGH DATA CENTER ANCILLARY SERVICES

By

MUHAMMAD ALI

The Supervisory Committee certifies that this ***disquisition*** complies with North Dakota State University's regulations and meets the accepted standards for the degree of

DOCTOR OF PHILOSOPHY

SUPERVISORY COMMITTEE:

Dr. Samee U. Khan
Chair

Dr. Ying Huang

Dr. Na Gong

Dr. Jacob Glower

Approved:

April 14, 2015
Date

Dr. Scott C. Smith
Department Chair

ABSTRACT

The primary objective of a control system is stability and steady-state performance under varying dynamics, such as faults and disturbances. The stable power system should continue to function properly in case of faults and disturbances. Stability of the power systems find applications in various domains, such as power delivery through Permanent Magnet Synchronous Generator (PMSG), Doubly-Fed Induction Generator (DFIG), and data centers.

The goal of this dissertation is to design a robust control for a power system. We propose a hybrid Fault-Ride-Through (FRT) strategy for DFIG and two new PMSG grid-interfaced models, named PMSG Boost and PMSG Rectifier-Inverter. We analyze the aforesaid system using symmetrical and asymmetrical grid faults and observe the following parameters: (a) voltage support, (b) active and reactive power support, (c) stringent grid-code conduct, (d) overvoltage and overcurrent protection of rotor and stator, and (e) damped rotor oscillations in current and voltage.

On the other side, we also propose a bi-directional model for power system and data centers. The goal of this research work is to increase the steady-state performance of the power system through computational capabilities of the data centers. Enormous energy consumption of data centers has a major impact on power systems by significantly increasing the electrical load. Due to the increase in electrical load, power systems are facing demand and supply miss-management problems. Therefore, power systems require fast and intelligent ancillary services to maintain robustness, reliability, and stability. Power system jobs will make this situation even more critical for data centers. In our work, we seek an Ancillary Services Model (ASM) to service data centers and power systems. In ASM, we find an optimal job scheduling technique for executing power systems' jobs on data centers in terms of low power consumption, reduced

makespan, and fewer preempted jobs. The power systems' jobs include Optimal Power Flow (OPF) calculation, transmission line importance index, and bus importance index. Furthermore, a Service Level Agreement (SLA) between data centers and power systems is shown to provide mutual benefits.

ACKNOWLEDGMENTS

First and foremost thanks to ALLMIGHTY ALLAH Who has helped me throughout the course of my studies. All of my knowledge, strength, courage, health, and abilities are His blessings upon me and there is no way to fulfill His right to thank Him.

Special thanks to Dr. Samee U. Khan, my advisor, for his help, guidance and innovative ideas. I offer my sincere and deep hearted gratitude to my advisor who always encouraged me, and persistently conveyed the spirit and guidance required for the research. Without his kind guidance and continuous efforts, this disquisition would not have been possible.

I want to express my gratitude to my committee members, Dr. Jacob Glower, Dr. Na Gong, and Dr. Ying Huang. I am also thankful to COMSATS Institute of Information Technology for providing me a wonderful opportunity for my PhD studies in United States. I am really grateful to my all colleagues at NDSU for their support and help.

DEDICATION

I would like to dedicate this dissertation to my parents, my wife Faiza Jadoon and my daughter Khush Bakht Ali.

TABLE OF CONTENTS

LIST OF TABLES

LIST OF FIGURES

1. INTRODUCTION

1.1. Overview

Power system is a complex network that is under the close observation of the engineers and scientists for the past few years [1.1], [1.2], [1.3]. The generation imbalance, faults in the transmission network, and fluctuating load curves have produced several problems in the conventional power system [1.4]. The unavoidable events, such as catastrophic outages, blackouts, and power failures have affected the reliability, stability, and control of the conventional power systems [1.3]. For the above stated reason, the supplying agencies and end users (consumers) have shown great concerns towards the power system management and control [1.5].

The control of generation, transmission, and distribution is a vital requirement for the stable operation of a power system [1.6]. A small miss-match can lead to disastrous events, namely frequency drift, reactive power imbalance, and small angle instability [1.7], [1.8], [1.9], and [1.10]. The dynamics of the power system can vary from the small-scale to large-scale depending on the disturbances occurred [1.11]. In some cases, the dynamics of the power system goes beyond the operator's control and expectations, such as severe contingencies, lightning strikes, and thunder storms [1.12]. Mostly, in complex weather conditions, for example heavy thunder-lighting, the conventional control system of the power network is unable to compute the high non-linearity and fluctuating system dynamics [1.13].

The wide area power system is said to be "stable" when all the controlling parameters are working in the steady-state mode. The stability of the power system is called "robust" when the steady-state performance persists under faults and disturbances. A real-time stable operation of the power system is the first and foremost requirement for carrying out control operations [1.14],

[1.15], and [1.16]. The stability of the power system is the steady state operation of the inter-connected system that is desired during the short-term and long-term disturbances. The authors in [1.17] and [1.18] reported the factors effecting the stability and control of the WASs.

The power system controls can be classified as: **(a)** continuous control and **(b)** discontinuous control. The local controls include continuous signals, such as Automatic Voltage Regulator (AVR) [1.13], Automatic Generation Control (AGC) [1.15], and Power System Stabilizer (PSS) [1.14]. The discontinuous control signals, such as the capacitor bank switching (reactive power compensation), operate for the local stability of small interconnected systems as shown in Figure 10.

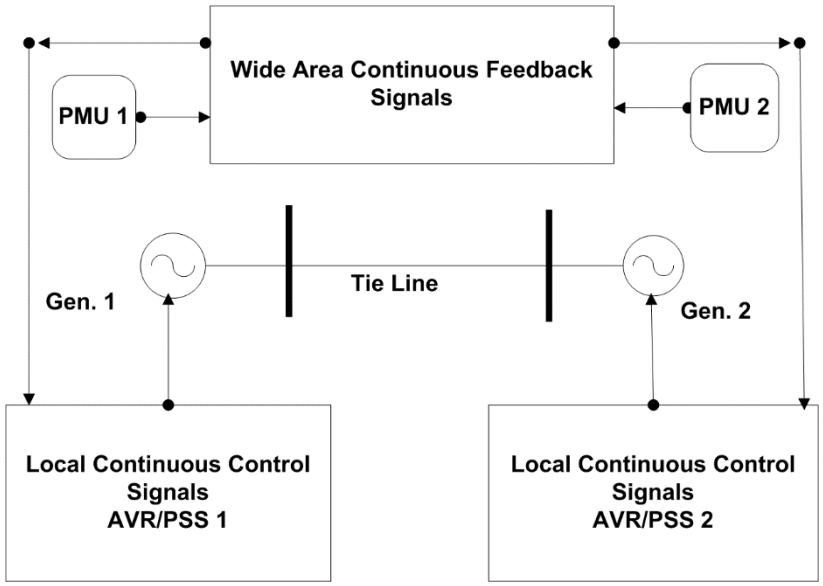

Figure 1.1. Continuous and discontinuous controls in power systems

The local continuous [1.19] and discontinuous controls [1.20] are used to maintain the power system operations in a steady state. The control of the power system offer much more controllability and observability margins [1.21]. The increased margins are acceptable only at the cost of the advanced and efficient communication medium. The taxonomy of the power system stability is presented in Figure 1.2. For power systems, the faults are categorized as: (a) short-

circuit faults and (b) open circuit faults [1.10]. The short-circuit faults are further classified into symmetrical and asymmetrical faults. Symmetrical fault is three-phase to ground short-circuit fault, while asymmetrical fault includes single-phase to ground fault, double-phase to ground fault, and double-phase fault [1.11]. The faults on the power system can occur on generation side, transmission side, and distribution side.

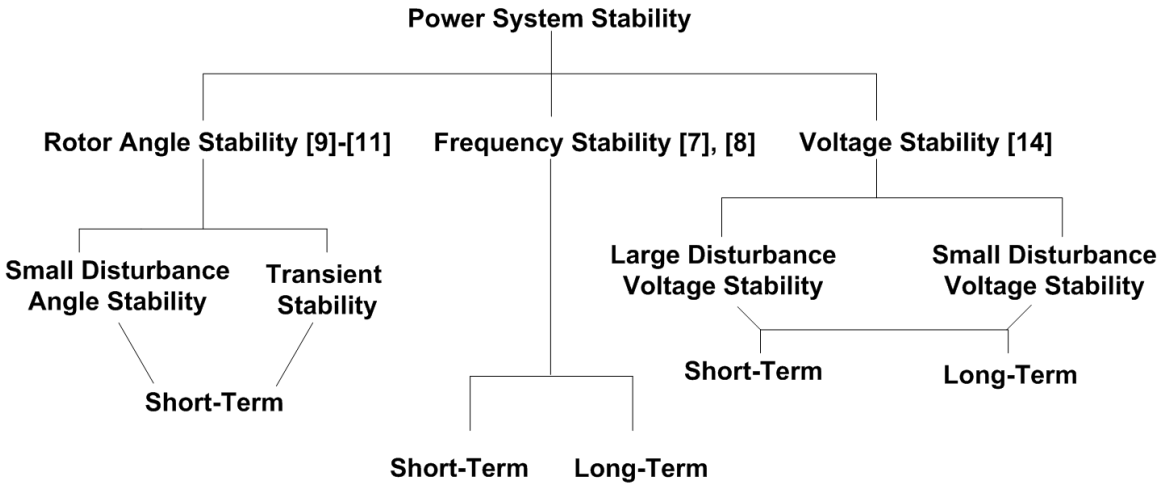

Figure 1.2. A taxonomy of the power system stability

In inter-connected power network, various renewable energy resources are also connected, such as wind power plants, solar panel generation systems, and fuel cell plants [1.12]. The faults related to aforesaid also includes demand-supply miss-management, frequency shifts, active power and reactive power miss-match, and over currents and over voltages. The fault tolerance of power system is provided through several schemes, namely local control system, central control system, Supervisory Control and Data Acquisition (SCADA), and intelligent energy monitoring and management devices [1.13]. The fault tolerant scheme for wind energy systems is called as “Fault-Ride-Through (FRT)” or “Low Voltage Ride-Through (LVRT)”. The above schemes results in high reliability, steady-state performance, and robustness within power systems [1.14], [1.15].

1.2. Motivation

Stability increases the robustness of the power system that further increases reliability and steady-state performance. Faults and disturbances can occur at any instant of time, improper design of the system will lead to malfunctions and dis-order of the equipment. The loss of equipment and device will result in an increase of financial loss. Moreover, system and device failures will cause massive losses within the power system. Furthermore, the power at the receiving end will be less, compared to the sending end voltage.

The transmission lines are stressed by heavy currents flowing through the power system. Voltage sag and dips cause voltage imbalances at both sides of the transmission lines [1.21]. Voltage sag and dips cause voltage imbalances at both sides of the transmission lines. The abnormal currents cause severe disorders, such as the burning of conductors and heavy line losses. The reactive power compensation using capacitors in the form of reactor banks are widely used throughout the power system for controlling voltage instabilities. Large-scale instabilities may cause heavy blackouts in the power system.

In the light of above, there is a pressing need to introduce decentralized control and distributed generation using Renewable Energy, such as wind power plants. The distributed generation will increase the generation capacity of the power system and will provide voltage support during grid faults. The stable operation of Distributed Generators (DGs), such as PMSG and DFIG is the foremost requirement in grid-interfaced systems. Lack of robust control for DGs will result in severe power outages, which can lead to complete blackout during faults and swings within the power system. Therefore, the goal of this dissertation is to develop a stable wind energy system for the power system. As the grid fault will cause voltage dip, wind energy system must supply voltage and reactive power support to the grid, otherwise a severe power

outage will cause blackout. The conventional and advanced schemes developed for FRT violate grid-code requirements, low voltage and power support, rotor overvoltage and overcurrent, and torque oscillations. The EFL control of the PMSG and Hybrid FRT control scheme for DFIG is proposed that overcomes the shortcomings of the conventional and advanced schemes.

1.3. Contributions

The objective of our research is to develop a robust and stable system for Power Systems that include Permanent Magnet Synchronous Generator (PMSG) and Doubly-Fed Induction Generator (DFIG) interfaced with the grid network and an Ancillary Service Model (ASM) for data centers and power system.

1.3.1. Grid-interfaced PMSG

For grid-interfaced PMSG wind energy models, we incorporate Exact Feedback Linearization (EFL) control using differential geometry and Lie-algebra. The PMSG Boost and PMSG Rectifier-Inverter is used for comparative analysis during grid faults. We introduce symmetrical faults for short-time and long-time within the grid network in order to validate the robustness and stability of aforementioned models. The effectiveness of the EFL control over the output DC link voltage of the PMSG is tested during the electrical grid faults and the mechanical perturbations. Moreover, we compared the above models and concluded that the stability of the PMSG Rectifier-Inverter is higher compared to the PMSG Boost during the variation of wind speed values from minimum to maximum. Furthermore, the robustness of the EFL control scheme for the PMSG Rectifier-Inverter is compared with the conventional Proportional and Integral (PI) controller and state-feedback controller. The EFL controller reports a faster output response, better accuracy, and quicker settling time of the output DC link voltage as compared to the PI controller.

1.3.2. Grid-interfaced DFIG

On the other side, for DFIG, we propose a hybrid control strategy that comprises of switch current fault current limiter, rotor crowbar, DC chopper switch, rotor side control, grid side control and wind turbine pitch control using Proportional Integral (PI) control. For switching of rotor side converters and grid side converters, space vector pulse width modulation is utilized. Hysteresis current control mechanism is used for the rotor demagnetization and DC chopper switching. In order to investigate the stability of the proposed scheme, grid faults are introduced for 300ms as: (a) symmetrical faults and (b) asymmetrical faults. Symmetrical faults are three-phase to ground faults, while asymmetrical faults are single-phase to ground fault, double-phase to ground fault, and double-phase fault. Moreover, positive-sequence and negative-sequence component analysis is discussed for in depth response of controlling parameters. Furthermore, our scheme provide protection of rotor and stator against overcurrent and overvoltage.

Power electronic devices are very sensitive to overcurrent and overvoltage, so DC chopper control switch ensures the management of controlling parameters during voltage dips. Our strategy provides voltage support, active power and reactive power support, protection of electronic devices, and stringent following of grid-code requirements. We illustrated the performance of aforesaid parameters using comparative analysis of advanced FRT schemes. The hybrid control FRT strategy outperforms the following strategies: (a) rotor crowbar with advanced IGBT control, (b) advanced control of DC chopper, and (c) switch type fault current limiter. Last but not the least, we observe critically the response of rotor dynamical parameters in terms of fault initiation, fault clearance, steady-state error, torque oscillations, and maximum transient peaks.

1.3.3. Data Center Ancillary Services

For further enhancing the steady-state performance of the power system, we propose a bi-directional ancillary services model for mutual benefits of the data centers and power system. The fast computational capabilities of the data centers are utilized for emergency workload computations of the power systems. The ASM is based on the Service Level Agreement (SLA) to ensure revenue maximization of the data centers during emergency interval within the power system. The reliability and stability of the power system is maintained with minimum transmission line losses. Moreover, we proposed three main ancillary services for stable operation of the power system, namely: (a) Optimal Power Flow (OPF), (b) Transmission Line Importance Index, and (c) Bus Importance Index. Furthermore, the ASM is based on the optimal job scheduling technique for data centers, ancillary services for the power system, and SLA.

1.4. Research Goals and Objectives

The objective of our research is to develop methodologies for monitoring and analyzing the stability of power system under varying dynamics, such as faults and disturbances. The stability of the power system is analyzed critically using wind distributed generators with non-linear control and an ancillary services of the data centers. The effect of grid-faults is observed on the grid-side and its effect on inter-connected system is described.

For case studies, we used permanent magnet synchronous generators and doubly-fed induction generators interfaced with the grid network. Based on the performance of controlling parameters under varying dynamics, we proposed the best fault-ride-through strategy for doubly-fed induction generator and permanent magnet synchronous generator model. The performance of the models is described during fault-initiation and clearance. Moreover, using the computational and on-demand services of the data centers, evaluated the steady-state

performance and stability of the power system using service level agreement. Furthermore, we used resource allocation schemes and real-time data analysis on high computing server that validated the aforesaid objectives of the power system stability.

1.5. Dissertation Outline

The dissertation is organized as follows. In Chapter 2, we present the background and related literature. Chapter 3 presents the stability and steady-state performance of grid-interfaced PMSG for wind energy applications. Chapter 4 presents comparative analysis of DFIG based WECS Fault-Ride-Through Schemes under symmetrical and asymmetrical grid faults. Chapter 5 discusses the mutual interaction of data centers and power systems. In Chapter 6, we present conclusions with future research directions.

1.6. References

[1.1] D. Karlsson, M. Hemmingsson, S. Lindahl, "Wide area system monitoring and control - terminology, phenomena, and solution implementation strategies", *IEEE Power and Energy Magazine*, 2004, 2, (5), pp. 68-76.

[1.2] D. Atanackovic, J. Clapauch, G. Dwernychuk, J. Gurney, H. Lee, "First steps to wide area control", *IEEE Power and Energy Magazine*, 2008, 6, (1), pp. 61-68.

[1.3] B. Morvaj, L. Lugaric, S. Krajcar, "Demonstrating smart buildings and smart grid features in a smart energy city", *Proc. IEEE International Youth Conf. Energetics*, 2011, pp. 1-8.

[1.4] A. Chakrabortty, P. Khargonekar, "Introduction to wide-area control of power systems", *Proc. IEEE American Control Conference (ACC)*, 2013, pp. 6758-6770.

[1.5] M. Hanai, H. Kojima, N. Hayakawa, K. Shinoda, H. Okubo, “Integration of asset management and smart grid with intelligent grid management system”, *IEEE Trans. Dielectrics and Electrical Insulation*, 2013, 20, (6), pp. 2195-2202.

[1.6] H. Liang, A. Abdrabou, W. Zhuang, “Stochastic information management for voltage regulation in smart distribution systems,” *Proc. IEEE INFOCOM*, 2014, pp. 2652-2660.

[1.7] Xiaolong Chen, Y. Li, “An Islanding Detection Algorithm for Inverter-Based Distributed Generation Based on Reactive Power Control,” *IEEE Transactions on Power Electronics*, 2014, 29, (9), pp. 4672-4683.

[1.8] H. Hamida, Ben-Kilani, M. Elleuch, “HVDC transmission in the interconnected south mediterranean region - LFC control analysis,” *Proc. IEEE Multi-Conference on Systems, Signals & Devices (SSD)*, 2014, pp. 1-7.

[1.9] P. Huang, S. Moursi, W. Xiao, L. Kirtley, “Novel Fault Ride-Through Configuration and Transient Management Scheme for Doubly Fed Induction Generator,” *IEEE Transactions on Energy Conversion*, 2013, 28, (1), pp. 86-94.

[1.10] C. Chamroon, T. Cole, T. Wongratanaphisan, “An active vibration control strategy to prevent nonlinearly coupled rotor-stator whirl responses in multimode rotor-dynamic systems”, *IEEE Trans. Control Systems Technology*, 2013, PP, (99), pp. 1-10.

[1.11] F. Mayouf, F. Djahli, A. Mayouf, “Study of Excitation and Governor power system stabilizers effect on the stability enhancement of a single machine infinte-bus power system”, *Proc. IEEE Environment and Electrical Engineering (EEEIC)*, 2013, pp.534-538.

[1.12] B. Sebastian, R. Garg, "Transient stability analysis of multi-machine power system and first swing stability analysis using SVC," *Proc. IEEE Advances in Electrical Engineering (ICAEE)*, 2014, pp. 1-4.

[1.13] Li Wang, Mi Sa-Nguyen Thi, "Stability Enhancement of Large-Scale Integration of Wind, Solar, and Marine-Current Power Generation Fed to an SG-Based Power System Through an LCC-HVDC Link," *IEEE Transactions on Sustainable Energy*, 2014, 5, (1), pp. 160-170.

[1.14] W. Du, J. Zhang, Y. Zhang, Z. Qian, "Stability criterion for cascaded system with constant power load", *IEEE Trans. Power Electronics*, 2013, 28, (4), pp. 1843-1851.

[1.15] D. Mondal, "SVC nonlinear optimal control with comparison to GA based conventional control in power system stability improvement," *Proc. IEEE Electronics, Communication and Instrumentation (ICECI)*, 2014, pp. 1-4.

[1.16] A. Jabr, "Minimum loss operation of distribution networks with photovoltaic generation," IET Renewable Power Generation, 2014, 8, (1), pp. 33-44.

[1.17] Delong Shang, Xuefu Zhang, Fei Xia, A. Yakovlev, "Asynchronous design for new on-chip wide dynamic range power electronics," *Proc. IEEE Design, Automation and Test in Europe Conference and Exhibition (DATE)*, 2014, pp. 1-6.

[1.18] R. Moghadam, B. Ma, R. Zhang, "Distributed Frequency Control in Smart Grids via Randomized Demand Response," *IEEE Transactions on Smart Grid*, 2014, PP, (99), pp. 1-12.

[1.19] R. Khezri, H. Bevrani, "Fuzzy-based coordinated control design for AVR and PSS in multi-machine power systems", *Proc. IEEE Fuzzy Systems (IFSC)*, 2013, pp. 1-5.

[1.20] J. Holland, K. Ikeda, “Forecasting in wind energy applications with site-adaptive Weibull estimation,” *Proc. IEEE Acoustics, Speech and Signal Processing (ICASSP),* 2014, pp. 2184-2188.

[1.21] C. Durga Prasad, P. Kumar, “Dynamic analysis of automatic generation control in a single machine and multi machine isolated power system,” *Proc. IEEE Advances in Electrical Engineering (ICAEE),* 2014, pp. 1-4.

2. RELATED WORK

This chapter presents the background as well as the literature survey on recent works related to the topics investigated throughout this dissertation. We perform categorization of the existing FRT schemes proposed for various types of Renewable Energy Systems.

2.1. Control Schemes for PMSG-WECS

Several control schemes have applied for an optimized performance of variable speed WECS. In the classical control schemes, such as the Proportional Integral (PI) control, the linearized expression is obtained through the Taylor Series (TS) expansion by ignoring the higher terms [2.1]. The final linearized expression of the PI control can only provide the stable operation in the fixed domain of the given parameters. By ignoring the higher order operating states of the dynamical system, the overall response of the system is slow. The parameter tuning of the PI control is obtained by trial and error method, thus making the control system problematic for practical applications. The use of adaptive controllers with variable speed WECS has several advantages, such as high tracking quality and power quality [2.2]. In addition to the complexity of control, the rotor dynamical characteristics must be evaluated quite accurately. Various modern control schemes, such as fuzzy logic control, sliding mode control, and robust control [2.3], [2.4], [2.5] are applied for resolving the WECS issues. The aforementioned control technologies vary in terms of mathematical complexity, control objectives, and applications.

2.2. EFL Control of Grid-Interfaced PMSG

The Exact Feedback Linearization (EFL) is a well-known control scheme that transforms a non-linear system into a completely linear one, through various techniques, such as the input output transformation, zero dynamics approach, disturbance decoupled analysis, and exact feedback linearization algorithms [2.6]. All the aforesaid schemes were applied in WECS except

algorithms of exact feedback linearization, which we will apply in our paper. The EFL provides higher accuracy, optimizes performance in case of fast varying dynamics, stabilizes control of each independent variable, and increases the robustness of the control system in case of faults and disturbances [2.7]. Moreover, the EFL provides an independent control of each regulated variable in WECS integration. Furthermore, the EFL has significant simplification in controller synthesis and system operation.

The transformation of an EFL scheme is based on differential geometry and Lie-algebra. The final linearized expression is obtained through mapping between differential spaces, such as space X, space Y, and space Z. The authors in [2.8] presented the concept of the local and global linearization of the EFL non-linear affine systems. Moreover, the necessary and sufficient conditions for the Single Input Single Output (SISO) and Multiple Input Multiple Output (MIMO) EFL systems were presented in [2.9]. The linearization of the affine non-linear EFL system was presented in [2.10]. The idea of MIMO EFL systems was further elaborated by the authors in [2.10]. The aforementioned research work shows the development of the non-linear affine EFL control scheme.

2.3. Conventional FRT Schemes of DFIG-WT

Various control schemes are proposed in literature to address the objectives of FRT. The control schemes are classified as: (a) Passive schemes and (b) Active schemes. Passive methods are implemented using converter architectural modifications for improving transient stability of the DFIG during faults. The authors in [2.11], [2.12], and [2.13] used Passive crowbar activation strategies employing rotor demagnetization and fault current limiters during grid faults. The DC chopper control circuit for overvoltage protection is described by the authors in [2.14], [2.15]. The excessive power during voltage dips is dissipated across the DC bus. The work of fault-

current limiter using superconductive coil is used in [2.16]. This mechanism limits surge overcurrent of stator and rotor during voltage dip. The coupling of transformer with converter in series with the stator for limiting fault-current is proposed in [2.17]. Although the aforementioned passive schemes limits the excessive fault-current, they lack complete controllability of rotor converters with respect to active and reactive power exchange with the grid. Moreover, this controllability is temporary lost during grid faults, which decreases the reliability of the model.

2.4. Advanced FRT Schemes of DFIG-WT

On the other hand, active schemes are used to reduce cost factor for FRT design models. Active schemes incorporate advanced non-linear control strategies and hardware modifications for stable FRT operation of DFIG WT. Some of the advanced FRT strategies include: (a) robust control [2.18], (b) sliding-mode control [2.19], (c) adaptive control [2.20], (d) model predictive control [2.21], (e) Fuzzy-Logic control [2.22], and (f) Input-Output Feedback Control [2.23]. The aforesaid non-linear strategies are too complex and complicated to implement in industrial applications. Moreover, these non-linear strategies possesses computational burden for the control system. Furthermore, the advanced control schemes cannot provide FRT capability under severe grid faults, as the RSC cannot supply the voltage as high as rotor back EMF because of the DC link voltage limitation [2.24], [2.25]. The idea of using novel Switch Type Fault Current Limiter (STFCL) is proposed in [2.26]. Although the authors provide STFCL based FRT mechanism with simple low cost stator switch circuitry, the model validation is restricted only under Short-time Short Circuit Fault (SSCF). Moreover, robustness and stability parameters of the model are not analyzed thoroughly under grid faults using positive-sequence and negative-sequence component analysis. Over the past decade, intensive research has been published that

only focuses on power management issues in data centers for revenue maximization [2.27], [2.28], [2.29], [2.30], [2.31], [2.32], and [2.33]. On the other hand, the power system research community is only addressing issues of demand and supply management and voltage stability by providing OPF solution [2.34], [2.35]. However, interaction between data centers and power systems has recently attracted the attention of the research community to address the issues of electric power load balancing in power systems and power management in data centers for revenue maximization [2.36], [2.37]. Moreover, none of the earlier works have focused on the usability of data centers' computational capability for maintaining stability in power systems.

In [2.27], the authors described a cost minimization method for data centers that incorporated cloud computing workload and electricity price differences. In [2.28], the authors discussed the aforesaid problem for renewable energy. The SLA based data center cost optimization model was described in [2.29]. The work in [2.30] proposed an energy saving model based on workload distribution to various internet data centers. The concept of the deregulated electricity price for data centers was discussed in [2.31]. The stochastic model for workload distribution on servers of the data center for cost reduction was elaborated in [2.32]. The work in [2.33] discussed that major cause of energy inefficiency in data centers is the wastage of idle power when ICT resources such as servers and data storage run at low utilization. In [2.34], the authors discussed the energy management issues in data center networks from the perspectives of data center architecture connectivity analysis. In all of the aforesaid models, the cost saving criterion was only related to geographical load conditions that was not an optimal approach, as climatic conditions are not the only controlling parameter. Moreover, the revenue of the data centers was only discussed in the perspective of workload, and optimal electricity prices.

2.5. Mutual Interactions between Data Centers and Power Systems

Due to the rapid increase in electrical load but inadequate expansion in generation and transmission, power systems are operating under stressed conditions. In [2.38], the authors presented a voltage stability constraints based OPF approach that improved voltage stability and minimized power system losses during emergency conditions. In [2.39], the authors proposed an artificial Bee Colony algorithm for OPF solution to maintain voltage stability in power systems. The data centers are one of the major power consumers for the power systems, which is a major concern that is directly related to the stability and reliability of power systems.

Recent trends in academic research have shown that the research community is starting to address the issues of interaction between power systems and data centers. In [2.40], the authors addressed the problem of power load balancing in smart grids by taking advantage of data centers' load distribution capability. The authors in [2.41] proposed a model for a data center to offer ancillary services to the smart grid. The data center is a load for any smart grid and the data center will offer load distribution as an ancillary service to the smart grid. In response, the smart grid will offer a lower electricity price to the data center.

To the best of our knowledge, no such mechanism is known to the authors for a data center to provide ancillary services to power systems, such as fast and intelligent OPF solution to reduce Transmission Line Losses (TLLs) and identify endangered TLs and buses for maintaining stability and reliability. Moreover, none of the earlier works addressed the issues and effects on data centers while providing ancillary services to power systems. Furthermore, the SLA between data centers and power systems had not been discussed in any previous studies. Consequently, our work provides a thorough treatment to the aforementioned problem at hand, with a complete theoretical derivation and simulation validation.

2.6. References

[2.1] H. Huang, and C. Chung, "Adaptive neuro-fuzzy controller for static VAR compensator to damp out wind energy conversion system oscillation," *IET Generation, Transmission and Distribution*, vol. 7, no. 2, pp. 200-207, 2013.

[2.2] M. Haque, M. Negnevitsky, and M. Muttaqi, "A novel control strategy for a variable speed wind turbine with PMSG," *IEEE Trans. Ind. Applications.*, vol. 46, no. 1, pp. 331-339, 2010.

[2.3] A. Howlader, N. Urasaki, A. Yona, T. Senjyu, and A. Saber, "A new robust controller approach for a wind energy conversion system under high turbulence wind velocity*," in Proc. IEEE Industrial Electronics and Applications (ICIEA) Conf.,* 2012, pp. 860-865.

[2.4] C. Xia, Q. Geng, X. Gu, T. Shi, and Z. Song, "Input-Output feedback Linearization and speed control of a surface permanent magnet synchronous wind generator with the boost chopper converter," *IEEE Trans. Ind. Electronics*, vol. 59, no. 9, pp. 3489-3500, 2012.

[2.5] F. Delfino, F. Pampararo, R. Procopio, and M. Rossi, "A Feedback Linearization Control Scheme for the Integration of Wind Energy Conversion Systems into Distribution Grids," *IEEE J. Syst.*, vol. 6, no. 1, pp. 85-93, 2012.

[2.6] V. Yaramasu, and B. Wu, "Predictive Control of a Three-Level Boost Converter and an NPC Inverter for High-Power PMSG-Based Medium Voltage Wind Energy Conversion Systems," *IEEE Trans. on Power Electronics*, vol. 29, no. 10, pp. 5308-5322, 2014.

[2.7] Q. Lu, Y. Sun, and S. Mei, Non-linear control system and power system dynamics, *Kluwer Academic Publishers*, 2001, pp. 165-170.

[2.8] Y. Wang, Z. Xia, and T. Zhang, "Sliding mode variable structure control based on exact linearization mode of nonlinear system," *in Proc. IEEE Intelligent Control and Automation (WCICA) Conf.*, 2012, pp. 2878-2881.

[2.9] R. Brockett, "Feedback Invariants for non-linear systems," *in Proc. 7th IFAC World Congress*, Helsinki, June 1978.

[2.10] B. Jakubczyk, and W. Respondek, On linearization of control systems, *Bulletin de L`acadenie Polonaise des Sciences*, 28, 1980.

[2.11] S. Beheshtaein, "Optimal hysteresis based DPC strategy for STATCOM to augment LVRT capability of a DFIG using a new dynamic references method," *in Proc. IEEE Industrial Electronics (ISIE)*, 1-4 June 2014, pp. 612-619.

[2.12] Guolian Hou, Zhentao Wang, Pan Jiang, and Jianhua Zhang, "Multivariable predictive functional control applied to doubly fed induction generator under unbalanced grid voltage conditions," *in Proc. IEEE Industrial Electronics and Applications*, 25-27 May 2009, pp. 2644-2650.

[2.13] T. Riouch, and R. El-Bachtiri, "Improvement low-voltage ride-through control of DFIG during grid faults," *in Proc. IEEE Multimedia Computing and Systems (ICMCS)*, 14-16 April 2014, pp. 1596-1601.

[2.14] Jian-Hong Liu, Chia-Chi Chu, and Yuan-Zheng Lin, "Applications of Nonlinear Control for Fault Ride-Through Enhancement of Doubly Fed Induction Generators," *IEEE Journal of emerging and Selected Topics in Power Electronics*, vol. 2, no. 4, pp. 749-763, Dec. 2014.

[2.15] Hua Geng, Cong Liu, and Geng Yang, "LVRT Capability of DFIG-Based WECS Under Asymmetrical Grid Fault Condition," *IEEE Trans. on Industrial Electronics,* vol. 60, no. 6, pp. 2495-2509, June 2013.

[2.16] B. Ambati, P. Kanjiya, and V. Khadkikar, "A Low Component Count Series Voltage Compensation Scheme for DFIG WTs to Enhance Fault Ride-Through Capability," *IEEE Trans. on Energy Conversion*, vol. PP, no. 99, pp.1-10.

[2.17] F. Lima, A. Luna, P. Rodriguez, E. Watanabe, and F. Blaabjerg, "Rotor Voltage Dynamics in the Doubly Fed Induction Generator During Grid Faults," *IEEE Trans. on Power Electronics*, vol. 25, no. 1, pp. 118-130, Jan. 2010.

[2.18] D. Nguyen, and G. Fujita, "Optimal power control of DFIG wind turbines using a simplified power converter," *in Proc. IEEE T&D Conference and Exposition*, 14-17 April 2014, pp. 1-5.

[2.19] M. Rahimi, and M. Parniani, "Efficient control scheme of wind turbines with doubly fed induction generators for low-voltage ride-through capability enhancement," *IET Renewable Power Generation*, vol. 4, no. 3, pp. 242-252, May 2010.

[2.20] Y. Chongjarearn, "New method of setting the maximum crowbar resistance for doubly-fed induction generators under grid faults," *in Proc. IEEE Electrical Engineering/Electronics*, Computer, Telecommunications and Information Technology (ECTI-CON), 14-17 May 2014, pp. 1-6.

[2.21] K. Okedu, S. Muyeen, R. Takahashi, and J. Tamura, "Wind Farms Fault Ride Through Using DFIG With New Protection Scheme," *IEEE Trans. on Sustainable Energy*, vol. 3, no. 2, pp. 242-254, April 2012.

[2.22] G. Pannell, D. Atkinson, and B. Zahawi, "Minimum-Threshold Crowbar for a Fault-Ride-Through Grid-Code-Compliant DFIG Wind Turbine," *IEEE Trans. on Energy Conversion*, vol. 25, no. 3, pp. 750-759, Sept. 2010.

[2.23] I. Ngamroo, and T. Karaipoom, "Cooperative Control of SFCL and SMES for Enhancing Fault Ride Through Capability and Smoothing Power Fluctuation of DFIG Wind Farm," *IEEE Trans. on Applied Superconductivity*, vol. 24, no. 5, pp. 1-4, Oct. 2014.

[2.24] J. da Costa, H. Pinheiro, T. Degner, and G. Arnold, "Robust Controller for DFIGs of Grid-Connected Wind Turbines," *IEEE Trans. on Industrial Electronics*, vol. 58, no. 9, pp. 4023-4038, Sept. 2011.

[2.25] M. Benbouzid, B. Beltran, Y. Amirat, Gang Yao, Jingang Han, and H. Mangel, "High-Order Sliding Mode control for DFIG-based Wind Turbine Fault Ride-Through," *in Proc. IEEE Industrial Electronics Society IECON*, 10-13 Nov. 2013, pp. 7670-7674.

[2.26] S. Beheshtaein, "Optimal hysteresis based DPC strategy for STATCOM to augment LVRT capability of a DFIG using a new dynamic references method," *in Proc. IEEE Industrial Electronics (ISIE)*, 1-4 June 2014, pp. 612-619.

[2.27] H. Wang, J. Huang, X. Lin, A.H. Mohsenain-Rad, "Exploring smart grid and data center interactions for electric power load balancing," *Newsletter ACM*, vol. 141, no. 3, pp. 89-94, Dec. 2013.

[2.28] M. Ghamkhari and H. MohsenianRad, "Data centers to offer ancillary services," *Proc. IEEE Conf. Smart Grid Communication (Smart Grid Comm)*, pp. 436-441, Oct. 2012.

[2.29] http://www.nyiso.com/public/markets_operations/market_data/ load _data/index.jsp.2014.

[2.30] United States Environmental Protection Agency, “EPA report on server and data center energy efficiency,” *Final Rep. to Congress*, Aug. 2007.

[2.31] U.S.-Canada Power System Outage Task Force, “Final report on the august 14th blackout in United States and Canada,” *United State Department of Energy and National Resources Canada*, 2004, available: http://reports.energy.gov/BlackoutFinal-Web.pdf..

[2.32] A.R. Bergen and V. Vittal, Power Systems Analysis, New Jersey: Prentice Hall, 2nd edn., pp. 81-100, 2000.

[2.33] P. Smita and B.N. Vaidya, “Particle swarm optimization based optimal power flow for reactive loss minimization,” *Proc. IEEE Students' Conf. on Electrical, Electronics and Computer Science (SCEECS)*, pp. 1-4, Mar. 2012..

[2.34] J. Rahul, Y. Sharma, and D. Birla, “A new attempt to optimize optimal power flow based transmission losses using genetic algorithm,” *Proc. IEEE Fourth Int. Conf. on Computational Intelligence and Communication Networks (CICN)*, pp. 566-570, Nov. 2012..

[2.35] M.E. Newman, Networks an Introduction, Oxford University Press, 2010. [2.36] S. Banerjee, A. Das, A. Mazumder, Z. Derakhshandeh, A. Sen, “On the impact of coding parameters on storage requirement of region-based fault tolerant distributed file system design,” *Proc. IEEE Computing, Networking and Communications Conf. (ICNC)*, pp. 78-82, 3-6 Feb. 2014.

[2.36] X. Fan, W.D. Weber, L.A. Barroso, “Power provisioning for a ware-house-sized computer,” *SIGARCH Comput. Archit. News*, vol. 35, no. 2, pp. 13-23, 2007.

[2.37] Amazon EC2, http://aws.amazon.com/ec2/, Accessed on: Oct. 2014..

[2.38] R.D. Zimmerman, C.E. Murillo-Sánchez, and R.J. Thomas, "MATPOW ER steady-state operation, planning and analysis tools for power systems research and education," *IEEE Trans. on Power Systems*, vol. 26, no. 1, pp. 12-19, Feb. 2011.

[2.39] C.T. Kelly, Fundamentals of Algorithms: Solving Nonlinear Equations with Newton's Method, *SIAM Press*, PA, USA, 2003, ISBN: 978-0-89871-546-0.

[2.40] K. Bilal, M. Manzano, S.U. Khan, E. Calle, K. Li, and A.Y. Zomaya, "On the characterization of the structural robustness of data center networks," *IEEE Trans. on Cloud Computing*, vol. 1, no. 1, pp. 64-77, 2013.

[2.41] S.U. Khan and I. Ahmad, "A cooperative game theoretical technique for joint optimization of energy consumption and response time in computational grids*," IEEE Trans. on Parallel and Distributed Systems*, vol. 20, no. 3, pp. 346-360, 2009.

3. EXACT FEEDBACK LINEARIZATION BASED GRID-INTERFACED PMSG CONTROL MODELS

This paper is accepted to the journal: *International Transactions on Energy Systems*. This paper is going through first round of revisions. The authors of this paper are Sahibzada Muhammad Ali, Muhammad Jawad, Feng Gou, Jacob Glower, and Samee U. Khan.

3.1. Overview

Renewable Energy Resources (RERs), such as solar energy, biomass energy, and wind energy is the emerging need of today's power market [3.1], [3.2], [3.3], [3.4], [3.5], [3.6], [3.7]. With rapid development of research in Wind Energy Conversion System (WECS), the power generated by the wind turbine is contributing significantly towards consumers' power demands. The WECS have gained attention of researchers because of high performance, reliability, and low maintenance costs [3.8]. The variable speed WECS possesses various promising features, such as maximum power output and high efficiency. Due to the aforementioned features, many of the power supply companies have installed wind energy generation systems to provide Renewable Energy (RE) to the end users (consumers).

3.1.1. Motivation

The performance and reliability of variable speed WECS is maintained using PMSG. The PMSG model for the wind energy applications need a balanced and stabilized control in the grid-connected mode. The promising features of the PMSG are [3.8], [3.9]: (a) simple mechanical and electrical structure, (b) low wind speed operation, (c) self-excitation, (d) high power factor, (e) high reliability, (f) high efficient operation, and (g) low maintenance costs. Moreover, no gearbox mechanism is required during low speed operation to avoid regular maintenance, which

makes the system unreliable. Furthermore, DC link voltage control and maximum power extraction is achieved under varying wind speeds throughout a day.

For the research community, the integration of wind energy generation systems with the conventional power grids, introduce various challenges. Some of the main challenges are: (a) control of the DC link voltage, (b) support of the grid voltage during perturbations, (c) sensitivity of the parameters drift during extreme conditions, and (d) optimized and robust performance of the PMSG even in worse-case scenarios [3.9]. Conventionally, DC link voltage was controlled using grid-side converter, but researchers suggested that the aforesaid control and Maximum Power Point Tracking (MPPT) can be effectively achieved by generator-side converter [3.10]. The basic issues that occur in the grid-interconnections are the voltage support during unbalanced conditions and the control of the output DC link voltage. Due to the non-linearity in the nature of wind and fast varying WECS dynamics, the steady state operation of the grid-interfaced PMSG is a challenging task. Moreover, the stability enhancement of the control system during mechanical perturbations, electrical grid faults, and PMSG parameter disturbances is a demanding problem. Furthermore, with aforesaid scenario, converter currents and generator outputs, such as rotor speed and stator current need a robust control. Consequently, with this condition, the stability of the grid-interfaced PMSG control system can be local or global depending on the subsets of the control parameters.

3.1.2. Contributions

We present a theoretical analysis and brief comparative discussions on the non-linear PMSG control models applied to the wind energy systems and grid-interconnected applications. The detail discussion on modeling and analysis of the PMSG Boost and the PMSG Rectifier-Inverter with the grid-interconnection is illustrated for the WECSs. Moreover, we also describe

the technical and comparative aspects of the PMSG models in the grid inter-connected mode. Furthermore, the fundamental key issues for the local stability of the PMSG Boost and the PMSG Rectifier-Inverter are also highlighted. We believe that our research contribution is more versatile in selecting a better PMSG model for WECS and design analysis provides the benefits of using the EFL over conventional and non-conventional control schemes, compared to prior works.

In summary, our contributions in this chapter are as follows: (1) we present a robust design of the grid-connected PMSG for machine-side control and grid-side control. Our model provides an optimized control of: (a) DC link voltage, (b) converter current, (c) PMSG rotor speed, (d) stator current, and (e) maximum power transfer to the grid, (2) a stable DC link voltage control is achieved during three phase electrical grid faults (short-time and long-time) and mechanical disturbances (varying input wind speed from minimum to a maximum) with perturbed generator parameters, (3) comparative analysis of the two PMSG models is discussed in detail based on the control features, such as robustness, optimization, and local stability, (4) comparison of the PMSG Rectifier-Inverter is performed with the classical PI controller for the validation of robustness and stability, and (5) identification of the sensitive parameters that cause the abrupt response in the output of the grid-interfaced PMSG Boost.

The rest of the chapter is organized as follows. Section 3.2 demonstrates the local and global linearization of the affine non-linear system. In Section 3.3, Section 3.4, and Section 3.5, we present a comparative analysis of the models, namely PMSG wind turbine, PMSG Boost, and PMSG Rectifier-Inverter. The simulation results of the two PMSG models is performed in Section 3.6 and Section 3.7.

3.2. EFL Conditions for an Affine Non-Linear Systems

We applied EFL controller on the PMSG-Wind energy conversion systems. The EFL transforms non-linear systems into an exact linearized system through coordinate transformation. For the non-linear mapping, the first and foremost objective is to fulfill the necessary and sufficient conditions for exact linearization (local or global). The mathematical control law is derived after satisfying the aforesaid conditions. The control laws of the PMSG Boost and PMSG Rectifier-Inverter is presented in Section 3.3 and Section 3.4. This Section discusses all necessary and sufficient conditions of an EFL controller. Consider a non-linear affine system as:

$$\dot{X} = f(X) + g(X)u,\ y = h(x). \tag{3.1}$$

In Eqn. (1), the parameter $X \in R^n$ is the state vector, u is the control variable, and $(f, g)X$ are the n-dimensional vector fields. To check whether or not an affine non-linear system can be linearized into the Brunovsky Normal Form (BNF), the Lie bracket and the Lie derivative operations are performed as:

$$ad_f g = [f, g]X = \Delta g.(f) - \Delta f.(g), \tag{3.2}$$

$$ad_f^2 g = \Delta ad_f g - \Delta f.ad_f g,$$

$$ad_f^i g = \Delta ad_f^{i-1} g - \Delta f.ad_f^{i-1}.$$

Consider the Lie derivative of the scalar function $\lambda(X)$ along $f(X)$ as:

$$L_f \lambda(X) = \sum_{i=1}^{N} \frac{\partial \lambda(X)}{\partial x_i} f_i(X). \tag{3.3}$$

For the relative degree equal to or less than the degree of the state vector, the following conditions must be met:

$$L_g L_f^k h(X) = 0, k < (r-1), \tag{3.4}$$

$$L_g L_f^{r-1} h(X) \neq 0,$$

$$D = \left[g, ad_f g, ad_f^2 g, \ldots, ad_f^{n-1} g\right],$$

$$r(D) = n.$$

The matrix D must be involutive at $X = X_0$. In Eqn. (4), $r(D)$ is the rank of the matrix D and n is the degree of the state vector. If the aforementioned conditions are all fulfilled, then the non-linear coordinate transformations can be successfully employed on the system model. The conditions of the linearization illustrates that the non-linear coordinate transformation will be global, if for any value of the initial condition, the solution of the Jacobian Matrix (JM) remains non-singular [3.10]. Moreover, the non-linear system is linearized in a large enough region of the space or global space.

3.3. PMSG-Wind Energy Conversion System

The WECS comprises of various electrical elements, such as wind turbine, PMSG, machine side Pulse Width Modulation (PWM) inverter, and grid network. The diagram of the WECS and wind turbine power curve is described in Figure 3.1.

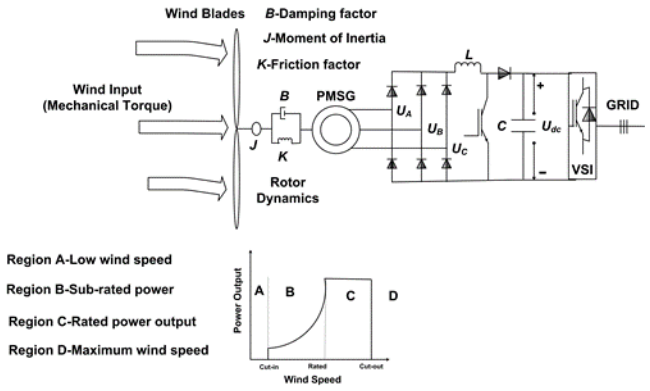

Figure 3.1. PMSG boost

3.3.1. PMSG Wind Turbine Model

The output mechanical power generated by the wind turbine is presented as:

$$P = \frac{1}{2}\rho A V^3 C_p(\beta, \gamma). \tag{3.5}$$

In Eqn. (3.5), ρ is the air density of air, A is the area of the wind blades, V is the velocity of wind, C_p is the performance coefficient, β is the pitch angle of the blades, and γ is the tip speed ratio. The expression of gamma is defined as:

$$\gamma = \frac{2.237V}{\omega}. \tag{3.6}$$

In Eqn. (3.6), ω is the rotor mechanical speed of the wind power generator. The simplified expression of C_p is presented by a non-linear relation as:

$$C_p = \frac{1}{2}(\gamma - 0.022\beta^2 - 5.6)e^{(-0.17\gamma)}. \tag{3.7}$$

The wind turbine operates in four basic regions. The working regions are described as: In Region A, no power will be generated by the wind turbine because of low wind speed, In Region B, sub-rated power is be produced. Sub-rated region exists between cut-in speed and rated speed, In Region C, rated power is produced by the wind turbine, and In Region D, no power is produced due to the existence of stronger winds. The wind turbine goes to shut down mode for mechanical safety. Conventionally, the DC link voltage is controlled by the grid side converter, while maximum power extraction is controlled by the generator side converter.

3.4. Non-Linear PMSG Boost Converter

The non-linear PMSG Boost Converter is presented in Figure 3.1 [3.8]. The PMSG model is interfaced with the Rectifier-Boost Converter circuitry to obtain the desired DC link voltage. The Boost circuitry is inter-linked with the Voltage Source Inverter (VSI) for synchronization with the grid network. The input torque to the PMSG is the wind that is blowing

towards the PMSG blade section. The output is the controlled DC link voltage in the presence of the electrical disturbances (faults, outages, etc.) and the mechanical perturbations (varying wind speed as an input torque). The power turbine characteristic curve of the PMSG Boost is presented in Figure 3.2.

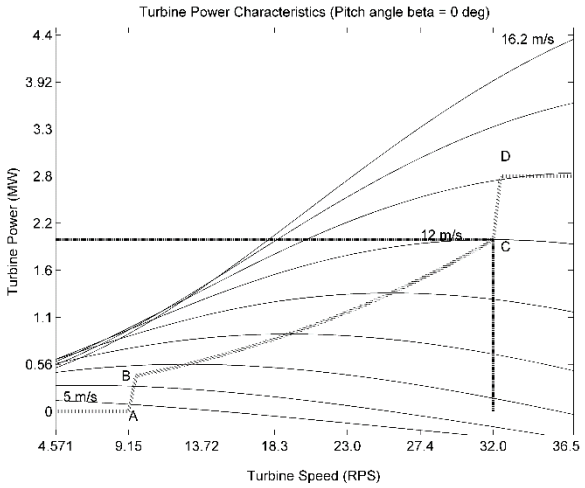

Figure 3.2. Wind turbine characteristic curve for the PMSG boost case

The objective is to obtain the steady state response of the output DC link voltage during the grid faults and varying input torques. In our case, the maximum rated wind speed is 12 m/s, while rated turbine power output is 2MW. The operating region of wind turbine is between points B and C. The wind turbine goes to shut-down mode when wind speed exceeds 12m/s. The MPPT of wind turbine occurs at rated wind speed and controlled by grid-side converter. The objective of MPPT is to obtain maximum power from the wind energy. Moreover, for this objective wind turbine operates in Region B and Region C.

For the ease of understanding, the most commonly used mathematical symbols are given in Table 3.1. The state space model of the PMSG Boost Converter is developed using three parameters, namely: inductor current, electrical rotating machine speed, and rotor electrical angle. The state space model can be presented as:

Table 3.1. Symbols and notation meanings for mathematical analysis

Symbols	Notation Meanings
I_L	Inductor current
R_s	Stator resistance
L_s	Stator inductance
p_n	Number of pole pairs
φ_{PM}	Useful flux linkage
ω_e	Electrical speed of the machine
θ_e	Rotor electrical angle
φ_X^D	Integral curve for mapping
I_d	Direct axis current
I_q	Quadrature axis current
U_d	Direct axis voltage
U_q	Quadrature axis voltage
L_d	Direct axis inductance
L_q	Quadrature axis inductance
T_{em}	Electromagnetic torque
J	Inertial constant
$\emptyset_f$	Useful rotor field flux
U_{dc}	DC link voltage
T_m	Input mechanical torque
T_{mo}	Rated input mechanical torque

$$\dot{I}_L = C_1 I_L + C_2 \omega_e \sin(\theta_e - 60) + C_3, \tag{3.8}$$

$$\dot{\omega}_e = C_4 I_L \sin(\theta_e - 60) + C_5 \omega_e + C_6,$$

$$\dot{\theta}_e = \omega_e.$$

In Eqn. (3.8), the constants from C_1-C_7 consists of the several model constant parameters, such as stator resistance, stator inductance, inertia, and friction that we define as:

$$C_1 = -\frac{2R_s}{2L_s + L'}, \tag{3.9}$$

$$C_2 = -\frac{1.732\varphi_{PM}}{2L_s + L},$$

$$C_3 = -\frac{U_{dc}}{2L_s + L'},$$

$$C_4 = \frac{1.732 p_n^2 \varphi_{PM}}{J},$$

$$C_5 = -\frac{F}{J},$$

$$C_6 = \frac{p_n T_m}{J},$$

$$C_7 = \frac{U_{dc}}{2L_s + L}.$$

The selected state variables on which our mathematical control model will be based on is described by the following three controlling parameters:

$$x_1 = I_L, \tag{3.10}$$

$$x_2 = \omega_e,$$

$$x_3 = (\theta_e - 60).$$

The vector fields *f(X)* and *g(X)* are formed by performing the necessary conditions of the Lie-algebra. The control law *u* is the desired duty cycles for boosting the DC link voltage to a rated value and the output function is *y*. The mathematical expressions for the aforementioned case can be defined as:

$$f(X) = \begin{pmatrix} C_1 I_L + C_2 \omega_e \sin(\theta_e - 60) + C_3 \\ C_4 I_L \sin(\theta_e - 60) + C_5 \omega_e + C_6 \\ \omega_e \end{pmatrix}. \tag{3.11}$$

$$g(X) = \begin{pmatrix} C_7 \\ 0 \\ 0 \end{pmatrix},$$

$$u = d,$$

$$y = h(X) = x_3.$$

The Lie-derivative and the Lie-bracket operation is performed using the transformations using non-linear coordinate transformations. We define the mapping, inverse mapping, derived

mapping, and solving a set of partial differential equations for the conversion of the non-linear system into a linear system as described in Figure 3.3. The sufficient and necessary non-linear coordinate transforms are carried out from the *W* space to the Z^{n-1} space. Moreover, the mapping will be calculated from the *X* space to the Z^{n-1} space. The coordinate transform *T* is defined as, $T=R^{(n-1)}f^{-1}$. The diffeomorphic relation among *W*, *X*, and *Z* spaces through the non-linear coordinate transforms is shown in Figure 3.3.

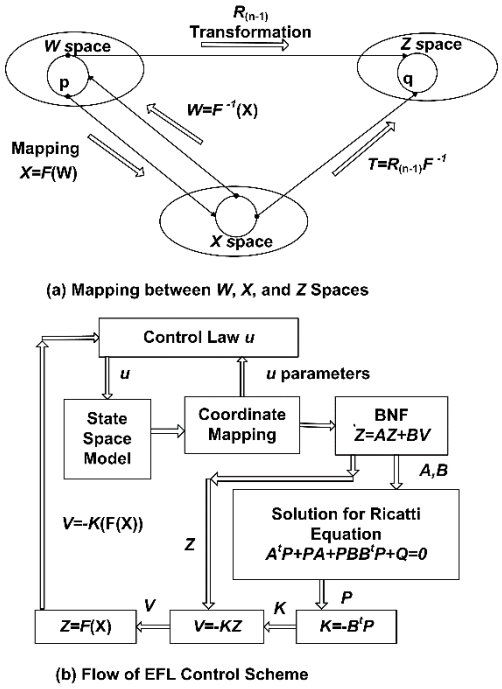

Figure 3.3. Coordinate transformations between *W*, *X*, and *Z* spaces

For the Brunovsky Normal Form (BNF), the mapping between any two spaces must exhibit a local diffeomorphic relation. To obtain a fully linearized expression, the non-linear coordinate transforms are carried from one space to the other depending on the degree of the state model of the system. The final coordinate transformation from the non-linear system into an exactly linear system is called the BNF. Consequently, the BNF and linearized system will become as:

$$\dot{Z} = AZ + BV, \tag{3.12}$$

$$\dot{z}_1 = z_2,$$

$$\dot{z}_2 = z_3,$$

$$\dot{z}_3 = v.$$

The non-linear mathematical control law model for the PMSG Boost is illustrated in terms of the vector fields, controlling parameters, and the linear control variable. The performance index or cost function *J* is Linear Quadratic Ricatti (LQR), which is described as:

$$J = \frac{1}{2}\int_0^{\infty} (\varphi^T(X) Q \varphi(X)) + \left(\frac{d\varphi_n(X)^T}{dt}\right) R \left(\frac{d\varphi_n(X)}{dt}\right) dt. \tag{3.13}$$

Where *Q* is semi-positive definite $n \times n$ matrix and *R* is a positive definite $m \times m$ matrix. The expression of the linear control variable *v* is a LQR problem that provides optimized values of the control variables. The linear control variable *v* is obtained by solving Ricatti Equation (RE). After completely solving a set of partial differential equations the control law *u* becomes:

$$RE = A^T P + PA + PBB^T P + Q = 0, \tag{3.14}$$

$$u = d = \frac{-f_1^{\sim}(X) + v^*}{g_1^{\sim}(X)},$$

$$v^* = (x_3 - x_{3o}) - 2.29x_2 - 2.14(C_4 x_1 \sin(\theta_e - 60) + C_5 x_2 + C_6),$$

$$f_1^{\sim}(X) = C_4 sinx_3 (C_1 x_1 + C_2 x_2 sinx_3 + C_3) + C_5 \dot{x}_2 + C_4 x_1 x_2 cosx_3,$$

$$g_1^{\sim}(X) = C_4 C_7 sinx_3.$$

Eqn. 3.14 is the desired control law for the stable operation of the PMSG Boost. The value of u provides the duty cycles (PWM) to the boost converter for maintaining the stable output response of the system. The denominator term in the control law contains constants and a state variable term. The boundaries of x_3 are defined in the subset Ω as:

$$\Omega = \{x_3 | x_3 \in u, x_3 \neq (0, pi) \& C_4 C_7) \neq 0\}. \quad (3.15)$$

The summary of the control law model (through the EFL) can be observed from Figure 3.4. The electrical parameters for the PMSG Boost are listed in Table 3.2.

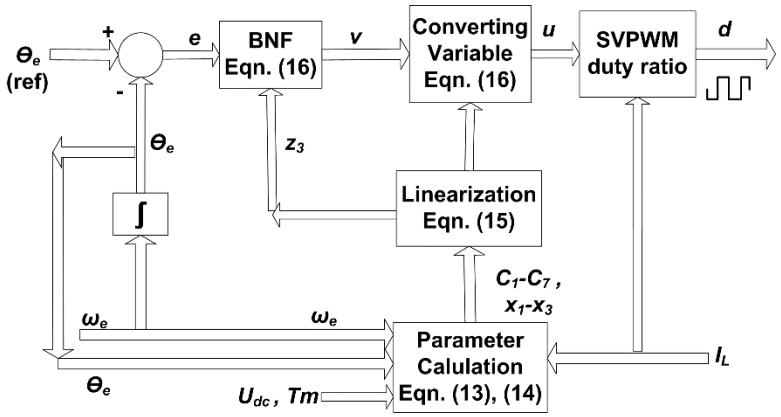

Figure 3.4. EFL control flow of the PMSG boost

Table 3.2. Parametric values of the PMSG boost

Model Parameters	Value
Rated power (generator)	2MW
Flux linkage of generator	9.7Wb
Stator resistance	0.1ohms
Stator inductance	0.835mH
Number of pole pairs	40
Moment of inertia	1000,00Kg-m^2
Friction factor	1000Kg-m^2
DC link inductance	50mH
DC link capacitance	500mF
DC link voltage	900V
Synchronizing frequency	60Hz
Sampling frequency	20KHz
Rotor speed	32rps
Rated wind speed	12m/s
Rated torque	4000N.m

In Eqn. (3.14), the numerator and the denominator have the trigonometric terms, such as the sine and the cosine. Therefore, an impression of the cotangent term is created that produces small spikes in the output response of the system. The sensitivity of the sine parameter in the

denominator of the control law is very high that needs strict thresholds for the stable operation of the system. The local subset in Eqn. (3.14) shows the local stability of the PMSG Boost. The value of x_3 can never be zero and 180 degrees. Between the two points, the system remains stable but local. The control law u will provide the desired duty cycles to control the rectifier block that will boost the output DC voltage up to the desired value.

3.5. PMSG Rectifier-Inverter

The back-to-back Pulse Width Modulation (PWM) converter is described in Figure 3.5 [3.8]. Both the generator and the grid sections of the converter have the same main circuits that makes the control system similar for both sides of the system [3.9]. The synchronization of the obtained voltage with the electrical grid is performed by the inverter section. The capacitor between the two sections eliminates the ripples from the DC link voltage. The input is the wind speed that generates the mechanical torque. The wind turbine power characteristic curve is described in Figure 3.6.

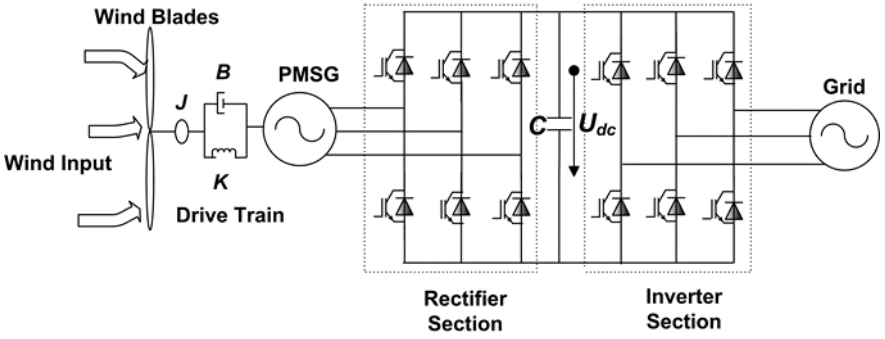

Figure 3.5. PMSG rectifier-inverter

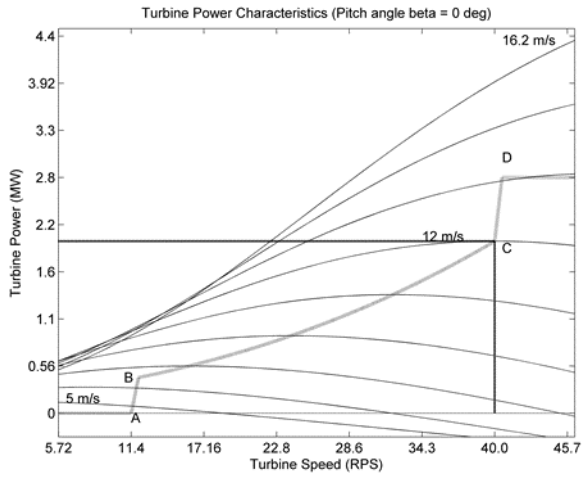

Figure 3.6. Wind turbine characteristic curve for the PMSG rectifier-inverter case

3.5.1. Generator-Side Control

In conventional current vector control, the control strategy of the Generator-Side Converter (GSC) includes the following two main parts: current control loop and conversion from current control signals to voltage control signals. The complete generator control system using space vector PWM is shown in Figure 3.7. The quadrature-axis and direct-axis voltage equations of the synchronous *d-q* frame of reference are described below. The quadrature-axis and direct-axis currents are used as a state variables that control U_q and U_d through EFL. U_q and U_d are in turn used to generate three phase PWM pulses through space vector modulation mechanism. The aforesaid triggering pulses are used to control the DC link voltage. Unlike the conventional vector control, the current vector EFL control directly calculates the *q*-axis reference voltage U_{qref} .

$$U_q^* = R_s I_q + L_s \dot{I}_q + \omega L_q I_d + \omega \varphi_{PM}, \tag{3.16}$$

$$U_d^* = R_s I_d + L_s \dot{I}_d - \omega L_d I_q.$$

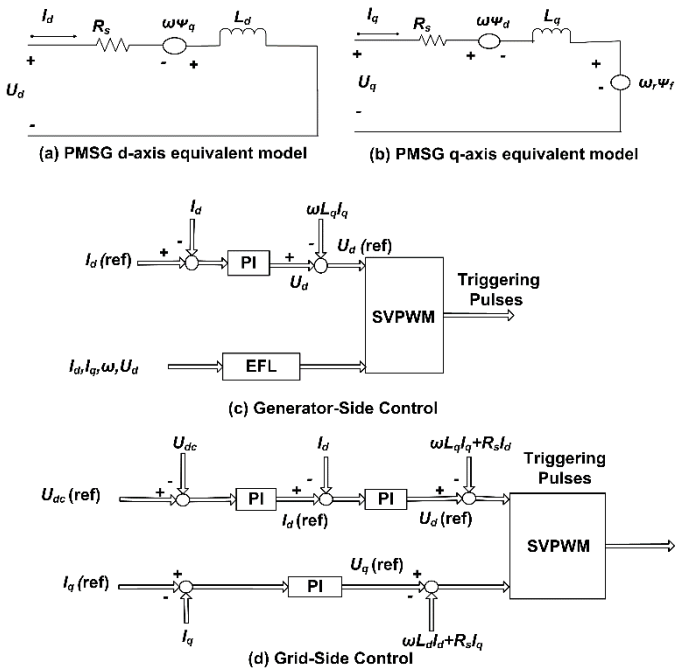

Figure 3.7. Generator-side and grid-side control

There is a stator *d*-axis current control that is set to zero (minimum stator current control strategy). The stator *d*-axis voltage U_d' can be generated by the current-loop controller. The current control signal can be converted to voltage control signal that is stator *d*-axis voltage U_{dref}.

3.5.2. Grid-Side Control

The active and reactive power grid controls are achieved by controlling the direct and quadrature current components. The control scheme for the Grid-Side Converter System (GSCS) is similar to the GSC. The GSCS circuitry consists of the circuit that generates controlled DC link voltage, DC bus, an inverter, and the grid section. The GSCS converts the U_q and U_d voltage signals from Cartesian Coordinates to polar coordinate system. The aforesaid signals are converted into three phase triggering pulses through *d*-*q* transformations. The MPPT is achieved using the two control loops that control the active and reactive power [3.6].

The MPPT mechanism ensures the transfer of maximum active power and reactive power to the grid side for synchronization. The DC link voltage control loop is used to control the *d*-axis current I_d . The total power coming from the rectifier is delivered to the grid by the inverter. The reference DC voltage U_{dcref} must be set a little higher than the actual one, which keeps the inverter to deliver the power. A reactive power control loop is setting a *q*-axis current reference I_{qref} to a current control loop that is similar to the *d*-axis current control loop. The grid controller ensures that all of the power in the DC link must be delivered to the grid. The scheme of the grid-side controller is depicted in Figure 3.7.

3.5.3. Mathematical Model of the PMSG Rectifier-Inverter

The non-linear state space model of the PMSG Rectifier-Inverter in the grid-connected mode is described in terms of the three parameters, namely: direct axis current, quadrature axis current, and electrical rotating speed. The non-linear state space model of the PMSG Rectifier-Inverter is linearized using the same scheme of the EFL employed for the PMSG Boost. The three controlling parameters will be analyzed for the conversion of non-linear system into a completely linear model, the BNF. The simplified model is described as:

$$\dot{x}_1 = k_1 x_2 x_3 + k_2 x_1, \tag{3.17}$$

$$\dot{x}_2 = k_4 x_2 + k_5 x_1 x_3 + k_6 V_q + k_7 x_3,$$

$$\dot{x}_3 = k_8 x_2 + k_9.$$

In Eqn. (3.17), the terms k_1-k_8 consists of various constant model parameters, such as direct axis inductance, quadrature axis inductance, and stator resistance. These constants are mathematically presented as:

$$k_1 = p, \tag{3.18}$$

$$k_2 = -\frac{R}{L_d},$$

$$k_3 = -\frac{R}{L_q},$$

$$k_4 = -p,$$

$$k_5 = \frac{1}{L_q},$$

$$k_6 = -\frac{\lambda_p}{L_q},$$

$$k_7 = -\frac{1.5p^2\lambda}{4J},$$

$$k_8 = -\frac{BP}{2J}.$$

The state variables will be equal to the degree of the state vector. The non-linear PMSG Rectifier-Inverter is of order three. Therefore, the three state variables are given as:

$$x_1 = I_d, \tag{3.19}$$

$$x_2 = I_q,$$

$$x_3 = \omega.$$

The vector fields *f(X)* and *g(X)* are calculated for analyzing the Lie-algebra operation. The vector fields, control variable and the output function are defined as:

$$f(X) = \begin{pmatrix} k_1 x_2 x_3 + k_2 x_1 \\ k_4 x_2 + k_5 x_1 x_3 + k_6 V_q + k_7 x_3 \\ k_8 x_2 + k_9 \end{pmatrix}, \tag{3.20}$$

$$g(X) = \begin{pmatrix} 0 \\ k_5 \\ 0 \end{pmatrix},$$

$$u = U_q = d,$$

$$y = h(X) = x_2.$$

The electrical parameters for the PMSG Rectifier-Inverter are listed in Table 3.3. The linear control variable and the control law become:

$$u = -\frac{D(A) + E(B) + F(C) + (-z_1 - 2.29z_2 - 2.14z_3)}{k_4k_5k_7x_1 + k_1k_4k_5x_3^2 + k_5k_3^2 + k_6k_5k_7}, \tag{3.21}$$

$$z_1 = h(X),$$

$$z_2 = L_f h(X),$$

$$z_3 = L_f^2 h(X),$$

$$A = k_1x_2x_3 + k_2x_1,$$

$$B = k_3x_2 + k_4x_1x_3 + k_6x_3,$$

$$C = k_7x_2 + k_8,$$

$$D = k_2k_4x_3 + k_4k_3x_3 + k_4k_7x_2 + k_4k_8,$$

$$E = k_7k_4x_1 + k_4k_1x_3^2 + k_3^2 + k_6k_7,$$

$$F = k_2k_4x_1 + k_4k_3x_1 + 2k_4k_1x_2x_3 + k_3k_6 + k_4.$$

Table 3.3. Parametric values of the PMSG rectifier inverter

Model Parameters	Value
Rated power (generator)	2MW
Flux linkage of generator	9.7Wb
Stator resistance	0.1ohms
Stator inductance	0.835mH
Number of pole pairs	40
Moment of inertia	1000,00Kg-m^2
Friction factor	1000Kg-m^2
DC link inductance	30mH
DC link capacitance	800mF
DC link voltage	1400V
Synchronizing frequency	60Hz
Sampling frequency	20KHz
Rotor speed	40rps
Rated wind speed	12m/s
Rated torque	5500N.m

The control law of the PMSG Rectifier-Inverter, is derived on the same principle, as that of the EFL. Proceeding in a similar fashion, the final control equation for the PMSG Rectifier-Inverter is obtained after solving a lengthy set of expressions according to the EFL model, as described in Figure 3.3.The denominator term in Eqn. (3.20) of the control law is void of the sine and the cosine terms. The sensitivity of the controlling parameters x_1 and x_3 is very low, as compared to the sensitivity of the control law for the PMSG Boost. Because the local subset has no trigonometric terms in Eqn. (3.20), the local stability associated with the thresholds x_1 and x_3 will produce more stability than the PMSG Boost. The boundary subset is defined as:

$$\Omega = \{ x_1 x_3 | \, x_1 x_3 \neq 0 \& (k_1 \dots k_9) \neq 0 \}. \qquad (3.22)$$

3.6. Simulation Results of the PMSG Boost

The PMSG Boost is implemented using the EFL scheme in MATLAB/Simulink. The cotangent factor in the control law has produced an undesired peaks in the output DC link voltage U_{dc}. With undesired spikes, the PMSG Boost in the grid synchronized mode will affect the stability of the inter-connected system from the small-scale to large-scale. The solution for the aforesaid problematic response is suggested by further linearization of the control law. In windy areas, the proportionality of getting the desired mechanical input (wind) is optimum. The high speed wind factor is putting a safety measure on the state variable x_3. But as the wind speed fluctuates, the varying parameter x_3 will produce a shift in the value of $sinx_3$. The controller must react quickly to maintain the stabilized output with varying control parameters. The above mentioned problem arises due to a very high value generated by the fraction $\frac{1}{sinx_3}$, when the state variable x_3 approaches to zero. To overcome the non-linear response of $\frac{1}{sinx_3}$, a limiter is applied in the EFL controller to avoid an infinity condition. Moreover, this methodology of adding a limiter is a cost increasing factor for the design of real-time applications.

The stability of the above mentioned designed model is analyzed in the presence of a three-phase short circuit line to the ground faults across the grid section. The three-phase short circuit faults are introduced as: (a) Short-time Short Circuit Fault (SSCF) and (b) Long-time Short Circuit Fault (LSCF). Figure 3.8 shows the DC link voltage response during the SSCF and LSCF. The PMSG parameters, such as friction, inertia, stator resistance, and flux linkage of the magnets are also changed from the nominal to the slight off-nominal values. These PMSG machine model parameters are changed to 1.5% of the rated machine values. The heavy LSCF will make the DC link voltage to reach the value of zero for some duration of the clearing time. As soon as the clearing time of the fault is over, the DC link voltage maintains a steady state response. Because of the large reduction in the DC link voltage U_{dc} magnitude during the SSCF and LSCF with perturbed generator parameters, the robustness level of the PMSG Boost against the faults is low.

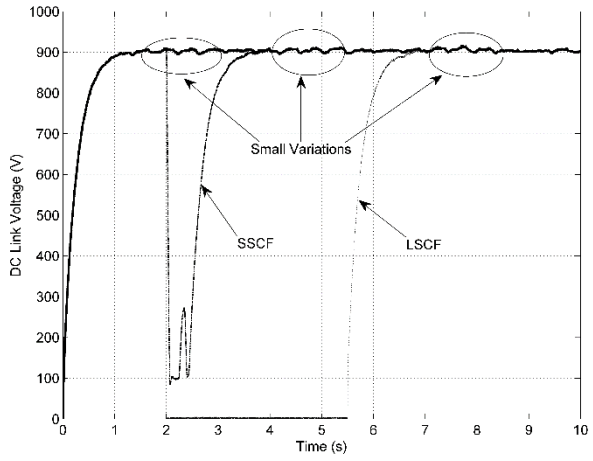

Figure 3.8. DC link voltage response during steady state, SSCF, and LSCF with perturbed generator parameters

The stability of the PMSG Boost is further analyzed by varying the input mechanical torque from minimum to the maximum value. We analyzed that the stability of the PMSG Boost is only limited to the mechanical torque variation of 80%. The minimum torque variation of 80%

means that the wind speed is reduced to 20% from the maximum 100% rated speed. When the torque variation goes below 80% of the rated value, the output response of the DC link voltage goes below the rated value of 900V, as defined in Table 3.2. The PMSG Boost is not robust because the designed controller is only accepting the minimum varying input torque (wind speed) of 20%. The stability of the PMSG Boost is also compromising due to the aforementioned limitation of the controller. When the wind speed varies to 50% and 30% of the rated speed, the optimized DC link voltage response is unachievable. The output DC link voltage response of the PMSG Boost with varying input torques is shown in Figure 3.9.

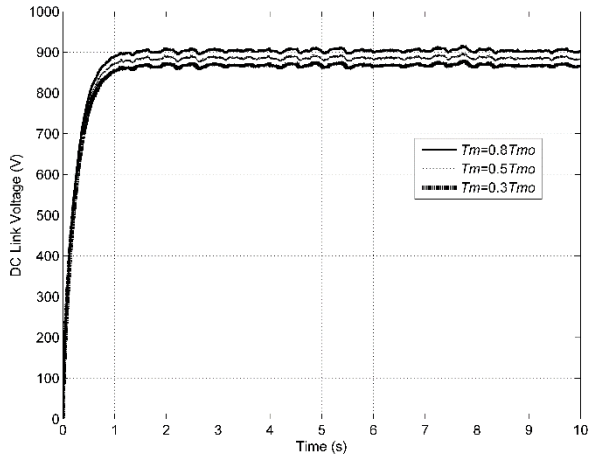

Figure 3.9. DC link voltage response during varying input mechanical torques

The DC converter current I_{dc} during Steady State (SS), SSCF, and LSCF with perturbed generator parameters is presented in Figure 3.10. The controller takes five seconds for the current to settle down in steady-state. This output response shows variations in peak-time and overshoot during SSCF and LSCF. Similar output response occurs for the PMSG rotor speed during parameter variations and faults. The rotor speed response is described in Figure 3.11.

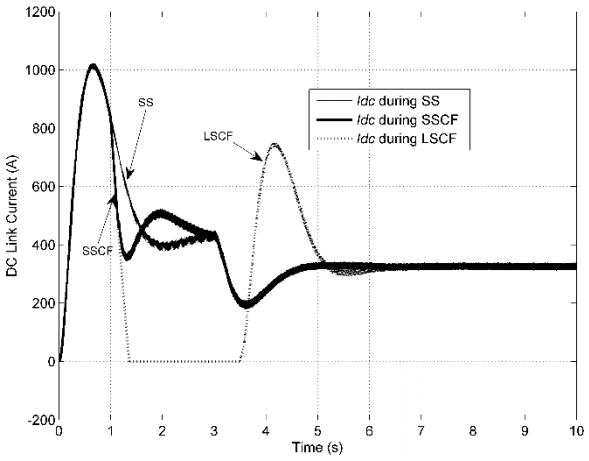

Figure 3.10. DC link converter current (A)

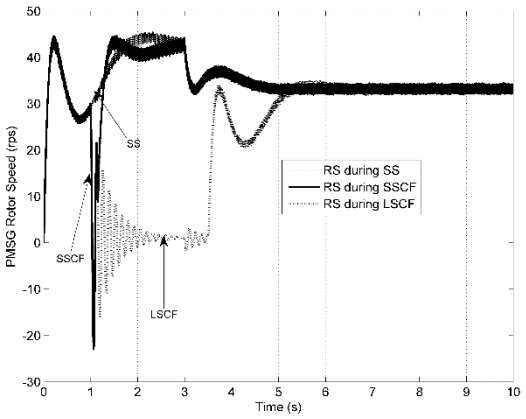

Figure 3.11. PMSG rotor speed (RPM)

The authors in [3.8] simulated the aforesaid model with generator parameter perturbations and variations in input mechanical torque. The parameter variations were shown separately in each plot of Rotor Speed (RS). We simulated the same system with multiple variations of generating parameters at the same time. Moreover, we provided the rotor speed, converter current, and DC link voltage during Steady State (SS), SSCF, and LSCF with perturbed generator parameters. Furthermore, the effect of rotor speed control on other parameters of the PMSG Boost, detailed discussion on the control law, and local subsets associated with the stability were not analyzed by the authors in [3.8]. We provided a detailed

technical discussion on the output response of the system due to non-linear functions. The critical and theoretical analysis of our simulation results are more versatile than the simulation results of the authors in [3.8].

In the areas of high wind speeds, the PMSG Boost will perform a stable operation with small variations in the output. The stability issues associated with the non-linear control performance of the PMSG Boost are: feasibility placement, Computational burden, associated computational cost for further linearization, low stability level against varying input torques and short-circuit faults, and small variations in the output DC link voltage.

3.7. Simulation Results of the PMSG Rectifier-Inverter

The PMSG Rectifier-Inverter is implemented and interfaced with the grid section in the back to back converter topology. The three-phase line to ground faults (SSCF and LSCF) across the grid-side is introduced in the PMSG Rectifier-Inverter. The generator parameters, such as inertia, friction, and stator resistance values are also perturbed from the nominal values to 1.5 times of the rated machine values to validate the stability and performance of the PMSG Rectifier-Inverter controller. The output DC link voltage maintains a steady state value, as shown in Figure 3.12. The robustness level of the PMSG Rectifier-Inverter against the SSCF and LSCF faults is more than the PMSG Boost. The stability of the PMSG Rectifier-Inverter is further verified by comparing the output DC link voltage response between the PI (linear) controller and the EFL (non-linear) controller with the minimum and maximum varying input torques. The input torque was varied between 30% (maximum) and 80% (minimum) of the rated torque values for the validation of the model. The settling time, accuracy and output stability of the PMSG Rectifier-Inverter under fast varying dynamics was improved by using the EFL controller compared to the PI controller. The EFL controller is able to maintain the steady DC link voltage

for the aforementioned input torque variations, as shown in Figure 3.13, Figure 3.14, and Figure 3.15. However, the classical PI controller starts producing the unstable and abrupt responses to the varying torques.

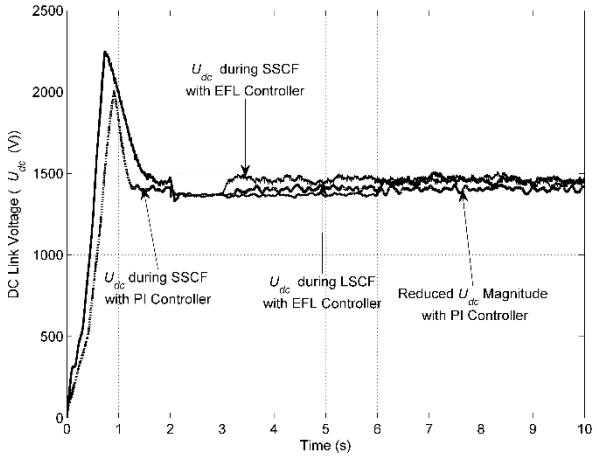

Figure 3.12. The DC link voltage during the SSCF and LSCF faults with perturbed generator parameters

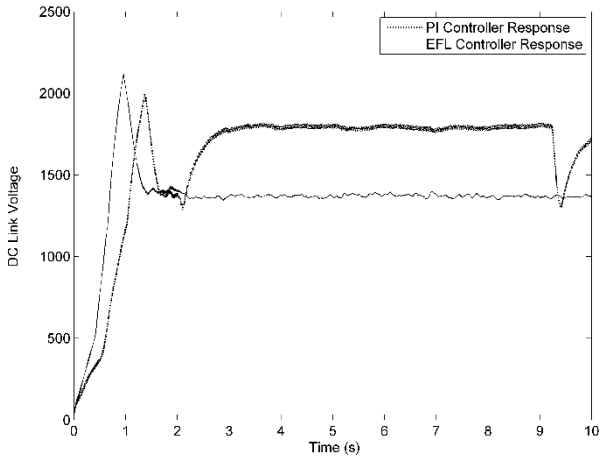

Figure 3.13. The DC link voltage of the PMSG Rectifier-Inverter during 30% of the rated input torque

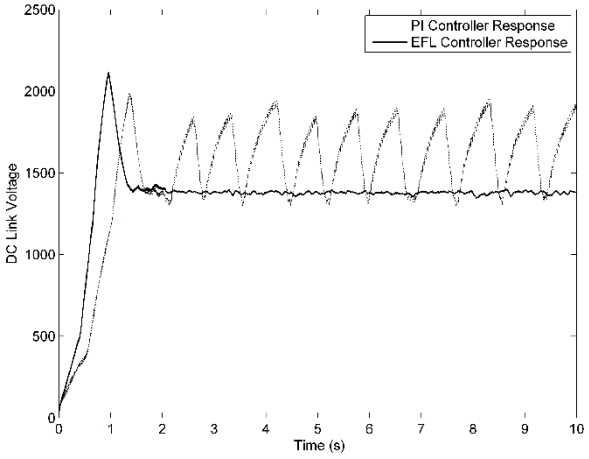

Figure 3.14. The DC link voltage of the PMSG rectifier-inverter during 50% of the rated input torque

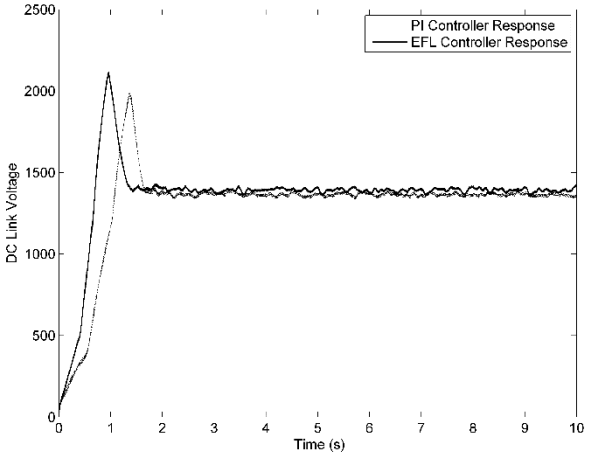

Figure 3.15. The DC link voltage of the PMSG rectifier-inverter during 80% of the rated input torque

The PMSG rotor speed is compared between EFL scheme and PI scheme. The rotor speed is analyzed during SS, SSCF, and LSCF. The rotor speed drifts away from the rated speed during SSCF with PI control. The graphical analysis of the rotor speed is described in Figure 3.16. The output function of the state-feedback law is quadrature component of the stator current I_q . The variation in I_q is analyzed in subplots (a), (b), and (c) during SS, SSCF, and LSCF with the EFL control scheme, while I_q response with PI control is highlighted in (d). The

above mentioned results are presented in Figure 3.17. During short-circuit grid fault, voltage sag is created which effects the inter-connected network. The WECS must "ride through" the faulty-period and provide required power support. In case of SSCF, the active power and reactive power transferred to the grid through the EFL control scheme is presented in Figure 3.18.

The comparative analysis of the PMSG Rectifier-Inverter using the EFL is much better than the conventional PI scheme. With PI control, the output response of various parameters, such as DC link voltage possesses increased settling time, less accuracy, and slow output response. Through EFL, the regulated parameters have higher accuracy, stabilized control, optimized performance, and high robustness in the presence of electrical and mechanical disturbances. The control performance of the above mentioned model is enhanced using differential game, non-linear coordinate transformations, geometrical-space linearization, and Lie-algebra simplifications. The PMSG Rectifier-Inverter with an EFL control under varying non-linear dynamics is more suitable for wind energy applications.

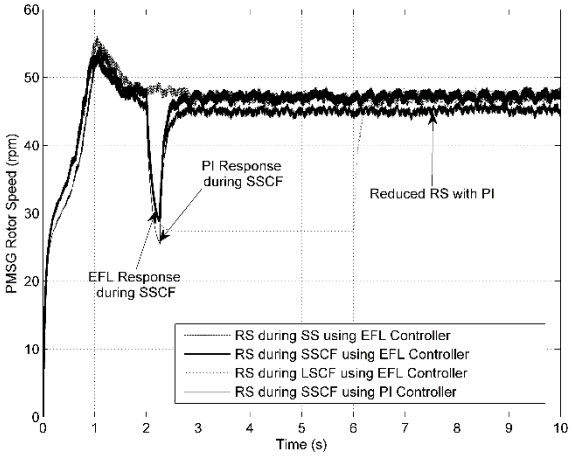

Figure 3.16. PMSG rotor speed. The plot shows rotor speed during SS, SSCF, LSCF with EFL control, and rotor speed during SSCF with PI control

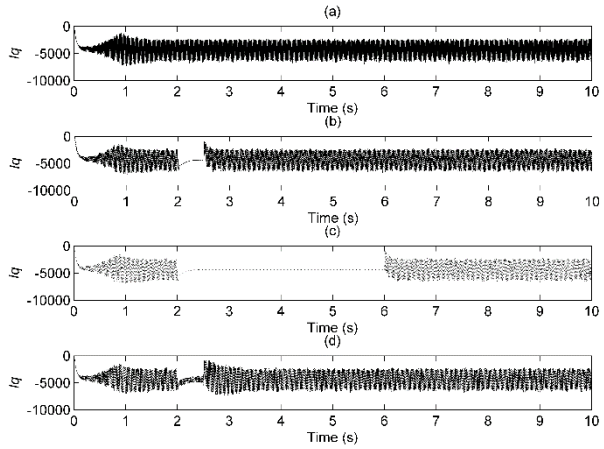

Figure 3.17. Quadrature-axis current. The subplot (a) shows I_q during SS with EFL, (b) shows I_q SSCF with EFL, (c) shows I_q during LSCF with EFL, and (d) shows I_q during SSCF with PI control

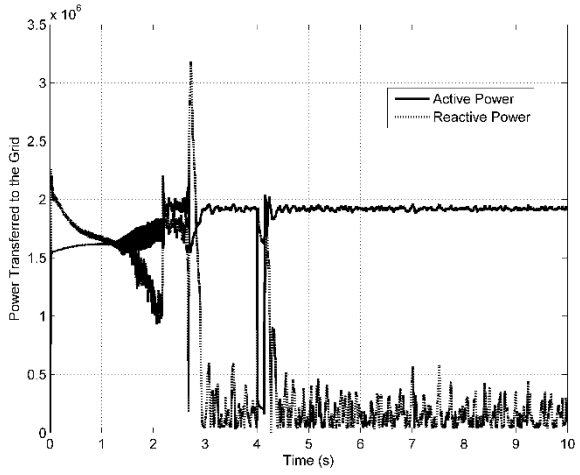

Figure 3.18. Active power and reactive power transferred to the grid

The comparison of the PMSG Boost and PMSG Rectifier-Inverter based on the control responses obtained through the EFL scheme is also listed in Table 3.4. The Table 3.4 highlights that control features of the PMSG Rectifier-Inverter, such as stability, optimization level, placement feasibility, and robustness level dominates the PMSG Boost. The output responses of both of the PMSG models are compared based on the local stability subsets, derived control laws, local linearization, and output response of the DC link voltage from the respective

converter systems. The comparison justifies the performance and the effectiveness level of the PMSG Rectifier-Inverter for the wind energy applications

Table 3.4. Comparison of PMSG boost and PMSG rectifier-inverter

Control Features	PMSG Boost	PMSG Rectifier-Inverter
Robustness level	Low	High
System stability	Low	High
Mathematical complexity	High	High
Computational burden	High	High
Reliability	Low	High
Optimization level	Low	High
Self-Tuning capability	High	High
Parameter sensitivity	High	Medium
Control law stability	Local	Local
Computational cost	High	Medium
Grid-Interface performance	Low	High
Placement area	Constant high windy	Low, medium, and high windy
Applications	Local and Global controls	Local and Global controls

Table 3.5. Comparison of PI and EFL

Control Features	PI	EFL
Robustness level	Low	High
System stability	Low	High
Mathematical complexity	Low	High
Computational burden	Low	High
Reliability	Low	High
Optimization level	Low	High
Self-Tuning capability	None	High
Parameter sensitivity	Low	High
Control law stability	Low	High
Computational cost	Low	High
Grid-Interface performance	Low	High
Settling time	Slow	Fast
Accuracy level	Low	High
Applications	Limited in WECS	Wide in WECS

With PI control, the output response of various parameters, such as DC link voltage possesses increased settling time, less accuracy, and slow output response. The comparison of the PMSG Boost and PMSG Rectifier-Inverter based on the control responses obtained through the EFL scheme is also listed in Table 3.4. The Table 3.4 highlights that control features of the PMSG Rectifier-Inverter, such as stability, optimization level, placement feasibility, and robustness level dominates the PMSG Boost. . Moreover, comparative features of the EFL and PI evaluated in this paper is summarized in Table 3.5.

3.8. References

[3.1] S. Louarem, S. Belkhiat, D. Belkhiat, "A control method using PI/fuzzy controllers based DFIG in wind energy conversion system," in *Proc. IEEE PowerTech (POWERTECH)*, 2013, pp. 1-6.

[3.2] M. Cespedes, J. Sun, "Modeling and mitigation of harmonic resonance between wind turbines and the grid," in *Proc. IEEE Energy Conversion Congress and Exposition (ECCE)*, 2011, pp. 2109-2116.

[3.3] E. Iyasere, M. Salah, D. Dawson, J. Wagner, E. Tatlicioglu, "Optimum seeking-based non-linear controller to maximize energy capture in a variable speed wind turbine," *IET Control Theory and Applications*, vol. 6, no. 4, pp. 526-532, 2012.

[3.4] B. Ramasamy, A. Palaniappan, and S. Yakoh, "Direct-drive low-speed wind energy conversion system incorporating axial-type permanent magnet generator and Z-source inverter with sensorless maximum power point tracking controller," *IET Renewable Power Generation*, vol. 7, no. 3, pp. 284-295, 2013.

[3.5] H. Huang, and C. Chung, “Adaptive neuro-fuzzy controller for static VAR compensator to damp out wind energy conversion system oscillation,” *IET Generation, Transmission and Distribution*, vol. 7, no. 2, pp. 200-207, 2013.

[3.6] M. Haque, M. Negnevitsky, and M. Muttaqi, “A novel control strategy for a variable speed wind turbine with PMSG,” *IEEE Trans. Ind. Applications.*, vol. 46, no. 1, pp. 331-339, 2010.

[3.7] A. Howlader, N. Urasaki, A. Yona, T. Senjyu, and A. Saber, “A new robust controller approach for a wind energy conversion system under high turbulence wind velocity,” in *Proc. IEEE Industrial Electronics and Applications (ICIEA) Conf.*, 2012, pp. 860-865.

[3.8] C. Xia, Q. Geng, X. Gu, T. Shi, and Z. Song, “Input-Output feedback Linearization and speed control of a surface permanent magnet synchronous wind generator with the boost chopper converter,” *IEEE Trans. Ind. Electronics*, vol. 59, no. 9, pp. 3489-3500, 2012.

[3.9] F. Delfino, F. Pampararo, R. Procopio, and M. Rossi, “A Feedback Linearization Control Scheme for the Integration of Wind Energy Conversion Systems into Distribution Grids,” *IEEE J. Syst.,* vol. 6, no. 1, pp. 85-93, 2012.

[3.10] V. Yaramasu, and B. Wu, “Predictive Control of a Three-Level Boost Converter and an NPC Inverter for High-Power PMSG-Based Medium Voltage Wind Energy Conversion Systems,” *IEEE Trans. on Power Electronics*, vol. 29, no. 10, pp. 5308-5322, 2014.

[3.11] Q. Lu, Y. Sun, and S. Mei, *Non-linear control system and power system dynamics*, Kluwer Academic Publishers, 2001, pp. 165-170.

[3.12] Y. Wang, Z. Xia, and T. Zhang, “Sliding mode variable structure control based on exact linearization mode of nonlinear system,” in *Proc. IEEE Intelligent Control and Automation (WCICA) Conf.*, 2012, pp. 2878-2881.

[3.13] R. Brockett, “Feedback Invariants for non-linear systems,” in *Proc. 7th IFAC World Congress, Helsinki*, June 1978.

[3.14] B. Jakubczyk, and W. Respondek, *On linearization of control systems*, Bulletin de L`acadenie Polonaise des Sciences, 28, 1980.

[3.15] D. Kim, and D. Lee, “Feedback Linearization control of three phase UPS inverter Systems,” *IEEE Trans. Ind. Electronics*, vol. 57, no. 3, pp. 963-968, 2010.

4. COMPARITIVE ANALYSIS OF FAULT RIDE THROUGH SCHEMES FOR GRID INTERFACED DFIG-WT

4.1. Overview

The unprecedented growth rate of wind power production in recent years has attracted the attention of scientists and engineers. In deregulated energy market, the integration of Wind Turbine (WT) with grid network is a demanding task. Among various WTs, Doubly Fed Induction Generator (DFIG)-WT has gained more popularity due to various promising features, such as (a) high energy efficiency, (b) wide range of speed variation, (c) low converter rating, (d) independent control of active and reactive power, (e) reduced converter rating, (f) lower mechanical stress, and (g) improved power quality [4.1]. The model of grid interfaced DFIG-WT is shown in Figure 4.1.

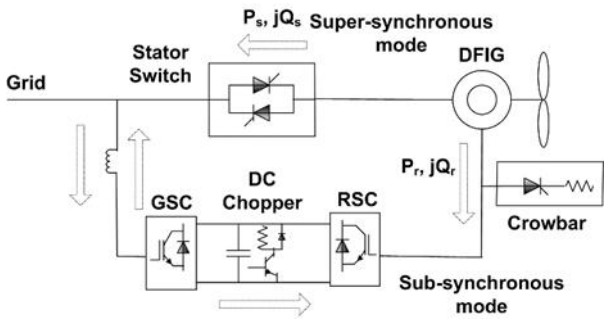

Figure 4.1. DFIG-WT interface with grid network

4.1.1. Motivation

With increasing integration of WTs into the grids, stability and steady-state performance are the alarming issues in presence of symmetrical and asymmetrical short-circuit grid faults. In extreme cases of voltage dips, the inter-connected system will result in widespread tripping of the DFIG. Moreover, voltage instabilities will cause overcurrent and overvoltage in Rotor Side Converter (RSC), Grid Side Converter (GSC) and DC link capacitor. Furthermore, this will lead to the destruction of the power sensitive components and de-stabilize the voltage and reactive

power support by the WT at Point of Common Connection (PCC). To address the aforesaid challenging problem, various utilities have revised the grid-code requirements for the stable operation of WTs during Fault-Ride-Through (FRT).

The minimum grid-code requirements for FRT operation during grid fault must be followed by the DFIG-WT. The minimum FRT grid-code specification is depicted in Figure 4.2 [4.2]. In Figure 4.2, tdip is the maximum allowable duration during which DFIG-WT must be connected to the grid network, while Vr is the minimum retaining voltage. The main objectives of FRT scheme are: to restore active and reactive power control during fault-initiation and clearance, to divert or negate rotor overcurrent, and to minimize the voltage drop at the generator.

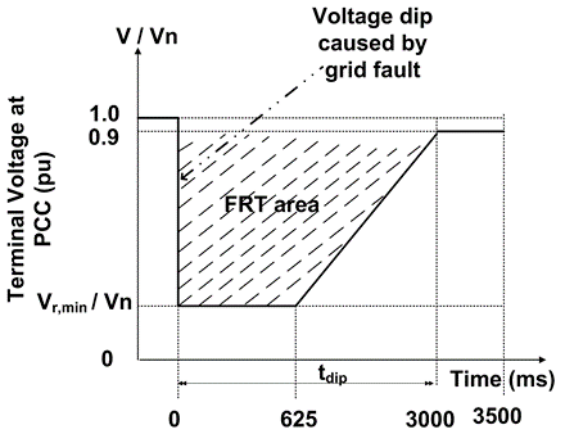

Figure 4.2. FRT specification curve of grid-interfaced DFIG

4.1.2. Contributions

We propose a Hybrid FRT Strategy. Different from conventional FRT schemes, our Hybrid model provides more stable and robust performance under symmetrical and asymmetrical grid faults of 300ms (transient-period). Moreover, effectiveness of our model is validated using thorough transient analysis of various dynamical parameters of the DFIG-WT. We believe that our research work is more versatile and covers a broad domain of FRT scheme for DFIG-WT.

The main contributions of our paper in the light of above stated issues are: (1) our Proposed Hybrid FRT Strategy consists of: (a) STFCL model, (b) Active Rotor crowbar, (c) DC chopper circuit, and (d) RSC control and GSC control models, (2) performance of the FRT strategies are analysed under: (a) symmetrical fault (3Φ-g) and (b) asymmetrical faults, such as single-phase to ground (Φ-g) fault, double-phase to ground (2Φ-g) fault, and double-phase (2Φ) fault. Moreover, sequence component analysis (positive and negative) is presented for most critical controlling parameters, (3) thorough stability analysis of varying parameters is investigated during transient period. Stability analysis includes maximum transient peak at fault initiation, fault-clearance period, rotor overvoltage, and dips in grid voltages, and (4) comparative assessment of the proposed strategy is evaluated with various active strategies, namely: (a) Strategy A [4.2]-IGBT based active rotor crowbar with RSC and GSC control, (b) Strategy B [4.3]-DC chopper circuit, rotor crowbar, and RSC and GSC control, (c) Strategy C [4.4]-STFCL for FRT operation.

The remainder of the chapter is structured as follows. Section 4.2 presents modelling of the DFIG-WT and grid fault analysis for FRT operation. Section 4.3 highlights the control design of the Hybrid FRT strategy. Performance evaluation of the above mentioned strategies are elaborated in Section 4.4.

4.2. Modelling of the DFIG-WT and Grid Fault Analysis

The grid-interfaced DFIG-WT model is presented in Figure 4.3. The primary objective of the DFIG is to provide voltage and reactive power support and optimum-ride-through operation in case of grid faults. The rotor supplies power to the grid and receives power from the grid through AC/DC/AC power converter system. The converter system consists of three electronic components, such as RSC, DC link capacitor, and GSC. The RSC and GSC exhibits fast

switching characteristics of IGBT/Diodes circuitry with low switching and conduction losses. The switching controls of the aforesaid converter is provided by a control system that generates triggering pulses for RSC and GSC. The dynamic model of grid interfaced DFIG will be presented in the following sub-sections.

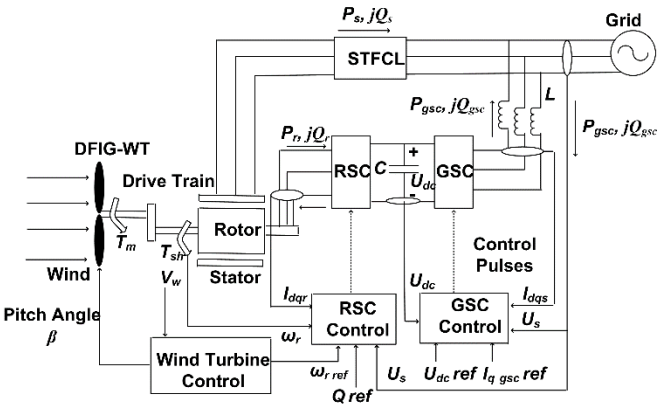

Figure 4.3. Grid-interfaced DFIG-WT for FRT operation

4.2.1. Stator and Rotor Model

In *d-q* frame of reference rotating at synchronous speed, the stator and rotor voltages of the DFIG are described as [4.5]:

$$U_s = U_{ds} + jU_{qs}, \tag{4.1}$$

$$U_r = U_{dr} + jU_{qr}.$$

In Eqn. (1), U_s and U_r are the stator and rotor voltages, U_{ds} and U_{qs} are the direct and quadrature axis stator voltages, U_{dr} and U_{qr} are the direct and quadrature axis stator voltages. The expressions of U_{ds} , U_{qs} , U_{dr} and U_{qr} are expressed as:

$$U_{ds} = R_s i_{ds} - \omega_s \varphi_{qs} + \frac{1}{\omega_b}\frac{d\varphi_{ds}}{dt}, \tag{4.2}$$

$$U_{qs} = R_s i_{qs} + \omega_s \varphi_{ds} + \frac{1}{\omega_b}\frac{d\varphi_{qs}}{dt},$$

$$U_{dr} = R_r i_{dr} - (\omega_s - \omega_r)\varphi_{qr} + \frac{1}{\omega_b}\frac{d\varphi_{dr}}{dt},$$

$$U_{qr} = R_r i_{qr} + (\omega_s - \omega_r)\varphi_{dr} + \frac{1}{\omega_b}\frac{d\varphi_{qr}}{dt}.$$

In Eqn. (2), R_s and R_r are the stator and rotor resistances, ω_s and ω_r are the angular frequencies of stator and rotor, ω_b is the base angular frequency, and φ_{ds}, φ_{qs}, φ_{dr}, and φ_{qr} are the flux linage of stator and rotor. Consider i_s and i_r are the stator and rotor currents and i_{ds}, i_{qs}, i_{dr}, and i_{qr} are the direct and quadrature axis components of stator and rotor currents. The simplified equations of i_s, i_r, φ_s, and φ_r are described as:

$$i_s = i_{ds} + j i_{qs}, \tag{4.3}$$

$$i_r = i_{dr} + j i_{qs},$$

$$\varphi_s = \varphi_{ds} + \varphi_{qs},$$

$$\varphi_r = \varphi_{dr} + \varphi_{qr}.$$

The drive train model consists of turbine blades, turbine shaft, and gear box mechanism of the WT. The parameters for modeling drive train mechanism include generator inertial constant J_g, turbine inertial constant J_t, friction coefficient B, shaft damping D_{sh},shaft twist θ_t, electromagnetic torque T_{em}, T_m , and T_{sh}. For analyzing drive train model, two-mass model is defined as:

$$\frac{d\omega_r}{dt} = \frac{1}{2J_g}(T_{sh} - T_{em} - B\omega_r), \tag{4.4}$$

$$\frac{d\theta_t}{dt} = \omega_b(\omega_t - \omega_r),$$

$$\frac{d\omega_t}{dt} = \frac{1}{2J_t}(T_m - T_{sh}),$$

$$T_{em} = L_m\left(i_{qs}i_{dr} - i_{ds}i_{qr}\right),$$

$$T_{sh} = K_{sh}\theta_t + D_{sh}\omega_b(\omega_t - \omega_r),$$

$$T_m = \frac{P_m}{\omega_t}.$$

Consider ρ as the air density, R is the radius of the blades and λ is the blade tip-speed ratio. Pitch angle β of the WT blade and tip-speed ratio λ are the contributing factor for the performance coefficient C_p, as $C_p = f(\beta, \lambda)$. The expression of P_m is explored as:

$$P_m = \frac{1}{2}\left(\rho\pi R^2 C_p(\lambda, \beta)V_w^3\right), \tag{4.5}$$

$$\lambda = \left(\frac{\omega_t R}{V_w}\right),$$

$$C_p = 0.22\left(\frac{116}{\lambda_i} - 0.4\beta - 5\right)e^{\left(-\frac{12.5}{\lambda_i}\right)},$$

$$\lambda_i = \frac{1}{\left(\frac{1}{(\lambda + 0.08\beta)} - \frac{0.035}{\beta^3 + 1}\right)}.$$

The output power of DFIG-WT depends on turbine speed. The power-speed characteristics of DFIG is depicted in Figure 4.4. The WT operates in four basic regions. In Region 1, no mechanical power will be produced due to low wind speed. In Region 2, sub-rated power will be produced, existing between cut-in speed and rated speed. In Region 3, rated power will be produced, while no power will be produced in Region 4 for mechanical safety. The tracking speed of WT is characterized by points A, B, C, and D. At point A, generated output power will be zero. At cut-in point, minimum turbine power will be produced. Along points A-B, the turbine power will start increasing with increased wind speed. The wind speed at point B is greater than wind speed at point A. The maximum power of the WT is tracked along the locus between points B-C. From points C to D, tracking characteristic is a straight line highlighted by

Region 3. At point D, turbine power will be maximum and WT operated in shutdown mode automatically beyond point D, indicated by Region 4.

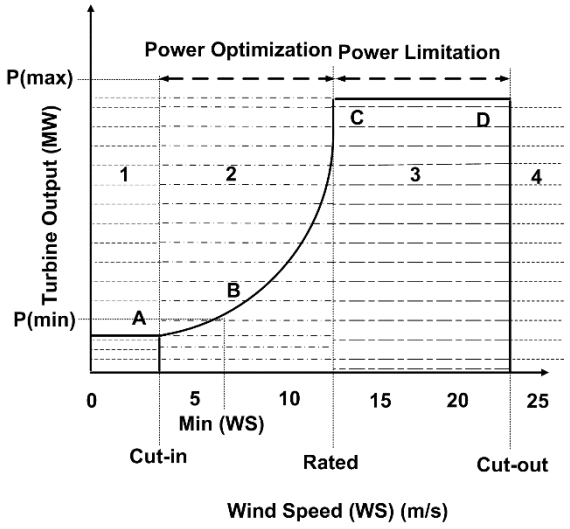

Figure 4.4. DFIG-WT power-speed characteristic curve (β=0^0)

The one-line diagram of grid-interfaced DFIG-WT is shown in Figure 4.5. We used IEEE 5 bus system interfaced with 9 MW DFIG using standard electrical component blocks in Matlab/Simulink. Short-circuit grid fault occurs on a 25 Km short transmission line (25 KV), denoted by an arrow. The voltage at Grid Connection Point (GCP) during fault period is elaborated, considering voltage dips at Point of Common Connection (PCC). The FRT Strategies are simulated and critically analyzed under grid faults.

Consider a voltage divider network of Figure 5(b). Source impedance and fault impedance are denoted by Z_s and Z_f. When fault occurs near GCP, than voltage at GCP U_{gcp} is defined as: $U_{gcp} = \left(\frac{Z_f}{Z_s+Z_f}\right) U_{g,x}$, where $U_{g,x(a,b,c)}$ symbolize pre-fault voltage. The simplified expressions for symmetrical and asymmetrical fault are presented in Table 4.1. The term λ indicates the relative fault distance (1.27 pu), while α denotes an impedance angle. The value of α depends on the type of network (0^0 for transmission system, -20^0 for distribution system, and -

60^0 for wind farms). For simplicity, positive and negative impedances are considered identical as: $Z_{s+} \approx Z_{s-} = Z_s,\ Z_{f+} \approx Z_{f-} = Z_f$. We assume that DFIG is operating in steady-state condition before the asymmetrical fault. Let initial steady-state operation is achieved at time t_o and asymmetrical fault is analyzed during time t_f. The intensity of positive and negative-sequence components during fault is symbolized as p and n, while $\theta_1$are θ_2 the phase-angle jumps of sequence components. The positive and negative-sequence grid voltages at GCP are defined in Table 4.1.

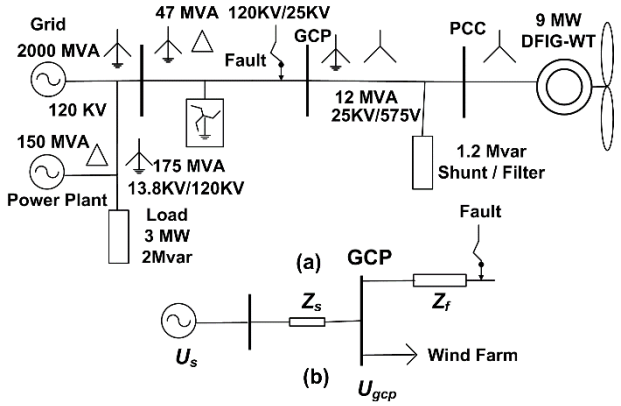

Figure 4.5. One-line diagram of grid-interfaced DFIG-WT

This stator voltage will induce positive and negative-sequence stator fluxes in the grid-interfaced DFIG-WT that will induce sequence-stator currents. During asymmetrical fault, the rotor voltage is defined using rotor frame of reference is described in Table 4.1.

4.3. Proposed Hybrid Control strategy For FRT

When Wind Energy Conversion System (WECS) experiences a voltage dip, transients are produced that influence the stability of inter-connected system very badly. During this period, low voltage prevents the power transfer capability of DFIG-WT, resulting in overvoltage and overcurrent in stator and rotor circuitry. To protect RSC, GSC, and DC link capacitor from overvoltage and overcurrent is a primary objective of FRT. Moreover, DFIG-WT must be

connected to the grid for providing sufficient voltage and active and reactive power support. Furthermore, stability and steady-state performance is quickly desired when the fault-time is over. Due to GCP fault, the voltage at PCC falls suddenly, stabilizes for very short-time, and then recovers for stability. At the point of fault-initiation and clearance, maximum transient peaks of rotor current and voltages are generated. With voltage dip at PCC, sudden change of stator flux results in rotor current oscillations.

In view of above mentioned issues, we proposed Hybrid control strategy, described in Figure 4.3. The proposed scheme provides robust control structure of protection, monitoring, low voltage ride-through, and voltage and current management for sensitive power electronic circuitry. Our proposed strategy damp out rotor oscillations during fault-initiation and clearance by cutting-off the energy injection in the rotor circuit. The active control mechanism includes: (a) STFCL stator switch, (b) Rotor crowbar (c) IGBT based DC chopper control, (d) Pitch servo control, (e) RSC control, and (f) GSC control. In stator switch scheme, STFCL is used that comprises of IGBT switch, current limiting inductors, snubber capacitor, and fault energy absorbers [4.5]. The control of DC chopper during grid faults is described by the authors in [4.6]. The description of pitch control, RSC control, and GSC control is elaborated in the following sub-sections.

4.3.1. Pitch Servo Control Model

The WT pitch control model is presented in Figure 4.6. It is used for controlling power extraction during over-speeding of rotor above rated value. By providing a dynamic resistive crowbar control, overcurrent in rotor windings is dissipated with RSC open-circuited [4.7].

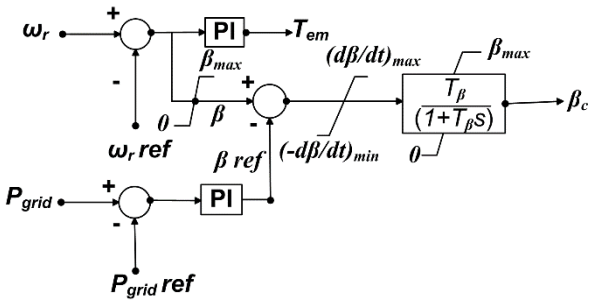

Figure 4.6. Pitch servo control model

Table 4.1. Fault expression for symmetrical and asymmetrical faults

Case	Positive-Seq. Fault Expression)	Negative-Seq. Fault Expression
Φ-g	$\vec{U}_{(gcp)+} = \frac{1}{3}U_g\left(3 - \frac{1}{1+\lambda e^{(j\alpha)}}\right)$	$\vec{U}_{(gcp)-} = -\frac{1}{3}U_g\left(\frac{1}{1+\lambda e^{(j\alpha)}}\right)$
2Φ-g	$\vec{U}_{(gcp)+} = U_g\left(1 - \frac{2}{3}\left(\frac{1}{1+\lambda e^{(j\alpha)}}\right)\right)$	$\vec{U}_{(gcp)-} = \frac{1}{3}U_g\left(\frac{1}{1+\lambda e^{(j\alpha)}}\right)$
2Φ	$\vec{U}_{(gcp)+} = U_g\left(1 - \frac{1}{2}\left(\frac{1}{1+\lambda e^{(j\alpha)}}\right)\right)$	$\vec{U}_{(gcp)-} = \frac{1}{2}U_g\left(\frac{1}{1+\lambda e^{(j\alpha)}}\right)$
3Φ-g	$U_{gcp} = U_{g,x}\left(\frac{\lambda e^{(j\alpha)}}{1+\lambda e^{(j\alpha)}}\right)$	
$\vec{U}_s$	$\vec{U}_{s+} = \begin{pmatrix} e^{j\omega t_f}, t_0 < 0, \\ (1-p)e^{j(\omega t_f+\theta_1)}, t_0 \geq 0, \end{pmatrix}$,	$\vec{U}_{s-} = \begin{pmatrix} 0\,, t_0 < 0, \\ ne^{-j(\omega t_f+\theta_2)}, t_0 \geq 0, \end{pmatrix}$
$\vec{\varphi}_s$	$\vec{\varphi}_{s+} = \begin{pmatrix} \frac{1}{j\omega}e^{j\omega t_f}, t_0 < 0, \\ \frac{(1-p)}{j\omega}e^{j(\omega t_f+\theta_1)}, t_0 \geq 0, \end{pmatrix}$	$\vec{\varphi}_{s-} = \begin{pmatrix} 0\,, t_0 < 0, \\ \frac{n}{-j\omega}e^{-j(\omega t_f+\theta_2)}, t_0 \geq 0, \end{pmatrix}$
$\vec{U}_r$	$\vec{U}_r = \frac{L_m}{L_s}\left(\frac{d\vec{\varphi}_s}{dt}\right) + \left(R_r\vec{\imath}_r + \left(\sigma = 1 - \left(\frac{L_m^2}{L_sL_r}\right)\right)L_r\frac{d\vec{\imath}_r}{dt}\right)$	

In contrast to overvoltage and overcurrent protection [4.6], Hybrid control strategy will convert increased rotor power into Kinetic Energy (KE) of WT, slightly increasing the rotor speed and damping the oscillations. During high wind speeds, pitch control will decrease the required wind power extraction to ensure mechanical safety.

The mathematical model of pitch control is described as:

$$\frac{d\beta}{dt} = \frac{T_\beta}{1 + T_\beta s}\left(\beta - \beta_{ref}\right). \tag{4.6}$$

4.3.2. RSC Control Model

Our proposed scheme will ensure controllability of RSC and GSC during short-circuit faults, which is completely lost in conventional schemes [4.8]. The RSC control model is depicted in Figure 4.7. Electromagnetic torque oscillations and overcurrent protection is achieved using Proportional Integral (PI) controllers. We considered *d-q* axis orientation of the stator fluxes and rotor currents in torque control and var control loops. The *d-q* voltages of rotor are converted to triggering pulses of rotor side converter U_{rscc} after passing through Space Vector Pulse Width Modulation (SVPWM) control block.

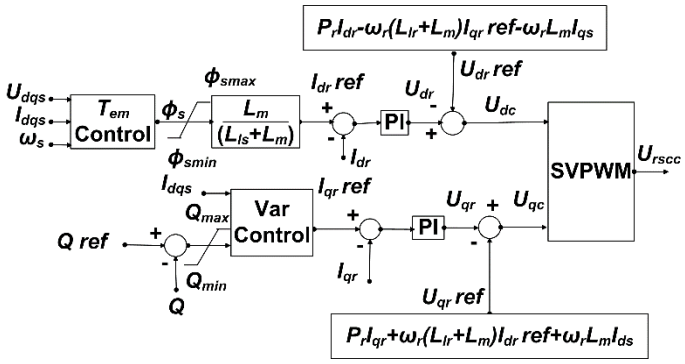

Figure 4.7. RSC control model

4.3.3. GSC Control Model

The GSC control model is presented in Figure 4.8. Power imbalance results from FRT operation that causes increased DC link voltage U_{dc} and grid side converter current I_{gsc}. During steady-state operation, the value of DC link voltage is constant. When grid fault occurs, current miss-match occurs between grid side converter current i_{gsc} and rotor side converter current i_{rsc}. The SVPWM scheme will produce control pulses of GSC U_{gscc} for safe operation during FRT. This is described in Figure 4.8.

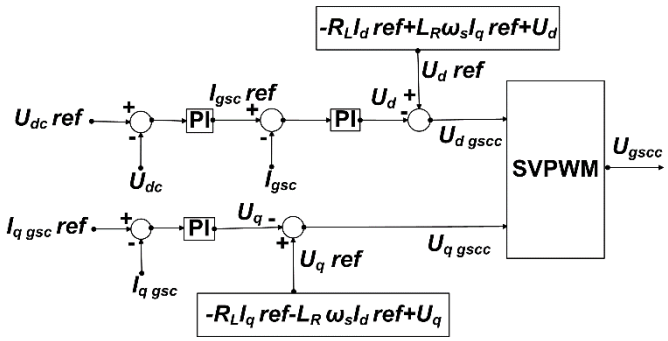

Figure 4.8. GSC control model

The expression of DC link voltage is defined as:

$$\frac{dU_{dc}}{dt} = \frac{1}{C_{dc}}\left(i_{gsc} - i_{rsc}\right). \tag{4.7}$$

4.4. Performance Evaluation

4.4.1. Symmetrical Analysis

Four FRT Strategies are compared using 9MW DFIG-WT interfaced with grid (IEEE 5 Bus System) is shown in Figure 4.5 using Matlab/Simulink. The rated wind speed in each evaluation is 11m/s. Short-circuit fault occurs on 25KV transmission line for 300ms. The parameters of DFIG-WT model are listed in Table 4.2. The Strategies compared critically are described as: (1) Strategy A: Active rotor crowbar, (2) Strategy B: DC Chopper control with rotor crowbar, (3) Strategy C: STFCL stator switch, and (4) Strategy D: Hybrid control (proposed).

For fair comparison, the aforesaid Strategies are implemented with pitch control, RSC control, and GSC control mechanism. Short-circuit three-phase to ground faults occurs for 300ms. At time *t*=0.3s, fault is initiated, dynamic responses of grid-interfaced DFIG-WT is shown in Figure 4.9. All currents must be lower than twice the rated values, DC link voltage variance must be less than 15% of rated value, rotor speed must be within 70% to 130% of rated values, and power ratings of the RSC and GSC must be lower than 30% of DFIG rated power

capability [4.20]. Various critical parameters of grid-side and machine-side systems are discussed to evaluate the performance of Strategies A, B, C, and D. The parameters include rotor variables, power converter variables, grid voltage, and grid current. The variation in the controlling parameters during grid faults will describe the comparative response of the Strategies.

Figure 4.9(a) shows that Strategies A, B, and C produces 99.6% grid voltage dip U_g, while Strategy D has 85% voltage dip with 0.15pu voltage support in accordance with grid-code requirements [4.2]. Strategies A and B produces maximum transients during fault start-time and end-time of I_g , as described in Figure 4.9(b). Moreover, abrupt response is shown by Strategies A, B, and C during fault, however, Strategy D presents a stable current response during fault in presence of power-imbalance during voltage dip. Regarding rotor voltage U_r, Strategies A and B produces maximum transient peaks during fault initiation, while Strategies C and D have lower transient peaks. However, high frequency oscillations (0.04pu) are illustrated using Strategies A, B, and C, while in case of Strategy D, low frequency oscillations (0.01pu) are depicted in Figure 4.9(c). Similarly, rotor overcurrent for Strategies A and B is clear in Figure 4.9(d), however, low oscillations exists for Strategy C, while due to increased KE in WT, this value is reduced to zero for Strategy D. Figure 4.9(e) describe U_{dc}, which is reduced to zero in case of Strategies A, B, and C with high transient peaks. Strategy D possesses smooth DC link voltage response during fault initiation and clearance, which presents controllability of RSC and GSC during fault. T_{em} for Strategy D is zero during fault because of temporary increasing rot Strategies A, B, and C shows abrupt response when fault is initiated and unstable response during fault interval. The aforesaid increase in rotor speed for Strategy D is described in Figure 4.9(g). or speed resulting in damping of current and torque oscillations, as presented in Figure 4.9(f).

Table 4.2. Machine parameters

DFIG Parameters	Values
Rated power	9 MW
Nominal stator voltage	575 V
System frequency	60 Hz
Slip	-10% (-251.28 rad/s)
Pole pairs	3
Stator resistance	0.023 pu
Rotor resistance	0.016 pu
Magnetizing inductance	2.9 pu
Rated wind speed	11 m/s
Rated torque	0.83 pu
Rated DC link voltage	1150 m/s
DC link capacitance	$10000*10^{-6}$ F
Switching frequency	20 KHz
RSC gains (K_p, K_i)	0.6, 8
GSC gains (K_p, K_i)	0.83, 5
Speed regulator gains (K_p, K_i)	3, 0.6
Pitch compensation gains (K_p, K_i)	3, 30

Strategy D provides active power support of 0.05pu to the grid at PCC, while Strategies A, B, and C do not comply grid-codes, as illustrated in Figure 4.9(h). Figure 4.9(i) shows Strategy D reactive power support of 0.1pu during voltage drop (super-synchronous mode with slip $s < 0$), while Strategies A, B, and C absorbs power from grid operating in sub-synchronous mode ($s > 0$).

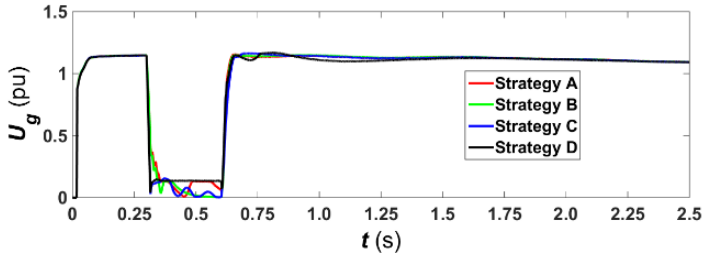

(a)

Figure 4.9. Grid-interfaced DFIG-WT response during symmetrical fault with voltage dip 85% and wind speed is 11m/s (a) Variation of grid voltage, (b) Variation of grid current, (c) Variation of rotor voltage, (d) Variation of rotor current, (e) Variation of DC link voltage, (f) Variation of elecromagnetic torque, (g) Variation of roror speed, (h) Variation of active power support at PCC, and (i) Variation of reactive power exchanged with grid at PCC

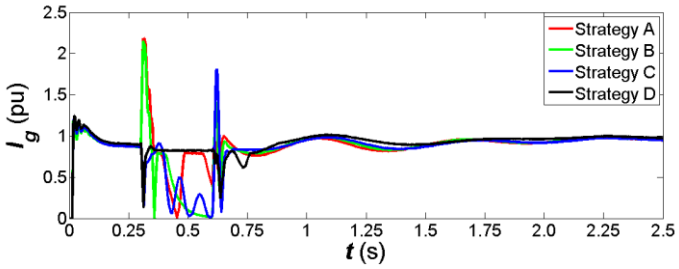

(b)

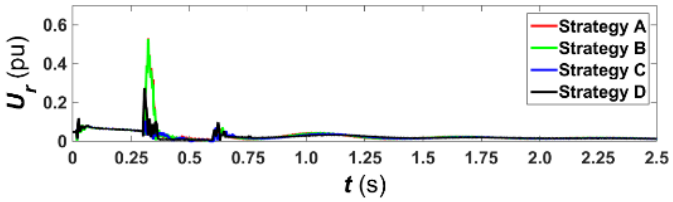

(c)

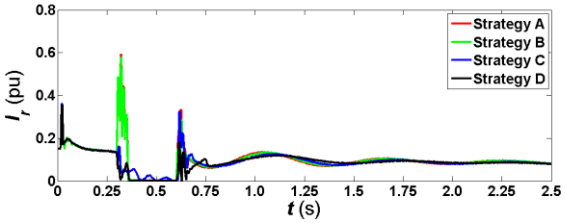

(d)

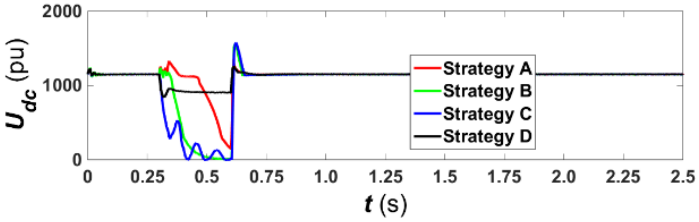

(e)

Figure 4.9. Grid-interfaced DFIG-WT response during symmetrical fault with voltage dip 85% and wind speed is 11m/s (a) Variation of grid voltage, (b) Variation of grid current, (c) Variation of rotor voltage, (d) Variation of rotor current, (e) Variation of DC link voltage, (f) Variation of elecromagnetic torque, (g) Variation of roror speed, (h) Variation of active power support at PCC, and (i) Variation of reactive power exchanged with grid at PCC (continued)

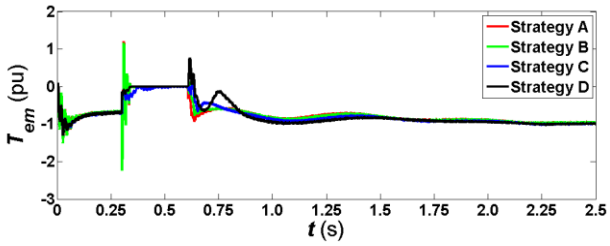

(f)

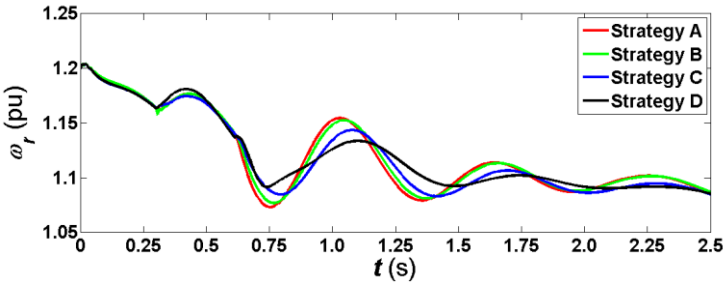

(g)

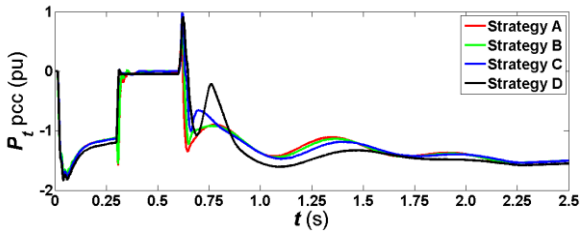

(h)

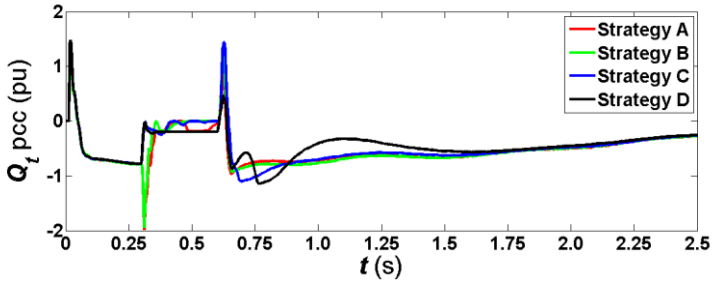

(i)

Figure 4.9. Grid-interfaced DFIG-WT response during symmetrical fault with voltage dip 85% and wind speed is 11m/s (a) Variation of grid voltage, (b) Variation of grid current, (c) Variation of rotor voltage, (d) Variation of rotor current, (e) Variation of DC link voltage, (f) Variation of elecromagnetic torque, (g) Variation of roror speed, (h) Variation of active power support at PCC, and (i) Variation of reactive power exchanged with grid at PCC (continued)

4.4.2. Asymmetrical Anlaysis

4.4.2.1. Single-Phase to Ground Fault Positive Sequence

Figure 4.10(a) describe U_g response during (Φ-g) fault at GCP. Strategies A and B starts producing low frequency oscillations during fault, violating grid-code requirements. Strategies C and D illustrate 71.5% voltage dip with fast settling time and smallest steady-state error. DFIG-WT is more sensitive to asymmetrical grid faults that induce voltage and current transient EMF in rotor circuitry. Strategies A and B generate maximum transients in U_r , while Strategy C produces constant high frequency oscillations of low magnitude during fault, as shown in Figure 4.10(b). Strategy D also induces transients but of low frequency and severity, compared to Strategies A, B, and C. The behavior of rotor current I_r transients is same in all Strategies during fault initiation and clearance, as shown in Figure 4.10(c). However, response of the aforesaid Strategies is quite different during fault. Strategies A and B results in high peak swings (0.26pu) above rated value (0.1pu), while Strategy C exhibits constant high frequency oscillations of 0.05pu magnitude. Due to RSC controllability in case of Strategy D that produces low frequency oscillations swinging between 0.004pu and 0.05pu. This response is in accordance with grid-codes and twice below the rated value of 0.1pu during fault.

Figure 4.10(d) illustrates U_{dc} response of Strategies A and B generating very high transients (90% above the rated value) that will destroy the sensitive power electronic devices, such as DC link capacitor. Strategies C and D remains within the specified limit of ratings with effective damped fluctuations and better FRT operation. Over speed of rotor is more obvious in Strategy D due to additional transformation of KE into WT, as shown in Figure 4.10(e). Strategies A, B, and C generate lower rotor speed during grid faults at GCP. This clarifies that damping of oscillations in case of Strategy D will be more, compared to Strategies A, B, and C.

Figure 4.10(f) and Figure 4.10(g) describe effectiveness of Strategy D supplying 0.1pu P_g and 0.04pu Q_g to the grid at PCC, while Strategy C shows a lower values of power support. Moreover, Strategies A and B shows power imbalance, abrupt response, oscillations, and absorbing reactive power from grid during fault. Strategies A, B, and C generate lower rotor speed during grid faults at GCP. This response is in accordance with the desired grid-code requirements of the national code.

4.4.2.2. Single-Phase to Ground Fault Negative Sequence

The negative-sequence performance of above mentioned Strategies is analyzed in terms of rotor voltage and rotor current, as depicted in Figure 4.10(h) and Figure 4.10(i). The response is better for Strategy D and Strategy C but worse for Strategies A and B, as RSC is disconnected during the fault interval.

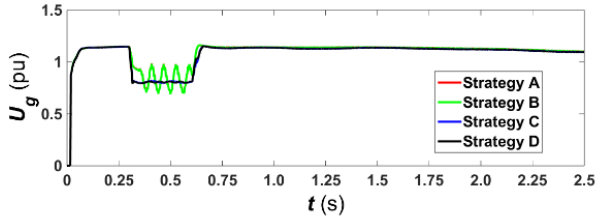

(a)

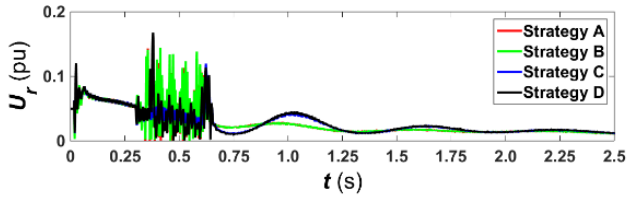

(b)

Figure 4.10 Grid-interfaced DFIG-WT response during asymmetrical fault with voltage dip 71.5% and wind speed is 11m/s (a) Variation of grid voltage, (b) Variation of rotor voltage, (c) Variation of rotor current, (d) Variation of DC link voltage, (e) Variation of roror speed, (f) Variation of grid active power support at PCC (g) Variation of reactive power exchanged with grid at PCC, (h) Variation of negative-sequence rotor voltage, and (i) Variation of negative-sequence rotor current

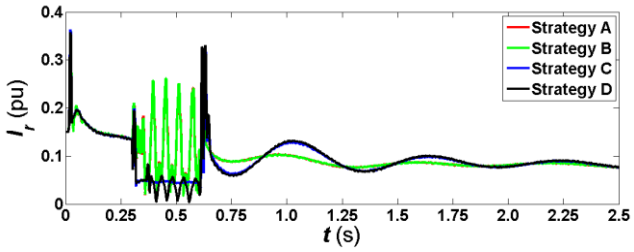

(c)

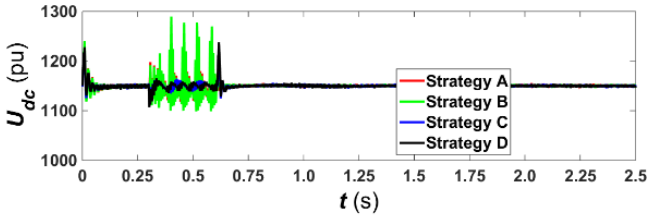

(d)

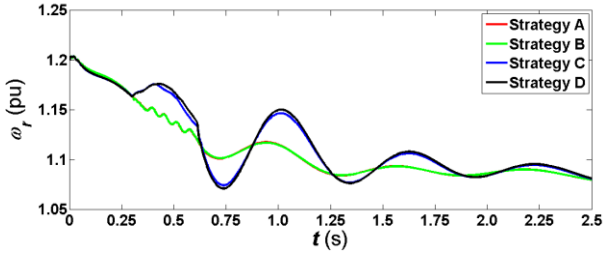

(e)

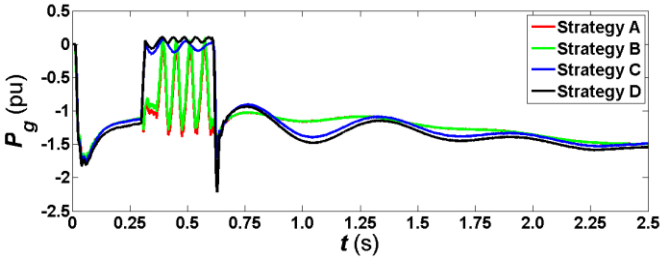

(f)

Figure 4.10 Grid-interfaced DFIG-WT response during asymmetrical fault with voltage dip 71.5% and wind speed is 11m/s (a) Variation of grid voltage, (b) Variation of rotor voltage, (c) Variation of rotor current, (d) Variation of DC link voltage, (e) Variation of roror speed, (f) Variation of grid active power support at PCC (g) Variation of reactive power exchanged with grid at PCC, (h) Variation of negative-sequence rotor voltage, and (i) Variation of negative-sequence rotor current (continued)

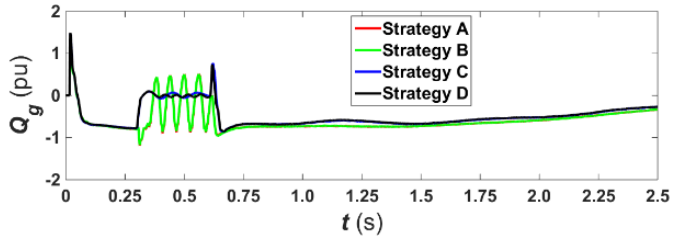

(g)

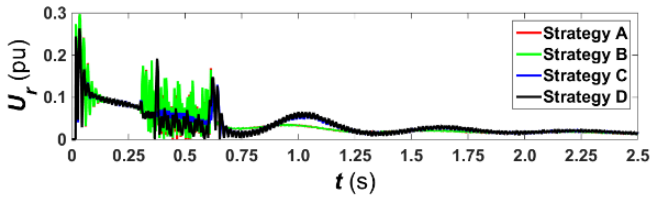

(h)

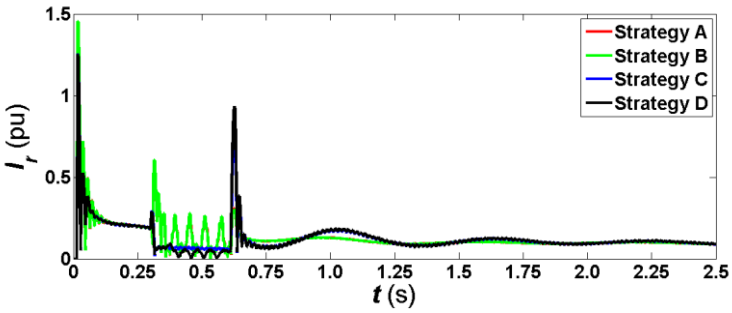

(i)

Figure 4.10 Grid-interfaced DFIG-WT response during asymmetrical fault with voltage dip 71.5% and wind speed is 11m/s (a) Variation of grid voltage, (b) Variation of rotor voltage, (c) Variation of rotor current, (d) Variation of DC link voltage, (e) Variation of roror speed, (f) Variation of grid active power support at PCC (g) Variation of reactive power exchanged with grid at PCC, (h) Variation of negative-sequence rotor voltage, and (i) Variation of negative-sequence rotor current (continued)

4.4.2.3. Double-Phase to Ground Fault Positive Sequence

All the Strategies fulfilled grid voltage U_g grid-code requirements during 2Φ-g at GCP. The voltage drop in U_g is more for Strategies A and B (64.4%), while Strategy C and Strategy D possesses a voltage dip of 62%, as presented in Figure 4.11(a). Figure 4.11(b) shows extreme

maximum induced U_r transients for Strategies A and B with peak values 0.6pu and 0.55pu (27.5 times the rated value) during fault initiation. Moreover, Strategies A and B produces high fluctuations of 0.11pu during fault interval, while Strategy C generates oscillations of 0.06pu. Furthermore, Strategy C shows high frequency rotor transients three times more than a rated value (0.02pu). Strategy D shows a robust performance for aforesaid case, resulting in low frequency oscillations of 0.01 pu. For I_r, Strategies A, B, and C performs worse, Strategy D produces induced current of 0.0018pu below the rated value (0.1pu), as seen in Figure 4.11(c). Strategy D exhibits a smooth U_{dc} response during fault with variation of 12.3% of rated value in accordance with FRT requirements, as shown in Figure 4.11(d). Strategies A, B, and C violates FRT grid-codes for DC link voltage. Figure 4.11(e) describe that rotor speed increases the most (within grid-code limits) during FRT for Strategy D, compared to Strategies A, B, and C. 0.04pu of P_g is delivered by DFIG-WT during fault to the grid, while A and C absorbs the power from grid. Strategy B delivers 0.08pu of active power to grid with transients at fault initiation, as presented in Figure 4.11(f). Strategy D provides 0.01pu reactive power support to the grid, while Strategies A, B, and C absorbs from the grid, as illustrated in Figure 4.11(g).

4.4.2.4. Double-Phase to Ground Fault Negative Sequence

Figure 4.11(h) presents negative-sequence rotor voltage on the performance of DFIG-WT. The abovementioned Strategies do not fulfill grid-codes, oscillations of U_r are high than rated value during fault interval. This abrupt response is very high for Strategies A and B and Strategies C and D also produces oscillations exceeding twice the rated value. Moreover, controllability of DFIG is lost during aforesaid scenario and RSC has no counteraction against negative-sequence transient EMF [4.10]. Furthermore, these negative-sequence transient EMF are consumed by rotor impedance.

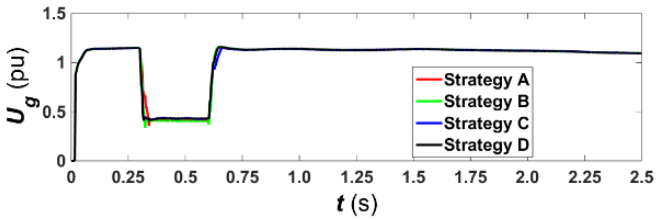

(a)

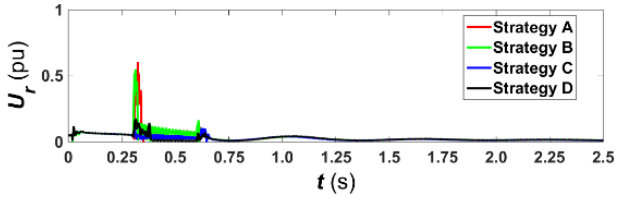

(b)

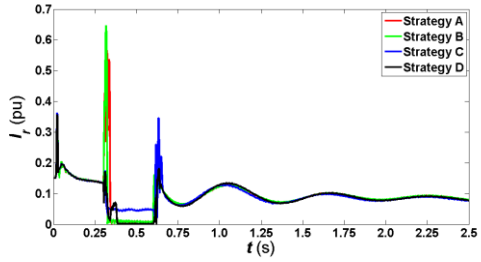

(c)

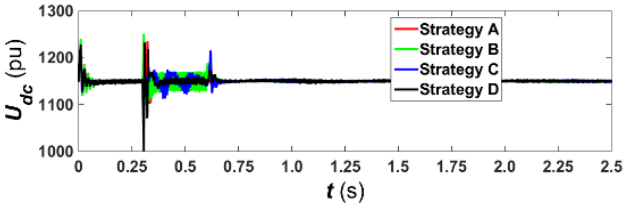

(d)

Figure 4.11. Grid-interfaced DFIG-WT response during asymmetrical fault with voltage dip 64.4% and wind speed is 11m/s (a) Variation of grid voltage, (b) Variation of rotor voltage, (c) Variation of rotor current, (d) Variation of DC link voltage, (e) Variation of roror speed, (f) Variation of grid active power (g) Variation of reactive power exchanged with grid at PCC, (h) Variation of negative-sequence rotor voltage, and (i) Variation of negative-sequence rotor current

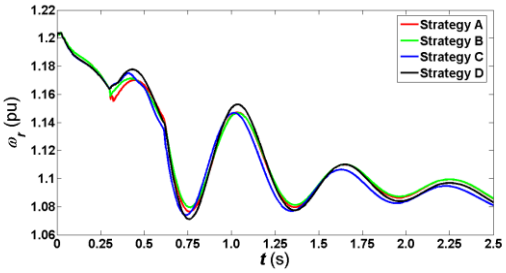

(e)

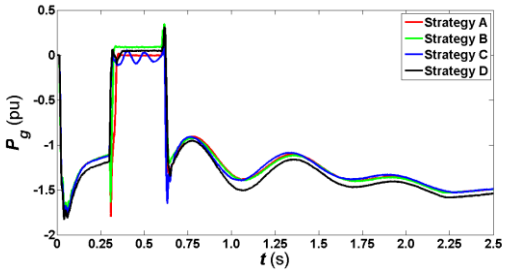

(f)

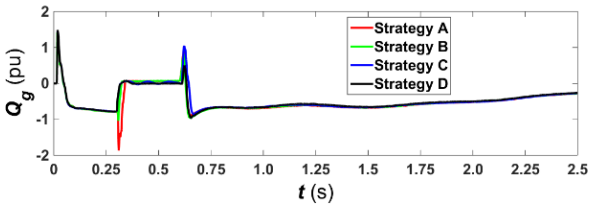

(g)

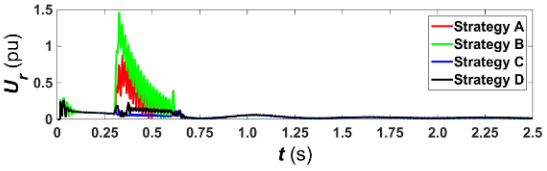

(h)

Figure 4.11. Grid-interfaced DFIG-WT response during asymmetrical fault with voltage dip 64.4% and wind speed is 11m/s (a) Variation of grid voltage, (b) Variation of rotor voltage, (c) Variation of rotor current, (d) Variation of DC link voltage, (e) Variation of roror speed, (f) Variation of grid active power (g) Variation of reactive power exchanged with grid at PCC, (h) Variation of negative-sequence rotor voltage, and (i) Variation of negative-sequence rotor current (continued)

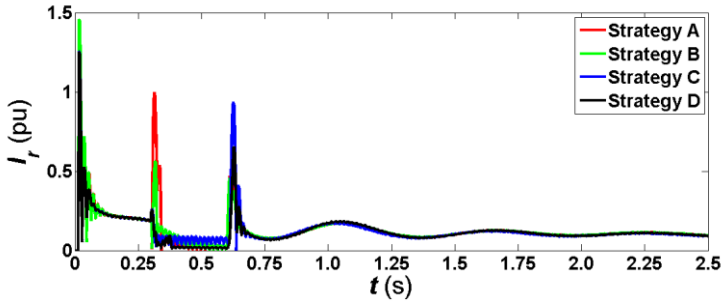

(i)

Figure 4.11. Grid-interfaced DFIG-WT response during asymmetrical fault with voltage dip 64.4% and wind speed is 11m/s (a) Variation of grid voltage, (b) Variation of rotor voltage, (c) Variation of rotor current, (d) Variation of DC link voltage, (e) Variation of roror speed, (f) Variation of grid active power (g) Variation of reactive power exchanged with grid at PCC, (h) Variation of negative-sequence rotor voltage, and (i) Variation of negative-sequence rotor current (continued)

4.4.2.5. Double-Phase Fault Positive Sequence

In Figure 4.12(a), Strategy C and D shows a voltage drop of 45.41% in U_g and Strategies A and B presents a voltage dip of 57.36%. 2Φ fault is most harmful for FRT operation [4.10] and Strategy D performs a robust operation during this interval, while Strategies A, B, and C produces abrupt EMF fluctuations in rotor voltage U_r and this effect of U_r is presented in Figure 4.12(b). Similarly, I_r response clarify the difference between aforementioned Strategies, as shown in Figure 4.12(c). Strategy D shows a smooth response during fault interval, while Strategies A, B, and C produces transients during fault initiation and clearance. Strategy D fulfills the most U_{dc} response in Figure 4.12(d) and output ω_r in Figure 4.12(e) satisfying grid-code specifications. Figure 4.12(f) shows Strategy D supplies 0.05pu P_g to grid and Strategy B provides 0.08pu P_g to grid. Moreover, Strategies A and B absorbs active power from grid violating FRT requirements. Strategy D provides maximum Q_g 0.05pu support at PCC, as illustrated in Figure 4.12(g). Furthermore, Strategy C provides least reactive support, while Strategies A and B absorbs power from grid.

4.4.2.6. Double-Phase Fault Negative Sequence

Figure 4.12(h) shows that all Strategies violates FRT specifications of RSC control, while Strategy D violation is minimum than the rest of the Strategies. Strategy D performs controlled response in case of, as depicted in Figure 4.12(i). Moreover, Strategies A, B, and C do not comply the standardized specifications for optimum FRT.

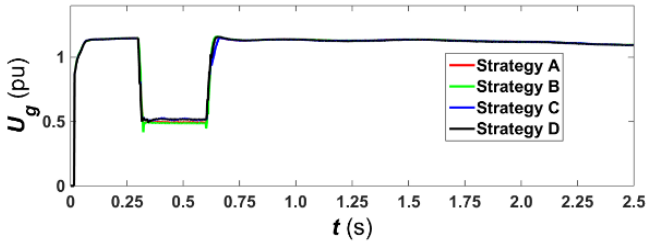

(a)

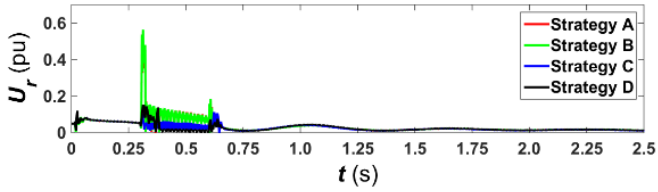

(b)

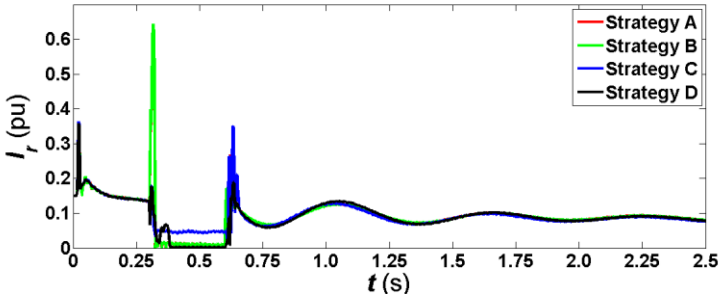

(c)

Figure 4.12. Grid-interfaced DFIG-WT response during asymmetrical fault with voltage dip 45.41% and wind speed is 11m/s (a) Variation of grid voltage, (b) Variation of rotor voltage, (c) Variation of rotor current, (d) Variation of DC link voltage, (e) Variation of roror speed, (f) Variation of grid active power, (g) Variation of reactive power from GSC, (h) Variation of negative-sequence rotor voltage, and (i) Variation of negative-sequence rotor current

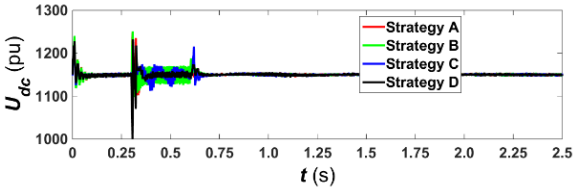

(d)

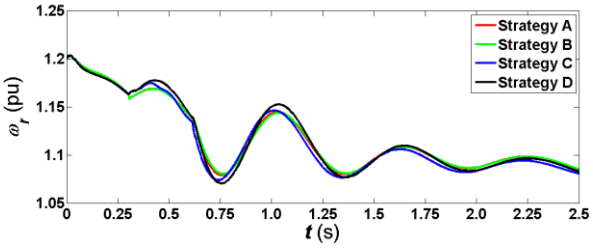

(e)

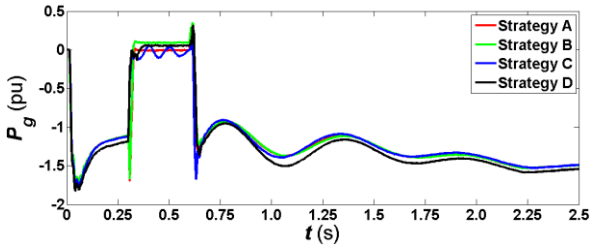

(f)

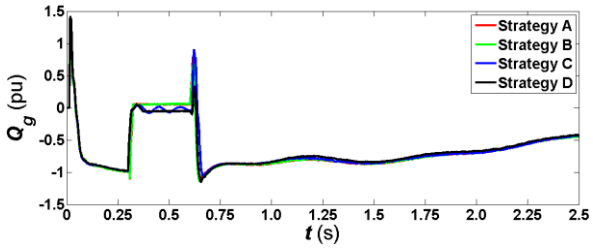

(g)

Figure 4.12. Grid-interfaced DFIG-WT response during asymmetrical fault with voltage dip 45.41% and wind speed is 11m/s (a) Variation of grid voltage, (b) Variation of rotor voltage, (c) Variation of rotor current, (d) Variation of DC link voltage, (e) Variation of roror speed, (f) Variation of grid active power, (g) Variation of reactive power from GSC, (h) Variation of negative-sequence rotor voltage, and (i) Variation of negative-sequence rotor current (continued)

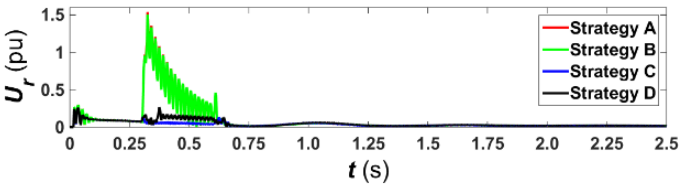

(h)

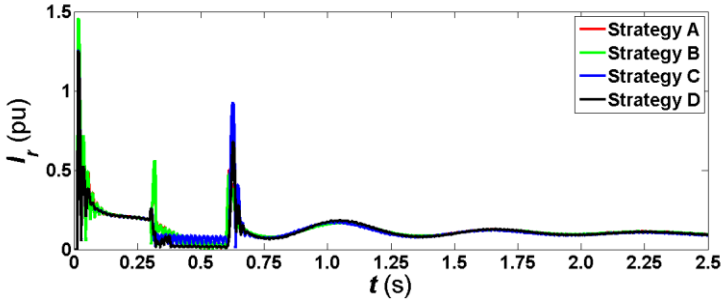

(i)

Figure 4.12. Grid-interfaced DFIG-WT response during asymmetrical fault with voltage dip 45.41% and wind speed is 11m/s (a) Variation of grid voltage, (b) Variation of rotor voltage, (c) Variation of rotor current, (d) Variation of DC link voltage, (e) Variation of roror speed, (f) Variation of grid active power, (g) Variation of reactive power from GSC, (h) Variation of negative-sequence rotor voltage, and (i) Variation of negative-sequence rotor current (continued)

From above analysis, we conclude that if the fault occur near GCP, non-ride through zones will be created. Controllability of positive-sequence components is higher for RSC, compared to negative-sequence quantities. In case of negative-sequence rotor variables, controllability with Strategy D is slightly higher than Strategies A, B, and C. This controllability factor may be increased by increasing the power ratings of the converter. Moreover, negative sequence quantities require separate control mechanism and ride-through specifications, compared to positive-sequence quantities. Furthermore, this critical difference exists for symmetrical faults as well. In case of negative-sequence rotor variables, controllability with Strategy D is slightly higher than Strategies A, B, and C.

4.5. References

[4.1] B. Ambati, P. Kanjiya, and V. Khadkikar, "A Low Component Count Series Voltage Compensation Scheme for DFIG WTs to Enhance Fault Ride-Through Capability," *IEEE Trans. on Energy Conversion*, vol. PP, no. 99, pp.1-10.

[4.2] F. Lima, A. Luna, P. Rodriguez, E. Watanabe, and F. Blaabjerg, "Rotor Voltage Dynamics in the Doubly Fed Induction Generator During Grid Faults," *IEEE Trans. on Power Electronics*, vol. 25, no. 1, pp. 118-130, Jan. 2010.

[4.3] D. Nguyen, and G. Fujita, "Optimal power control of DFIG wind turbines using a simplified power converter," in *Proc. IEEE T&D Conference and Exposition*, 14-17 April 2014, pp. 1-5.

[4.4] M. Rahimi, and M. Parniani, "Efficient control scheme of wind turbines with doubly fed induction generators for low-voltage ride-through capability enhancement," *IET Renewable Power Generation*, vol. 4, no. 3, pp. 242-252, May 2010.

[4.5] Y. Chongjarearn, "New method of setting the maximum crowbar resistance for doubly-fed induction generators under grid faults," in *Proc. IEEE Electrical Engineering/Electronics, Computer, Telecommunications and Information Technology (ECTI-CON)*, 14-17 May 2014, pp. 1-6.

[4.6] K. Okedu, S. Muyeen, R. Takahashi, and J. Tamura, "Wind Farms Fault Ride Through Using DFIG With New Protection Scheme," *IEEE Trans. on Sustainable Energy*, vol. 3, no. 2, pp. 242-254, April 2012.

[4.7] G. Pannell, D. Atkinson, and B. Zahawi, "Minimum-Threshold Crowbar for a Fault-Ride-Through Grid-Code-Compliant DFIG Wind Turbine," *IEEE Trans. on Energy Conversion*, vol. 25, no. 3, pp. 750-759, Sept. 2010.

[4.8] I. Ngamroo, and T. Karaipoom, “Cooperative Control of SFCL and SMES for Enhancing Fault Ride Through Capability and Smoothing Power Fluctuation of DFIG Wind Farm,” *IEEE Trans. on Applied Superconductivity*, vol. 24, no. 5, pp. 1-4, Oct. 2014.

[4.9] J. da Costa, H. Pinheiro, T. Degner, and G. Arnold, “Robust Controller for DFIGs of Grid-Connected Wind Turbines,” *IEEE Trans. on Industrial Electronics*, vol. 58, no. 9, pp. 4023-4038, Sept. 2011.

[4.10] M. Benbouzid, B. Beltran, Y. Amirat, Gang Yao, Jingang Han, and H. Mangel, “High-Order Sliding Mode control for DFIG-based Wind Turbine Fault Ride-Through,” in *Proc. IEEE Industrial Electronics Society IECON*, 10-13 Nov. 2013, pp. 7670-7674.

5. AN ANCILLARY SERVICES MODEL FOR THE DATA CENTERS AND POWER SYSTEM

This paper is submitted to the journal: *IEEE Transactions on Parallel and Distributed Computing*. The authors of this paper are Sahibzada Muhammad Ali, Muhammad Jawad, M. U. S. Khan, K. Bilal, Jacob Glower, Scott. C. Smith, Samee U. Khan, K. Li, A. Y. Zomaya.

5.1. Overview

Energy crises pose some of the key problems faced by the world today. Power hungry data centers make the problem even worse for power systems. For example, one of Google's data centers consumes more than 260 MW of power, which is more than the power consumed by the entire Salt Lake City [5.1]. The growing usage of World Wide Web and cloud computing services increases the power consumption and operating costs of data centers [5.2]. The increase in power consumption of data centers has a significant influence on the operation of the power system [5.2]. However, due to the large network size, power systems need data centers for intensive computational requirements [5.3]. The computational services provided by the data center for stable and reliable operation of the power system are known as ancillary services [5.3]. The key ancillary services required by the power system are optimal power flow on all Transmission Lines (TLs), voltage stability, power loss reduction, and identification of endangered TLs and buses. In a conventional power system, the lack of fast and intelligent control results in contingencies in some power system sections. The resultant contingencies lead to Transmission Line Failures (TLFs), un-optimized power flow, degradation in Quality of Service (QoS), electrical equipment failure, and complete blackouts [5.4]. The parallel computing capability of the data center can meet the computational requirements of the power

system jobs, which can return the power system back to steady-state operation in a manageable time.

5.1.1. Motivation

The power system's revenue is highly dependent on reliability and steady state performance [5.5]. Unreliable power systems that lack in QoS result in revenue loss. Moreover, the economic factors of power systems, such as demand-supply management, operational cost, standby generating unit, and salaries of the utility crew get disturbed. Furthermore, degradation in QoS will prevent the electrical network from further expansion. Therefore, data centers should provide ancillary services on a priority basis because the delay in power system jobs can lead to revenue loss for power system companies.

The data center and power system are part of a bigger cloud environment [5.1]. Most of the time, in cloud, data center resources remain idle during normal operations. Therefore, the data center's scheduler does not require reshuffling or delaying cloud computing jobs to execute a power system's ancillary services. However, at certain times, a data center may be over-loaded [5.6]. In such scenarios, the data center must preempt cloud computing jobs to satisfy the priorities of the power system jobs [5.6]. The power system jobs should not over burden the data center or violate the Service Level Agreement (SLA) of cloud computing jobs. Therefore, the data centers need an efficient job scheduling technique that minimally affects cloud computing jobs, while executing ancillary services.

This paper presents an Ancillary Services Model (ASM) that maximizes the revenue of the data center while ensuring the reliability and stability of the power system. We believe that our research contribution is more versatile and covers a broader area in the field of smart power

systems using the ASM compared to prior works. The proposed ASM for data centers and power systems consists of the following:

In summary, our contributions in this chapter are as follows: (1) we evaluated Longest Job First (LJF), Shortest Job First (SJF), and Shortest Remaining Job First (SRTF) to determine that SRTF is the best job scheduling technique in case of average queue time and makespan of data center workload, while SJF performs better in terms of data center workload preemption and power system job preemption. Our evaluation is based on power consumption, makespan, number of preempted jobs, queue time, and resource utilization, (2) we proposed three main ancillary services for stable operation of the power system, namely: (a) Optimal Power Flow (OPF), (b) Transmission Line Importance Index, and (c) Bus Importance Index. We performed our experiments on standard IEEE bus systems, and found the convergence condition for the OPF solution. Moreover, we identified endangered TLs and Buses, when two or more TLs are out, (3) we defined a SLA for priority execution of ancillary services on data centers. The SLA elaborates the revenue generation and penalty on the data center, if the ancillary services are delayed. The SLA is tested for variable load of the data center, variable energy price, and variable job length given by the power system during a month's time, and (4) The ASM is based on the optimal job scheduling technique for data centers, ancillary services for the power system, and SLA. The ASM reduces the revenue loss of the power system during contingencies with minimum effect on the data center.

The rest of the chapter is organized as follows. Section 5.2 demonstrates the system model. In Section 5.3 presents ancillary service model for the power system, Section 5.4 describe service level agreement, Section 5.5 discusses the revenue modeling, Section 5.6 shows simulation settings, and Section 5.7 presents ASM convergence.

5.2. System Model

In this section, we define a system model named ASM and notations for both data center and power system. We use these notations and system model to define a SLA and revenue model. The high level architecture of the system model is shown in Fig. 1. The data center has M_{max} servers that compute internet services and cloud workload. In return, the data center demands a service cost from customers. Moreover, the data center spends a large portion of its revenue on purchasing reliable and stable power from the power system. On the other hand, the power system revenue is highly dependent on demand-supply stability. The power system requires fast computing workstations for ancillary services to maintain reliability. Therefore, we divide our system model into two sub-parts: (a) data center module, (b) ancillary services for the power system.

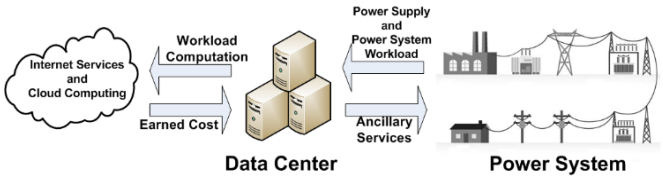

Figure 5.1. System architecture

5.2.1. Data Center Module

The purpose of data center module is to calculate the power consumption with and without the work-load of the power system jobs. Moreover, different job scheduling algorithms on the data center work-load are tested. The module provides an appropriate job scheduling technique that handles the power system jobs with minimal effect on the data center. The effect is calculated in terms of power consumption, makespan, number of job/task preemptions, and job queue time. The estimated revenue of the data center is highly dependent on electricity unit price and power consumption. Therefore, the discussion on electricity price and workload based power consumption is essential.

The electricity price model depends on the regulated or deregulated power market of the region [5.17]. In a regulated market, the electricity price remains uniform throughout the day. Conversely, in deregulated markets, the electricity price changes during the day depending on changes in the wholesale electricity market. The non-uniform pricing tariffs include time of use pricing, day ahead pricing, and real-time pricing. In the real world, the varying order of magnitude between demand and supply, and average pricing of electricity units make real-time pricing the most complex pricing tariff [5.17]. We used real-time pricing tariffs in the data center.

5.2.1.1. Power Consumption

The total power consumption of the data center is the sum of power consumption by computer servers, cooling plants, and lighting facilities, as given below [5.15].

$$\mathcal{P} = \mathfrak{M}[\mathcal{P}_I + (\Xi_U - 1)\mathcal{P}_P + (\mathcal{P}_{Peak} - \mathcal{P}_I)\mathfrak{U}] \,. \qquad (5.1)$$

In Eqn. (5.1), $\mathcal{P}_I$ denotes the power consumption of an idle server, and $\mathcal{P}_P$ is the average peak power when a server is busy handling requests. The term $\mathfrak{M} \leq \mathfrak{M}_{max}$ denotes the number of "on" servers, $\mathfrak{U}$ denotes CPU utilization in servers, and Ξ_U is the energy efficiency of the servers [5.11]. The power consumption of the data center varies throughout the day depending on workload. The detailed description of workload, power consumption, CPU utilization in servers, energy efficiency of servers, job scheduling techniques, queue time analysis, job preemption mechanism, and revenue calculation are discussed in Section 5.7.

5.3. Ancillary Services For The power System

Power systems are large and complex networks that constantly run at operational limits. Any transmission line failure can cause massive cascading failures [5.12]. Therefore, reliability of the power system depends on the ability to deliver the desired amount of electricity to all

delivery points within acceptable quality levels and at minimum cost. The aforementioned attributes need to be accomplished by finding an adequate balance between reliability and uncertainties of future conditions.

In our proposed model, the power system is modeled as a set of buses interconnected by TLs to form a network topology. The total number of buses defines the size of the power system. The loads and generators are connected to the buses that consume and inject power into the transmission net-work, respectively. The total load of the power system is the sum of background load (commercial and residential) and data center power load. The above network topology is suitable to solve for steady-state voltages and power flows [5.14]. The three main ancillary services provided by the data center to the power system include the following: Optimal Power Flow Analysis, Transmission Line Importance Index, and Bus Importance Index.

5.3.1. Optimal Power Flow Analysis

The primary objective in a balanced power system is to minimize generation cost. There are two main constraints in power balancing: (a) equality constraints (generation-load balance) and (b) inequality constraints (upper and lower limits on the output of generating units). In a power system, the generating units and loads are not connected to the same bus. Therefore, the economic dispatch will result in voltage instability within the power system. Moreover, an optimal solution is required that results in acceptable power flows on all transmission lines. The OPF is among the key parameters of power system that provides an optimal solution for the above mentioned problem, and has a cogent relationship with cascading failures [5.10].

In the OPF, the equality constraint is to balance complex power at each bus using power flow equations. The inequality constraints consist of TL flows and voltage limitations of control variables, including active power of generators, voltage of generating units, position of phase

shifters, status of reactors and switched capacitors, and disconnected loads. State variables are used to describe the system response due to the change in control variables. Voltage magnitude is defined at each bus except generator buses. Similarly, the voltage angle is defined for each bus except the slack bus. The main parameters for OPF calculation are the known system characteristics, system topology, and network parameters (generation limits and generation cost function) [5.2]. The main objective function is to minimize power generation cost, as stated in Eqn. (5.2):

$$\min_{u} \sum_{i=1}^{N} Co_i(P_i)\,. \tag{5.2}$$

Where Co_i is the cost of bus i, P_i is the active power of bus i, N is the total number of buses, and u is the vector of control variables. The other objective functions are: (a) minimizing following, and (b) minimizing the TLLs using the objective function O.

$$\min_{u} \sum_{i=1}^{N_u} Co_i\left|u_i - u_i^0\right|, \tag{5.3}$$

$$O = \sum\nolimits_{i=(k,j)} \left(G_k\left(V_i^2 + V_j^2 - 2V_iV_jcos\delta_{ij}\right)\forall k \in N_b\right). \tag{5.4}$$

In Eqn. (5.4), V_i is the voltage of bus i and V_j of bus j, G_k is the conductance of TL k, N_b is the number of TLs in the network, and δ_{ij} is the voltage angle difference between bus i and bus j. The power flow equations used for equality constraints are given below:

$$P_k^G - P_k^L = \sum_{i=1}^{N} V_kV_i[G_{ki}\cos(\theta_k - \theta_i) + B_{ki}\sin(\theta_k - \theta_i)], \tag{5.5}$$

$$Q_k^G - Q_k^L = \sum_{i=1}^{N} V_kV_i[G_{ki}\sin(\theta_k - \theta_i) + B_{ki}\cos(\theta_k - \theta_i)],$$

$$Compact\ Expression: G(x,u,y) = 0.$$

Where P_k^G is the active power of the generator, P_k^L is the active power of the load, Q_k^G is the reactive power of the generator, Q_k^L is the reactive power of the load, G_{ki} is the mutual conductance, B_{ki} is the mutual susceptance, and θ_k is the phasor angle. The state variables vector and parameter vectors are denoted by x and y, respectively. For inequality constraints, the limits on the control variables must be imposed as: $\underline{u} \le u \le \overline{u}$, the operating limits on power flows are $|P_{ij}| \le \overline{P_{ij}}$, the operating limits on voltages are $\underline{V_j} \le V_j \le \overline{V_j}$, and the compact expression of inequality constraints is written as $H(x,u,y) \ge 0$. The OPF problem is complex due to the non-linear behavior of all the components of the power system. The Newton-Raphson method is applied to solve the OPF, where the tolerance of the power injection and consumption mismatch is 10^{-8} [5.20]. If the tolerance is below 10^{-8}, the OPF solution is considered to be converged, as shown in Figure 5.2.

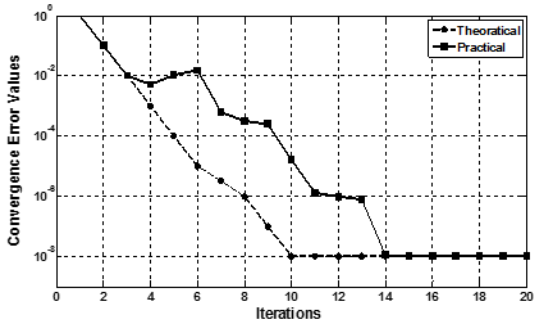

Figure 5.2. Convergence of Newton-Raphson tolerance between power injection and power consumption

Newton-Raphson is an iterative method that locally converges [5.15]. Theoretically, the cost function value indicated in Eqn. (5.5) should converge to the optimum solution. How close is enough? This question is problem dependent and most difficult to measure in practice [5.22]. However, decades of practice shows that Newton's method converges in a few iterations for most

problems. Therefore, the theory has practical importance, and our results in Section 5.7 support the theory. Eqn. (5.5) is a set of non-linear expressions that need to converge as $G(x,u,y) \cong 0$. Here $G: R^n \rightarrow R^n$. The Newton iteration expression is defined as:

$$G(x_k) = -J(x_k)\Delta x_k, \Delta x_k = x_{k+1} - x_k \,, \tag{5.6}$$

where x_k is the state variable for the k^{th} iteration, x_{k+1} is the state variable for the $(k+1)^{\text{th}}$ iteration, Δx_k is the error between two consecutive iterations, and $J(x_k)$ is the Jacobian matrix for x_k. If $G(x)$ is differentiable, then the Jacobian matrix is expressed as:

$$J(x_k) = G'(x_k) = \frac{\partial G}{\partial x}|_{x_k} \,. \tag{5.7}$$

Newton's method is convergent under the following three assumptions: **Assumption 1:** non-linear function $G(x)$ has solution x^*. **Assumption 2:** $G': \Omega \rightarrow R^{n\times n}$ is lipschtiz continuous near x^*. **Assumption 3:** $G'(x^*)$ is non-singular. Therefore, a constant, $K > 0$, exists such that: n is sufficiently large and mismatch tolerance decreases quadratically.

$$\|e_{n+1}\| \leq K\|e_n\|^2 \,, \tag{5.8}$$

The non-singularity of the Jacobian matrix is assured by *Assumption 3*, iteratively. Therefore, the initial point and Jacobian singularity play a vital role in the convergence of the OPF solution for the power system.

5.3.2. Transmission Importance Index

We evaluate the TL importance index for fault detection and cascading failure avoidance in the power system. When a TL failure occurs, the AC power flow on some other TLs will increase and cause volt-age instability. The TL importance index identifies those TLs whose failure can lead to a complete or partial blackout. If the AC power flow ratio on any TL increases above a certain threshold, then an outage will occur on the TL. The threshold depends on the maximum AC power flow a TL can sustain. Therefore, power system operators can take

precautionary measures before the occurrence of a failure. The judgment criteria for detecting whether a TL outage can cause system failure depends on two fac-tors: (a) the convergence of OPF solver and (b) power loss constraints on TLs. As explained in Section 5.2.1, the Newton-Raphson method is used to calculate the OPF solution [5.20]. If the Newton-Raphson method provides a converged OPF solution but unacceptable power loss on TLs, then the sys-tem will still be considered as un-converged for the sake of practical economic constraints. Therefore, both conditions are necessary and sufficient for an acceptable optimized OPF solution.

5.3.3. Bus Importance Index

The bus importance index is another important measure for the power system that depends on the concept of centrality. Centrality defines the most important or central bus in a network [5.3]. The most common and famous method is Eigenvector centrality that assigns the centrality value β to all of the isolated buses within a network [5.3]. Mathematically, the Eigenvector centrality of a network is defined as:

$$C_i = \alpha \sum_j A_{ij} \frac{C_j}{k_j^{out}} + \beta \, . \tag{5.9}$$

Where α is a damping factor that can have value$0 < \alpha < 1$, A_{ij} is the entry of the adjacency matrix, C_j in the centrality of bus j that is directly connected to bus i, k_j^{out} is the out degree of bus j, and β is the constant centrality value assigned to the isolated bus. The out degree describes how many buses are taking power from bus j. If there are buses in the power system that have an out degree equal to zero, then the first term in Eqn. (5.9) will be undefined. To avoid such condition, k_i^{out} is set to 1 for all such buses. The matrix notation of Eqn. (5.9) is represented as:

$$C = \alpha A D^{-1} C + \beta 1 \, . \tag{5.10}$$

Where '1' is the vector (1, 1, 1, ….) and D is the diagonal matrix with elements $D_{ii} = \max(k_j^{out}, 1)$. The power system depends on the calculation of OPF, whose solution defines whether the system is operating normally or the TLLs exceed the threshold. During an emergency, when outages occur on multiple TLs, the power system needs an optimized OPF solution. Moreover, the system requires identification of TLs that can cause a cascade outage and endanger buses due to over-voltage. The TL importance index identifies such TLs that are in danger of failure due to excess power flow. The bus importance index identifies power system buses that have excess voltage, which can trip relays on these buses.

5.4. Service Level Agreement

The core of the ASM is to define a SLA between the data center and the power system with minimum loss at both ends. The nature of the workload in data centers is stochastic and the execution time of each job varies [5.4]. Therefore, the following calculations are necessary for defining the SLA: (1) How much revenue loss is acceptable for the data center to prioritize execution of power system jobs? And How much uptime can the data center provide to the power system in a month's time.

In our proposed model, ancillary services for the power system are the highest priority jobs. If the data center is operating at its peak, then the scheduler must preempt other cloud computing jobs to execute an ancillary service request. There is no such mechanism known to the authors to determine how much delay a power system can withstand before power transmission gets perturbed. Excess delay in ancillary services also indirectly affects the data center's power supply. The ASM model will benefit the power system and the data center in a coordinated controlled manner.

Table 5.1. IEEE bus systems specifications

IEEE Bus Systems	TLs	GBs	Load Buses	GC (MW)	BL (MW)	OPF	Convergence Time on Single-Processor (seconds)
30	41	6	20	191.6	189.2	14	5.88
118	186	54	99	4374.9	4242	19	72.06
300	411	69	201	23935.4	23525.8	22	462.25
2383	2896	327	1826	25281	2458.4	34	980.20

Table 5.2. Peak power consumption of a typical server

Component	Peak Power (W)	Count	Total Power (W)
CPU	40	2	80
Memory	9	4	36
Disk	12	1	12
Motherboard	25	1	25
PCI Slots	25	2	50
Fan	10	1	10
Total-System Power			213

Table 5.3. Data center specification

Time Duration	20 February 2009 – 22 March 2009
Total data center jobs executed	22,385
Total distinct servers	1,056
Processor name	1056 Dell PowerEdge SC1425
Processor speed	3.0 GHz or 3.2 GHz
Peak performance	13 TFlop/second

Moreover, if ancillary services are delayed, then how much extra will power cost the data center? Furthermore, when a data center delays cloud computing jobs more than a certain time, data center revenue will be drastically affected. For example, if the Amazon Elastic Compute Cloud (EC2) delays a job by upto 1% of the total agreed upon execution time, then Amazon pays

a penalty (named service credit by amazon) of 10% of the agreed upon cost for the job. Moreover, if the delay is more than 1% of the agreed upon time, then the penalty is increased to 30% of the agreed amount [5.5].

We define a SLA that minimally affects the cost of the data center and maintains reliability of the power system. According to the SLA, the increased power consumption cost of the data center due to the execution of ancillary services will be paid by the power system. Moreover, a threshold will decide the number of cloud computing jobs that a data center can delay without penalty. We calculate this threshold in Section 5.7.

5.5. Revenue Modeling

The revenue model depends on the power consumption of the data center that is calculated by Eqn. (5.1) for any instant in time, where $\mathfrak{M}$ is the number of "on" servers in the data center. The revenue ($\mathfrak{R}$) of the data center is calculated as:

$$\mathfrak{R} = \sum_{i=1}^{T_J} \left(1 - q_i(\mu_i)\right) \left[1 + \frac{\mathfrak{F}_i}{\mathcal{L}_i}\right] - q_i(\mu_i) \left[1 + \frac{\mathfrak{F}_i}{\mathcal{L}_i}\right]. \tag{5.11}$$

The job service rate μ_i is defined as:

$$\mu_i = k\mathfrak{M}_i \,. \tag{5.12}$$

Let $\mathcal{T}$ be the time taken by a data center server to finish a job. In Eqn. (5.12), the variable k represents jobs per second ($1/\mathcal{T}$). In Eqn. (5.11), $q_i(\mu_i)$ is the probability of job failure, and T_J is the total number of jobs in the month. The data center's loss for preempting a cloud computing job and executing the i^{th} power system job is represented by $\mathcal{L}_i$. The data center will demand $\mathcal{L}_i$ dollars from the power system to minimize revenue loss. Moreover, $\mathfrak{F}_i$ is the monetary incentive that the data center can demand from the power system. In Eqn. (5.11), the term $\left(1 - q_i(\mu_i)\right) \left[1 + \frac{\mathfrak{F}_i}{\mathcal{L}_i}\right]$ denotes the total revenue earned by the data center for completing the

computational jobs of the power system in sufficient time. The term $q_i(\mu_i)\left[1+\frac{\mathfrak{F}_i}{\mathcal{L}_i}\right]$ is the penalty that the data center will pay for delaying power system jobs. Eqn. (5.11) minimizes the revenue loss of the data center and provides incentives to prioritize power system jobs.

Table 5.4. Power system job types and details

Power System Jobs Type	Execution Time (minutes)	Number of CPUs Utilized
Emergency	1-5	100-500
Reactive	1-10	50-300
Periodic	1-10	1-100

5.6. Simulation Settings

We consider IEEE 30 bus, IEEE 118 bus, IEEE 300 bus, and IEEE 2383 bus systems for the power system reliability tests. As the size of the power system increases, job lengths associated with the workload increase accordingly. The detailed descriptions of the IEEE bus systems are given in Table 5.1. To understand the network topology of IEEE bus systems, an IEEE 30 bus system is shown in Figure 5.2. The data center is powered from bus number 30 in the IEEE 30 bus system. Our exemplary data center consumes on average 1.885 MW of power operating at peak-load during a day with 1,056 servers running. A typical data center server has $\mathcal{P}_P$ = 213 watts and $\mathcal{P}_I$ = 100 watts, as shown in Table 5.2.

The TL outages are taken as an emergency condition for the power system, requiring ancillary services from the data center. TLs outages are modeled as a "two state Markov" model on each TL. A Markov state of the power system is defined by a particular condition where every TL is in a given state of its own. All possible states of the TLs make up the state space. The TL state (Up/Down) is considered to be a continuous random variable. In our study, the distributions for up and down states of the TLs are taken as exponential. The exponential distribution has the following probability distribution defined as:

$$F(x) = 1 - e^{-\rho x} = z\ . \tag{5.13}$$

In Eqn. (5.13), the mean of random variable X is denoted by ρ^{-1}. We set the exponential function given in Eqn. (5.13) equal to a uniform random decimal number, z, with values between 0 and 1. Equation (13) is then rewritten as:

$$x = -\frac{\ln(z)}{\rho}. \tag{5.14}$$

The occurrence time of TL failures and their maintenance time duration is determined by Eqn. (5.14). Moreover, in the real-world the nature of the load is random and precise load forecasting is challenging. Therefore, the background load distribution on power system buses is also modeled as a random variable with normal distribution. For example, the mean value of active power on all load buses in the IEEE 30 bus system is 9.46 MW (nominal).

We use a real-world data center workload, collected from Computational Research of State University of New York at Buffalo to validate the ASM [5.6]. The workload is a collection of a 30 day time span taken during February 20, 2009 to March 22, 2009. The unit electricity price offered to the data center is taken from the New York Independent System Operator (NYISO) for the same period February 20, 2009 to March 22, 2009 [5.14]. The complete data center specification is given in Table 5.3. The workload distribution sometimes exceeds 100% for a day, as shown in Figure 5.4. Therefore, data center resources are inadequate to complete all jobs at these particular times.

For clarity, ancillary services for the power system that will execute on data centers are called “power system jobs”. Moreover, we represent all other cloud computing jobs as the “data center workload”. We model three categories of power system jobs in our simulations along with the data center workload. The highest priority jobs are emergency jobs that arrive when a failure occurs in the power system. The data center will allocate the maximum required resources for the

completion of these jobs in least amount of time. The second highest priority jobs are called reactive jobs, which occur when there is a sudden large drift in the load. The data center will allocate a large number of resources to complete reactive jobs in a reasonable time with minimum effect on the data center workload. All of the remaining power system jobs required for normal operation are called periodic jobs, which will execute periodically on the data center. These periodic jobs also require significant resources, but delay is acceptable. A detailed description of power system jobs is given in Table 5.4.

We include “five” emergency jobs, 30 reactive jobs, and 2,930 periodic jobs in our dataset. Emergency power system scenarios rarely occurs in a month’s time. Therefore, we only include “five” emergency jobs in our simulations scenario. Reactive jobs occur more often than emergency jobs. Therefore, we include one job per day at a random time in the workload. Regular jobs required for stable power system operation are executed periodically every 15 minutes. Power system jobs can vary from a few minutes to a couple of hours, depending on the number of TL outages and network size. For testing and validation of the ASM, the power system job timing (e.g., OPF convergence time) varies from one minute to twenty minutes [5.7]. End user power consumption is always variable over time, and this phenomenon is also considered in the simulations. Table 5.4 also includes execution time and CPU utilization for the various power system jobs. In contrast, time-sharing algorithms divide time on a processor into several slots and assign the slots to every unique job. In our work, due to the priority of power system jobs, we choose space-sharing scheduling algorithms for the data center. The three space-sharing job scheduling techniques used are: (a) Longest Job First (LJF), (b) Shortest Job First (SJF), and (c) Shortest Remaining Time First (SRTF).

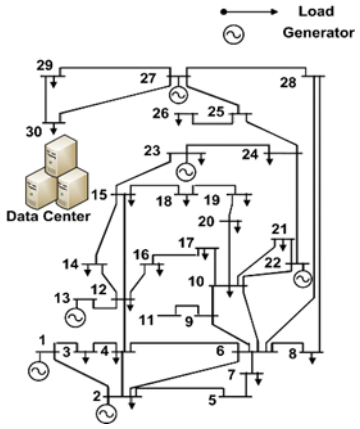

Figure 5.3. Network topology of the IEEE 30 bus system for reliability testing, where the data center is acting as a load

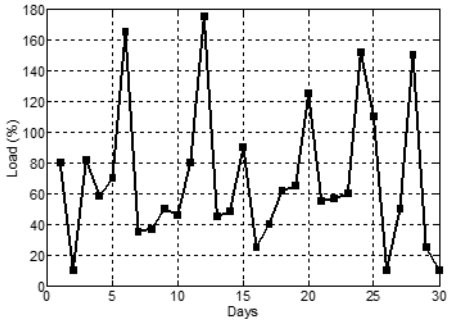

Figure 5.4. Total data center load per day over a month duration

Substantial research in the field of parallel and distributed computing has introduced several job scheduling algorithms, categorized as two mainly types: (a) time-sharing and (b) space-sharing. Space-sharing algorithms allocate resources to a single job until the job executes completely. The LJF space-sharing scheduling algorithm allocates resources to the longest job first. LJF is known to maximize server utilization. Similar to LJF, SJF periodically sorts incoming jobs and executes the shortest job first. SJF tends to minimize turn-around time. SRTF is the preemptive form of SJF. In SRTF, the job with the smallest remaining time will be executed first till completion unless a new job is added that requires less execution time than the remaining time of the current job. The above job scheduling algorithms are used to execute power system jobs along with the data center workload. The priority of all power system jobs are

set to be higher than the data center workload, such that inclusion of power system jobs can delay the data center workload. In our simulation settings, the job delaying criteria for all scheduling techniques is to preempt the job that has the longest remaining time. Whenever there are two or more jobs with the same time remaining and one of these job must be preempted, the first job in the queue will be selected first for preemption. The reason for comparing job scheduling techniques is to find an optimal job scheduling technique that has the minimum effect on number of preempted jobs, makespan, and average queue time. Moreover, an optimal job scheduling technique will also reduce idle power consumption and improve data center resource utilization. Conversely, a scheduling technique that results in a large number of preempted jobs and long duration of jobs in queues will adversely affect the SLA. Similarly, a scheduling technique that create a large makespan for the data center workload will result in increased power consumption.

In the ASM, the monetary cost to execute job is based on the "on-demand pricing criteria" of Amazon [5.25]. For example, a job utilizing 8 CPUs will bear a cost of $0.840/hour [5.25]. Moreover, the job preemption penalty is also the same as the service credit rate of Amazon EC2 [5.25].

5.7. Results and Discussions

We have carried out simulations of our proposed ASM on a 96 core super server SYS-7047GR-TRF system. The data center provides in-time OPF solutions and identification of endangered TLs and buses for establishing a robust power system. However, due to the effect of power system jobs, power consumption of the data center increases. This increase in power consumption has various reasons that are described later in the Section. The ASM is simulated for the period of one month using three job scheduling techniques, as stated in Section 5.6.

Figure 5.5(a), Figure 5.5(b), and Figure 5.5(c) show the average power consumption of the data center averaged over 20 runs for a 24-hours period, under the influence of the LJF, SJF, and SRTF job scheduling technique, respectively. The aforesaid figures elaborate that the power consumption of the data center increases after the inclusion of power system jobs.

However, we can observe from the figures that in the beginning and end hours of the day, the average power with the added power system jobs is less than the average power without power system jobs, which is counter intuitive. Since Figure 5.5 reports the average power consumption graphs over a month's time, and the inclusion of power system jobs increases the makespan of the overall workload of the data center, the total hours of work increases, which reduces the average power consumption with power system jobs in the beginning and end hours of the day, but still yields a net overall increase in average power consumption per day of 0.05527%, 0.05754%, and 0.06342%, using SRTF, SJF, and LJF, respectively. Figure 5.5(d) shows this power consumption comparison graphically for all three job scheduling techniques. The graph trend shows that most of the time power consumption remains the same; however, during the peak load period (starts from late afternoon till midnight), the SRTF performs better than LJF and SJF. To calculate the obvious increase in power consumption cost, a real-world electricity unit price is used, as shown in Figure 5.6 [5.17].

This subsection describes the impact of executing power system jobs on the data center. The influence is observed on the number of preempted jobs, makespan of jobs, average queue time, and resource utilization. Job preemption involves the purging of the data center workload in favor of power system jobs. Figure 5.7 shows the number of preempted tasks in one month's time. A job in the data center workload can have more than one task depending on the number of CPUs utilized by the job. In the data center, task preemption affects job execution time, which

may result in a monetary penalty, per the SLA. The more preempted tasks, the more the data center will be penalized for delaying jobs. In Figure 5.7, we observe that SJF preempts fewer tasks compared to SRTF and LJF. We also observe the job that was preempted the most number of times, as shown in Figure 5.8. Moreover, the job that is preempted the most times is also the longest running job in our data center workload. Furthermore, when the SJF job scheduling technique is used, this job is preempted fewer times compared to SRTF and LJF.

Although, the priority of power system jobs is higher than the data center workload, the job preemption effect of the different scheduling algorithms is still noticeable on the power system jobs, as shown in Figure 5.9, which illustrates that SJF and SRTF preempt fewer power system jobs compared to LJF over a month's time. SJF and SRTF preempt less than 0.1% of power system jobs; whereas LJF preempts four times the number of power system jobs, 0.4%. As shown in Figure 5.10, we also identify the effect of preemption on the longest running periodic job of the power system, illustrating that SRTF results in more preemptions compared to SJF and LJF.

Job queue time is another important metric that directly affects data center performance. The longer the queue time, the longer overall execution time for jobs will be; and data center power consumption is directly related to job execution time. Figure 5.11 shows that average queue time using SJF, SRTF, and LJF increases by 4.6%, 3.6%, and 12.76%, respectively, after adding power system jobs. This percentage increase in queue time is directly proportional to the increase in number of preempted tasks of the data center.

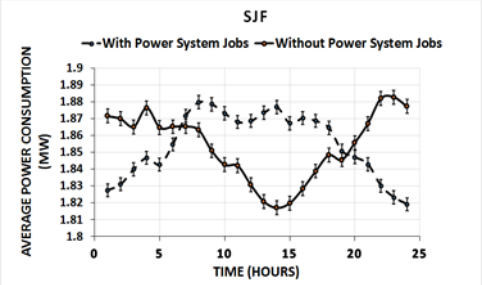

(a)

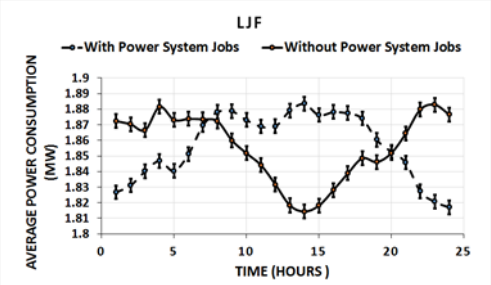

(b)

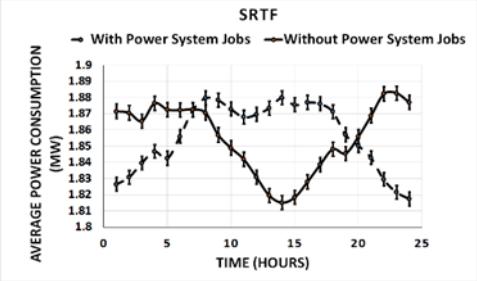

(c)

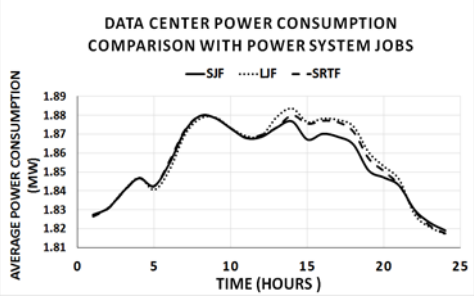

(d)

Figure 5.5. Power consumption comparison of data center under: (a) SJF, (b) LJF, and (c) SRTF job scheduling techniques. (d) Power consumption comparison of data center for all three job scheduling techniques when power system jobs are included

The workload makespan demonstrates the total running time of jobs on the data center. A job scheduling technique with a longer makespan results in increased power consumption. The maekespan of LJF for power system jobs is approximately 17.4 minutes longer than for SJF and 15.6 minutes longer than SRTF, as shown in Figure 5.13. As illustrated in Figure 5.14, a similar effect is observed for the overall data center makespan, which increases by 2.37%, 0.5%, and 0.53% using LJF, SJF, and SRTF respectively, after adding power system jobs. As shown in Figure 5.7 and Figure 5.11, SJF preempts fewer jobs and the percentage increase in average queue time for the jobs is smallest compared to the other two job scheduling techniques.

However, SRTF has minimum average queue time among all three job scheduling techniques. The power consumption of the data center is also affected by idle running resources. We observed the effect of resource utilization in the data center, as shown in Figure 5.15. The waste of idle running resources was reduced most by using SJF; however, SRTF results in the least number of idle CPUs. SRTF results in the least makespan and queue time, which allows jobs to complete earlier. Therefore, more resources will be available for execution of power system jobs within the allotted time. Given the current simulation parameters for data center workload and number of power system jobs. The best job scheduling technique among all three, when we consider number of power system job preemptions.

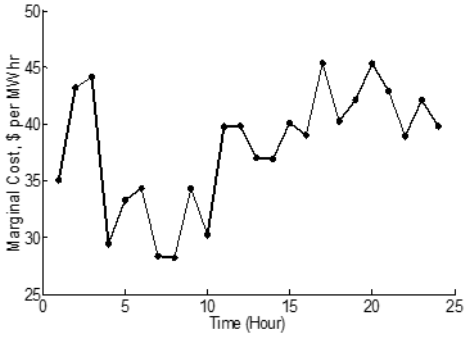

Figure 5.6. Real-time electricity unit pricing offered by the power system to the data center during a 24 hour period [5.17]

Therefore, using SJF and SRTF, the data center can safely agree on a SLA with the power system for computationally intensive ancillary services with minimum impact on the rest of the data center workload. We conclude that there is a trade-off between the two job scheduling techniques (SJF and SRTF). However, we have to compromise on average queue time and makespan of data center workload. In our ASM, the power system provides incentives to the data center to nullify the negative impact on data center revenue due to prioritizing power system jobs. These incentives include a lower electricity unit price during the execution period of power system jobs.

Moreover, as illustrated in Figure 5.9, SJF and SRTF preempted the fewest power system jobs during the entire month, which is the minimum job preemption possible for executing power system jobs. Therefore, we define this percentage as our threshold. If the data center preempts more jobs than this threshold, then the data center will sustain a penalty cost. For example residential load, commercial load, and industrial load. In the real-world, the background load varies depending on consumer requirements and the daily load curve. Therefore, inequality constraints are applied to the random background loads.

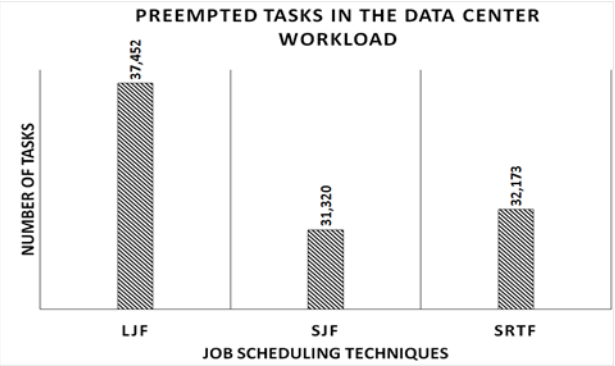

Figure 5.7. Task preemption comparison in data center workload in one month's time due to the inclusion of power system jobs

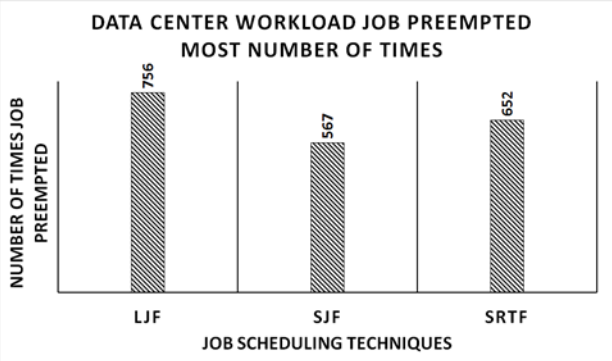

Figure 5.8. Comparison of data center workload job preempted the most times

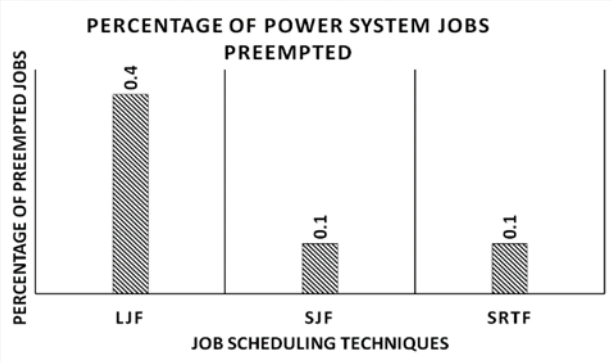

Figure 5.9. Comparison for preempted power system jobs

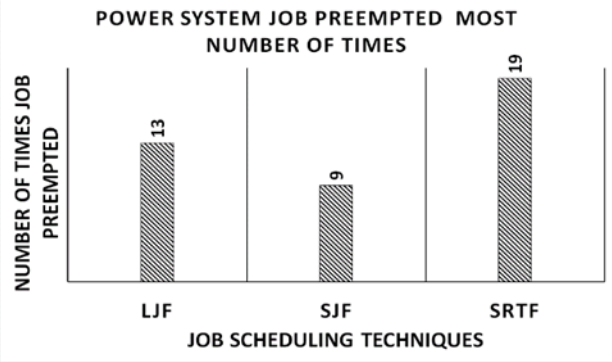

Figure 5.10. Comparison of longest running periodic power system job preempted the most number of times

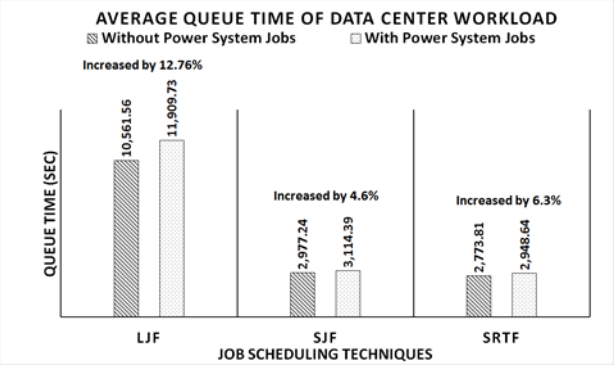

Figure 5.11. Comparison of data center workload average queue time

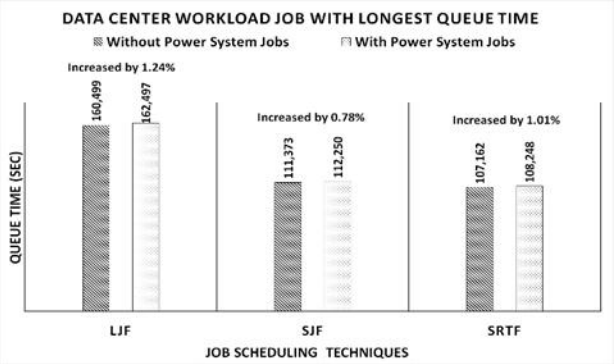

Figure 5.12. Comparison of data center workload job with longest queue time

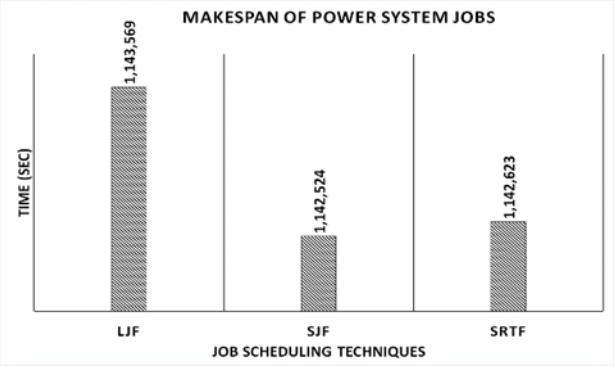

Figure 5.13. Comparison of total running time for power system jobs during a month's time

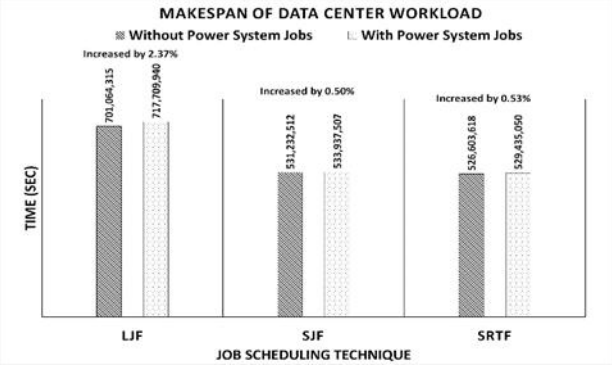

Figure 5.14. Comparison of total running time for data center's workload during a month's time

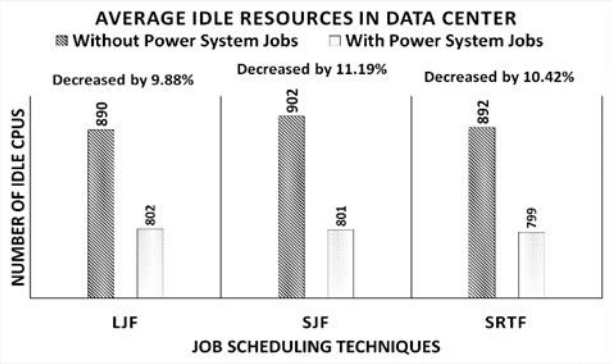

Figure 5.15. Comparison of data center idle CPUs

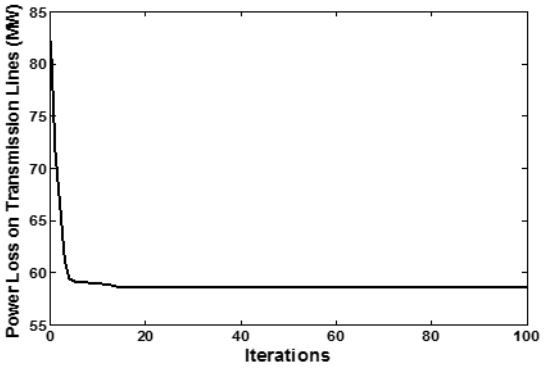

Figure 5.16. TLL convergence using the OPF algorithm for the IEEE 2383 bus system when 17 TLs are out

The stability and reliability of the power system depends on a balanced power flow solution. Once TL failures occur, the main requirement is to balance the generation and load. The bound on the inequality constraint is adjusted, such that the sum of the background load power

(active and reactive) does not exceed the total generation of the IEEE bus system minus the peak power consumption of the data center. Secondly, standard deviation of the background load on any given load bus is set at 10KW with mean value of the loads for all tested IEEE bus systems provided in Table 5.1.

The cost/objective function for the OPF solution is active power loss on all TLs. The power loss in the system is calculated with real power miss-match between the sending and receiving bus of each TL. TL outages are randomly generated. Whenever an outage occurs, the power system jobs become emergency jobs. Moreover, when there is a drastic change in load, the jobs generated are called reactive jobs. For normal steady-state operation, the power system requires periodic checks on load and generation. These jobs are called periodic jobs. The data center will calculate the OPF solution to balance the power system for all three cases. If the OPF fails to converge, then this situation is known as a blackout or system failure. Moreover, if the OPF converges but TLLs exceed 5% of the generated power, then the system is still considered to be in a failure state. Figure 5.16 illustrates the convergence iterations of the OPF algorithm for the IEEE 2383 bus system. The OPF converges in 17-23 iterations in most situations. The least TLLs achieved for the 17 TLs outage case is 58.594MW, which is less than 5% of the total generated power, making this an acceptable loss. During contingencies, the TL importance index is also calculated. For the clarity of the readers, the results for the IEEE 30 bus system are presented in Figure 5.17(a). The IEEE 30 bus system presents a more elaborative picture of TL outages. With increased power system network size, such as the IEEE 2383 bus system, the influence of TL outages on the system is not well visualized graphically.

Figure 5.17(a) shows that TL 10 and TL 20 are the most endangered TLs in the IEEE 30 bus system because the AC power flow ratio of these TLs are higher than the threshold. The

overall system has more chance of failure if an outage occurs on these TLs. Furthermore, Figure 5.17(b) shows the centrality based bus importance index. Buses with higher centralities are more prone to cause TL failures because these buses are associated with those TLs that have high AC power flow, and load power on these buses is more than for other buses. This concept is similar to the node centrality concept in networks [5.15]. In Figure 5.17(b), we observe that bus 1, bus 2, bus 3, bus 4, and bus 12 are the most critical buses in the IEEE 30 bus system. The data center provides an optimized OPF solution to reduce AC power flow on endangered TLs. The OPF solution also reduces overloading on these buses. Figure 5.18(a) shows the optimized AC power flow ratio of all TLs after running the OPF algorithm. The AC power flow on TL 10 and TL 20 has been reduced, such that the remaining TLs are no longer in danger. Figure 18(b) illustrates the reduction in the bus importance index compared to Figure 5.17(b). The decrease in centrality values of the endangered buses is observed. However, Figure 5.18(b) shows the increase in centrality values of bus 6 and bus 12. From Figure 5.3, we can observe from the one-line diagram of the IEEE 30 bus system that bus 6 is the most central and critical bus in the network.

Therefore, the centrality value of bus 6 will remain high. Moreover, bus 12 is directly connected to bus 13 that is directly linked with a 37MW generator. Bus 12 is the only connection between the 37MW generator and the entire network, such that when the transmission line between bus 12 and bus 13 is out, the network suddenly faces a power drop of 37MW. Therefore, bus 12 is the second most critical bus in the system; and after the OPF solution it still remains critical. The aforementioned analysis and discussion plays a pivotal role for maintaining stability, robustness, steady-state operation, and reliability of the power system. However, a problem arises when the data center is unable to complete ancillary services in time. Figure 5.19 depicts the data center revenue curve, as illustrated in Eqn. (5.11). In Figure 5.19, 100% revenue

means that the incentives, $\mathfrak{F}_i$, provided by the power system, all become the profit of the data center. Section 5.7 describes the results of the data center's revenue loss for providing ancillary services to the power system on a priority basis. In the ASM, the data center is compensated for this loss by the power system. Therefore, the data center will be motivated to prioritize execution of the power system's jobs. According to Eqn. (5.11), the power system will not only provide the cost, $\mathcal{L}_i$, for the ancillary services to the data center, but will also provide incentive, $\mathfrak{F}_i$, to maintain a minimum profit level for the data center.

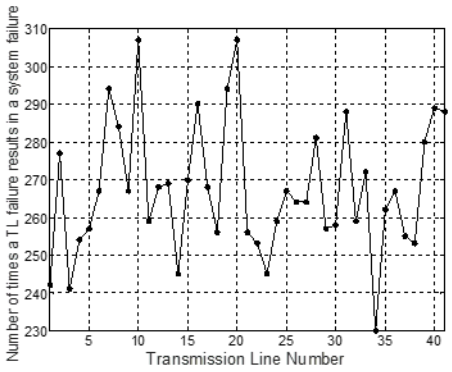

(a)

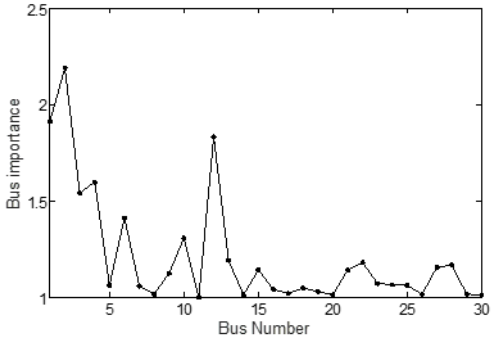

(b)

Figure 5.17. IEEE 30 bus system status during emergency, when an outage occurs on N-k transmission lines. (a) Transmission line importance index and (b) Bus importance index

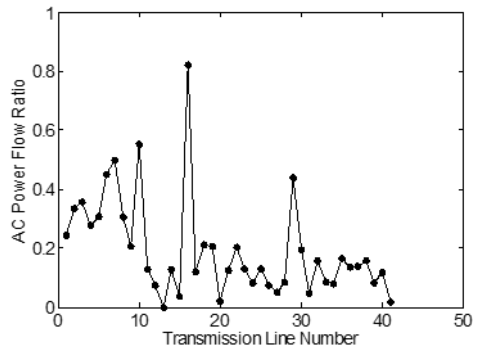

(a)

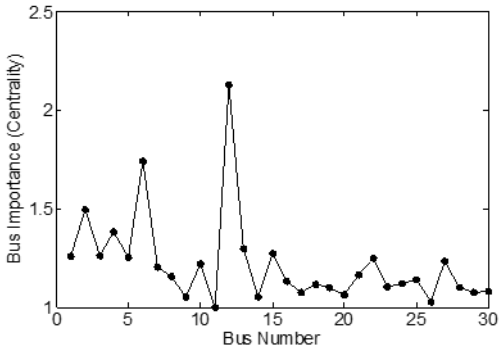

(b)

Figure 5.18. IEEE 30 bus system status after OPF solution provided by the data center. (a) AC power flow on Transmission lines and (b) Bus importance index

Furthermore, the graph below 0% depicts when the data center incurs a net loss in revenue by delaying cloud computing jobs to execute power system jobs. Figure 5.19 also illustrates the minimum failure rate (q_i = 0.48) for a power system job that is bearable for the data center. In Figure 5.9, the LJF preempts 0.4% of power system jobs during a month's time, which means approximately eleven power system jobs are preempted. However, SJF and SRTF only preempt two power system job per month. Therefore, if two or more power system jobs are delayed more than 48%, the data center will lose revenue.

5.8. ASM Convergence

To understand the concept of ASM convergence, a specific case of the IEEE 2383 bus system is considered. The parameters of the system have certain limitations, as listed in. Table 5.5. We arbitrarily selected 17 out of the 2896 TLs of the IEEE 2383 bus system to incur an outage for a period of ten minutes. The TLLs are increased to 62.216MW. The OPF algorithm reduces the power loss to 58.699MW and saves 3.517MW of power. In response, the incentives provided to the data center will be equivalent to the power saved by reducing TLLs.

Figure 5.20 shows a nonlinear curve between percentage increase in data center power consumption and corresponding percentage increase in data center cost, when power system jobs are executed on the data center. The intersection points C represents the percentage increase in data center cost when SJF and SRTF job scheduling techniques are used, while point D represents the percentage increase in data center cost when LJF is used. The horizontal solid-line defines the threshold amount that the power system will offer to the data center for providing OPF solution and reduction in power losses, as mentioned above. Therefore, Point B represents the maximum increase in power consumption (0.29%) of the data center that will be compensated by the power system. If the increase in power consumption is more than this threshold, data center will be in loss.

The aforementioned discussion is only for the specific case of 17 TLs out in the IEEE 2383 bus system. The threshold defined by horizontal solid-line is dependent on the power system network size and number of TLs out. In the IEEE 2383 bus system, if the number of TLs out is more than 17, then the OPF algorithm will not provide a converged solution. Therefore, we conclude that the region of convergence for data center revenue, for this case only, will have a threshold of approximately 0.29% increase in power consumption of the data center. The data

center's revenue will decrease whenever its power consumption exceeds this threshold, since the power system will not be able to provide enough compensation to the data center. Moreover, LJF is not be suitable for the execution of power system jobs. However, we can use either SJF or SRTF for scheduling power system jobs on data center.

The above discussion and analysis elaborates the integration model of data centers and power system. Through mutual ancillary services, data center will increase its revenue, while power system will increase the steady-state performance and reliability during emergencies.

Table 5.5. Input parameter constraints for model convergence at peak-load hour

System Model	Parameters Description	Convergence Constraints
Power System	Maximum number of TL outage that the power system can sustain	17
	Tolerance between power injection and power consumption	10^{-8}
	Limit on each Background Load	13.84MW±10kW
	Maximum Background Load (BL)	0<BL≤ 2458.4MW
	Maximum Power Loss (PL) savings resulting from the OPF data center calculation for the case of 17 TLs out	\$0 < PL ≤ \$3880
Data Center	Maximum Incentives given to the data center ($\mathcal{L} + \mathfrak{F}$)	$\mathcal{L} + \mathfrak{F} \leq$ PL

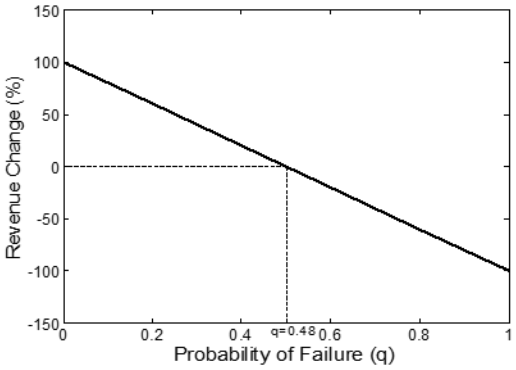

Figure 5.19. Data center revenue curve due to the implementation of the proposed service level agreement

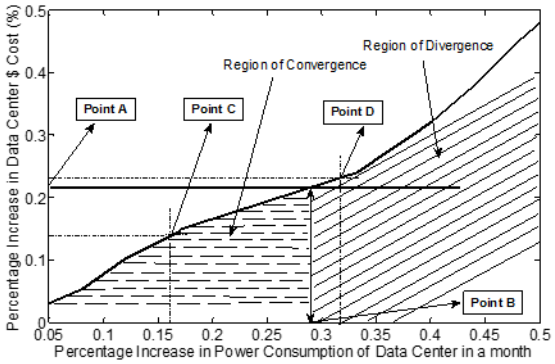

Figure 5.20. Revenue convergence region for the data center. Point A depicts the percentage cost saved by OPF to reduce TLLs for the case of 17 TLs out. Point B depicts the maximum increase in power consumption of the data center to not lose revenue. Point C depicts the increase in cost due to SJF and SRTF. Point D depicts the increase in cost due to LJF

5.9. References

[5.1] J. Shuja, K. Bilal, S.A. Madani, M. Othman, R. Ranjan, P. Balaji, and S.U. Khan, "Survey of techniques and architectures for designing energy-efficient data centers," *IEEE Systems Journal*. (DOI: 10.1109/JSYST.2014. 2315823.)

[5.2] J. Yao, X. Liu, W. He, and A. Rahman, "Dynamic control of electricity cost with power demand smoothing and peak shaving for distributed internet data centers," *Proc. IEEE 32nd Int. Conf. on Distributed Computing Systems* (ICDCS), pp. 416-424, June 2012.

[5.3] A. Rahman, X. Liu, and F. Kong, "A survey on geographic load Balancing based data center power management in the smart grid environment," *IEEE Communications Surveys & Tutorials*, vol. 16, no. 1, pp. 214-233, 2014.

[5.4] A. Singh, J. Bapat, and D. Das, "Distributed health monitoring system for control in smart grid network," *Proc. IEEE Innovative Smart Grid Technologies - Asia* (ISGT Asia), pp. 1-6, Nov. 2013.

[5.5] M. Mahmoudian and G.R. Yousefi, “ATC improvement and losses estimation considering dynamic transmission line ratings,” *Proc. 20th Iranian Conf. on Electrical Engineering* (ICEE), pp. 404-409, May 2012.

[5.6] A.A. Chandio, K. Bilal, N. Tziritas, Z. Yu, Q. Jiang, S.U. Khan, and C.Z. Xu, “A comparative study on resource allocation and energy efficient job scheduling strategies in large-scale parallel computing systems,” *Cluster Computing*, vol. 17, no. 4, pp. 1349-1367, 2014.

[5.7] G. Pannell, D. Atkinson, and B. Zahawi, “Minimum-Threshold Crowbar for a Fault-Ride-Through Grid-Code-Compliant DFIG Wind Turbine,” IEEE Trans. on Energy Conversion, vol. 25, no. 3, pp. 750-759, Sept. 2010.

[5.8] Z. Liu, M. Lin, A. Wierman, S.H. Low, and L.L.H. Andrew, “Greening geographical load balancing,” *IEEE/ACM Trans. on Networking*, pp. 233-244, no. 99, Mar. 2014.

[5.9] M.A. Adnan, R. Sugihara and R. Gupta, “Energy efficient geographical load balancing via dynamic deferral of workload,” *Proc. of IEEE CLOUD*, pp. 188-195, 2012.

[5.10] P. Wang, L. Rao, X. Liu and Y. Qi, “D-pro: dynamic data center operations with demand-responsive electricity prices in smart grid,” *IEEE Trans. on Smart Grid*, vol. 3, no. 4, pp. 1743-1754, 2012.

[5.11] Y. Yao, L. Huang, A.B. Sharma, L. Golubchik, and M.J. Neely, “Power cost reduction in distributed data centers: A two-time-scale approach for delay tolerant workloads,” *IEEE Trans. on Parallel and Distributed Systems*, vol. 25, no. 1, pp. 200-211, Jan. 2014.

[5.12] S.U. Khan and I. Ahmad, “A cooperative game theoretical technique for joint optimization of energy consumption and response time in computational grids,” *IEEE Trans. on Parallel and Distributed Systems*, vol. 20, no. 3, pp. 346-360, 2009.

[5.13] M. Manzano, K. Bilal, E. Calle, and S.U. Khan, "On the connectivity of data center networks," *IEEE Communications Letters*, vol. 17, no. 11, pp. 2172-2175, 2013.

[5.14] T. Zabaiou, L.A. Dessaint, and I. Kamwa, "Preventive control approach for voltage stability improvement using voltage stability constrained optimal power flow based on static line voltage stability indices," *IET Generation, Transmission & Distribution*, vol. 8, no. 5, pp. 924-934, May 2014.

[5.15] M. De and S.K. Goswami, "Optimal reactive power procurement with voltage stability consideration in deregulated power system," *IEEE Trans. on Power Systems*, vol. 29, no. 5, pp. 2078-2086, Sept. 2014.

6. CONCLUSION AND FUTURE WORK

This dissertation contributes to the development of a novel stability problem for power systems. We proposed an Exact Feedback Linearization (EFL) control for grid interfaced Permanent Magnet Synchronous Generators (PMSG) and a Hybrid Control Strategy for an effective Fault Ride Through (FRT) operation for Doubly Fed Induction Generator-Wind Turbines (DFIG-WT). Moreover, we also present a novel bi-directional ancillary services model for power system and data centers. Designing a stable control system is challenging because of the uncertainties during faults, and disturbances. By efficiently designing the control system, the proposed schemes achieved better performance in terms of robustness, performance, and steady-state performance during faults. The proposed research and simulation results are presented in separate chapters, and a brief summary of contributions is provided in the following subsection.

6.1. Summary of Contributions

In Chapter 3, we presented a detailed simulation and analysis of the PMSG models interfaced with the grid network. The stability and robustness against faults and disturbances plays a pivotal role in the efficiency of the grid-interfaced PMSG wind energy systems. We applied the EFL control scheme for the critical and comparative analysis of the PMSG Boost and PMSG Rectifier-Inverter. The spikes perturbations in the output DC link voltage response of the PMSG Boost were the main cause of instability in the designed system. The involvement of the trigonometric parameters in the control model of the PMSG Boost resulted in small spikes in the output DC link voltage. The EFL control law for the PMSG Boost was further linearized and simplified that resulted in the effective performance of the system in case of electrical grid faults. The stability of the PMSG Boost was limited, as the mechanical torque variations were only accepted up to 95% of the rated value.

The robustness of the PMSG Rectifier-Inverter was tested using different perturbations. The PMSG Rectifier-Inverter was proved to be more robust and efficient as compared to the PMSG Boost during the grid faults and varying mechanical perturbations for the wind energy applications. The EFL controller performance was compared with the conventional PI controller. In the PMSG Rectifier-Inverter, the EFL controller generated the fast response, quick settling time, and more robust performance as compared to the PI controller.

Chapter 4 discussed the FRT schemes employed for grid-interfaced DFIG-WTs. We evaluated the symmetrical and asymmetrical grid faults for the stability and steady-state performance of the DFIG-WT during FRT operation. Among all above mentioned strategies, Hybrid control strategy (Strategy-D) performs a robust and optimized performance with limited overloading of the power devices. Under symmetrical grid faults of 300ms, the proposed scheme was capable of power generation and absorbs excessive energy with slight increase in rotor speed at coupling point. Moreover, the fault switching transients and DC link voltage were suppressed effectively in rotor side converter and grid side converter. Furthermore, by implementing new control strategy, DFIG-WT provided voltage and reactive power support to the grid and effective "ride-through" during grid faults.

In case of asymmetrical grid faults, double-phase (2Φ) fault was most serious for DFIG-WT during FRT. The negative-sequence stator voltage induced very high EMF in rotor side converter than positive-sequence voltage. The positive-sequence power capability of WT was also limited for asymmetrical faults. For severe, grid faults, the fluctuations cannot be eliminated because of limited power rating capabilities of the electronic circuitry. There existed a trade-off between damping oscillations and power support of WT. Moreover, our proposed strategy strongly fulfilled stringent grid-code requirements for FRT. Furthermore, compared to classical

and advanced schemes, Hybrid Control Strategy provided the most robust control against various short-circuit faults.

In Chapter 5, we proposed an analytical model for a mutually beneficial relationship between a data center and its power system. The model ensures data center revenue maximization and power system stability and reliability enhancement. Our model includes several factors, such as Service Level Agreement (SLA), electricity price, data center revenue model, Optimal Power Flow (OPF) solution for the power system to reduce transmission line losses, and identification of endangered buses and transmission lines. The simulations using a real-world data center's workload and IEEE standard bus systems validate the performance of the Ancillary Services Model (ASM).

6.2. Future Work

In the near future, we will extend the robust affine PMSG grid-interfaced wind energy system to various MIMO-WECS using the EFL control scheme. We will further incorporate multi-RERs, multi-decentralized controls and power grid model together for the smart design of the MIMO-WECSs for the RE application in the smart grid environment. Our multi-decentralized control model of MIMO system will include excitation control, steam-valve control, and ripple free DC link voltage.

We will also extend our work of FRT operation of DFIG-WT further using PMSG-WT control during grid faults. The differential geometry and Lie-algebra based control, such as exact feedback linearization will be used for designing higher-order schemes for effective FRT operation for both DFIG and PMSG.

The proposed ASM will be further extended to multiple data centers attached to the power system. Various demand response pricing schemes, such as time-of-use pricing will be

incorporated to develop cost reduction models and power management algorithms for the data centers and power system. This work will be further extended by incorporating the geographical locations of the cloud data centers. We will consider electricity price differences and server loading conditions for jobs migration, execution, and re-directing. The service level agreement of clients and cloud data centers will also be incorporated for the design of more cost efficient fault tolerant system.